Precision Simulations for Future Colliders

Alan Price

A Thesis presented for the degree of
Doctor of Philosophy

Durham University

Institute for Particle Physics Phenomenology
Department of Physics
Durham University
United Kingdom

December 2020

Precision Simulations for Future Colliders

Alan Price

Submitted for the degree of Doctor of Philosophy

December 2020

Abstract: Future particle colliders will usher in a new era of precision physics. It will be crucial that the theory community can provide highly precise predictions for these experiments. In particular, for future e^+e^- colliders the theoretical calculations will need to improve by a factor 2-100, depending on the observable. In this thesis, we will present the theoretical improvements implemented in the SHERPA event generator for e^+e^- physics. We will concentrate on the treatment of QED radiation within the framework of Yennie, Frautschi and Suura resummation and discuss its impact on future colliders. In particular, we shall show how initial state radiation can be resummed in a process-independent manner to all orders in the QED coupling. We find that the resummation alone is not sufficient, and the inclusion of fixed-order corrections improves the perturbative description substantially. We will apply these corrections to the study of $e^+e^- \to f\bar{f}$, $e^+e^- \to W^+W^-$ and $e^+e^- \to ZH$ processes at a future lepton-lepton collider, and discuss the impact of the QED corrections.

In the second part of this thesis we will consider precision calculation of W/Z+jet at a future hadron-hadron colliders, namely the HE-LHC/FCC-hh. The theoretical modelling of these processes is crucial for controlling the background in many beyond the standard model searches. The processes are calculated up to next-to-next leading-order in the QCD coupling α_s. A detailed and robust study of the associated scale and shape uncertainties is presented.

Contents

List of Figures

List of Tables

Declaration

The work in this thesis is based on research carried out in the Department of Physics at Durham University. No part of this thesis has been submitted elsewhere for any degree or qualification.

Acknowledgements

Finally, my most heartfelt thanks have to go to my family. Mammy, Daddy, and Ava thank you for your continued support and encouragement, not only for the last three years, but throughout my life. This thesis is dedicated to you guys.

Between my finger and my thumb

the squat pen rests.

I'll dig with it.

— from *Digging* by Seamus Heaney

Chapter 1

Introduction

The validation of the Standard Model (SM) of particle physics is a triumph of modern physics. With an unprecedented amount of data gathered, the Large Hadron Collider (LHC) continues to provide a rich environment, that allows us to test our knowledge of fundamental particles and their interactions with matter. The crowning achievement of the LHC has been the discovery of a new scalar particle by the ATLAS [1] and CMS [2] collaborations, which to date has all the signatures of a Standard Model Higgs-Boson with a mass $m_H = 125.09 \pm 0.21(\text{stat.}) \pm 0.11(\text{syst.})$ GeV [3]. The coupling of the Higgs-Boson has been measured to vector bosons [4–8], to the top quark [9–12], the bottom quark [13, 14], the tau lepton [15, 16] and some first hints of its coupling to the muon [17, 18].

To date, there has not been any discovery of physics beyond the SM at the LHC, yet other experiments have made observations that are not explained within its framework, for example, the observation of non-zero neutrino masses, dark matter, and the anti-matter matter asymmetry. Developing more of an understanding of the origin and nature of the Higgs-Boson may answer some of these questions. While the LHC, and its hadronic successor, may yet provide a deeper understanding to the nature of the Higgs-Boson, there exists an alternative, and compatible [19], experimental avenue that the community can explore. A future lepton-lepton collider or "Higgs-Factory" could provide unprecedented measurements of the SM. Unlike a

hadronic machine, a lepton-lepton collider has a very clean initial state, due to the fact that leptons are point like particles. This allows for an experimental environment where measurements can be preformed with an unprecedented precision, which will allow for precise measurements of electroweak pseudo-observables (EWPO) [20]. Such a collider may be circular or linear and currently there are four proposals being considered.

The Future Circular Collider is a post-LHC particle accelerator, that initially would be e^+e^- collider (FCC-ee) [21, 22] and later, a high energy hadron-hadron collider (FCC-hh). For the leptonic stage there are four proposed energies at which the leptons will be collided. The first stage, which will last four years, will run at the Z-pole and is expected to collect 150 ab^{-1} of data, which corresponds to the production of around 10^{12} Z bosons [21]. Following this, there will be a two year run at the W^+W^- production threshold, $\sqrt{s} = 161$ GeV, with a projected integrated luminosity of 12 ab^{-1} or 10^8 W^+W^- pairs. After the W^+W^- run, there will be a three year run at $\sqrt{s} = 240$ GeV to produce the Higgsstrahlung process $e^+e^- \rightarrow ZH$. While this energy does not correspond to the maximum cross section for Higgsstrahlung, it does maximize the event per unit time due to the colliders luminosity profile. This run will produce 1 million ZH events with an integrated luminosity of 5 ab^{-1}. The last run will be at the $t\bar{t}$ threshold, which will done as a multipoint scan around the threshold range $\sqrt{s} = 345 - 365$ GeV. The integrated luminosity for this run is expected to be 1.5 ab^{-1} which will result in a 10^6 $t\bar{t}$ events.

The Circular Electron Positron Collider (CEPC) [23, 24], is a Higgs-factory that would based in China. With a circumference of 80 km, it is designed to operate at around 91.2 GeV as a Z-factory, at 160 GeV for of the W^+W^- production threshold, and at 240 GeV as a Higgs-factory. The CEPC will produce close to one trillion Z bosons, 100 million W bosons and over one million Higgs bosons during it operation. Like the FCC-ee, there is also the possibility for the CEPC to operate as hadron-hadron collider.

While circular colliders can reach large integrated luminosities, they are rather re-

stricted in their energy reach due to bremsstrahlung effects. The linear colliders on the other hand, do not suffer as much due to bremsstrahlung and can reach energies in the multi-TeV range. Though they can reach higher energies than a circular collider, they have reduced luminosities. The linear colliders will also be able use polarised beams to enhance their physics potential.

The Compact Linear Collider (CLIC) [25–27] is a multi-TeV linear e^+e^- machine, which is purposed to be built at CERN. It has three planned stage of operation, with centre of mass energies at, 380 GeV, 1.5 TeV, and 3 TeV. In the first stage, the Higgs boson will be measured through Higgsstrahlung and WW fusion and is expected to produce 160,000 Higgs bosons. Its energy range will then be extended into the TeV range, where it is expected to produce millions of Higgs-bosons.

The final e^+e^- collider being considered is the International Linear (ILC) [28–31] in Japan. The ILC is expected to run at multiple energies from the Z-pole up to 500 GeV, with a possible upgrade to 1 TeV. For $e^+e^- \rightarrow f\bar{f}$ and $e^+e^- \rightarrow W^+W^-$ there will be a dedicated run at 91 GeV and 160 GeV respectively. The next proposed run will be at 250 GeV where the ILC will study the Higgs-boson through $e^+e^- \rightarrow ZH$ with a projected integrated luminosity of 250 fb^{-1}. There will then be a run at the $t\bar{t}$ threshold followed by a run at 500 GeV. 500 GeV is currently the maximum planned centre of mass energy at the ILC but it is possible for the collider to be upgraded to 1 TeV which would allow it to probe rare Higgs couplings, such a the top and self couplings.

To take full advantage of these precision machines, the corresponding theory errors have to, at least, match the experimental uncertainties. There are two main types of theory uncertainties, parametric uncertainties, which are uncertainties on the SM input parameters, and the intrinsic error, which estimates the uncertainty due to missing higher-order terms. A large source of intrinsic uncertainty are the corrections due to QED radiation. A improvement factor of 2-100, depending on the observable, will have to be achieve to reduce the QED uncertainties to a level that is acceptable, as we see in Table 1.1. QED effects of the order 0.1% could be safely ignored

Observable	Where from	Current (LEP)	FCC (stat.)	FCC (syst.)	$\frac{\text{Now}}{\text{FCC}}$
M_Z [MeV]	Z linesh. [32]	$91187.5 \pm 2.1\{0.3\}$	0.005	0.1	3
Γ_Z [MeV]	Z linesh. [32]	$2495.2 \pm 2.1\{0.2\}$	0.008	0.1	2
$R_l^Z = \Gamma_h/\Gamma_l$	$\sigma(M_Z)$ [33]	$20.767 \pm 0.025\{0.012\}$	$6 \cdot 10^{-5}$	$1 \cdot 10^{-3}$	12
σ_{had}^0[nb]	σ_{had}^0 [32]	$41.541 \pm 0.037\{0.025\}$	$0.1 \cdot 10^{-3}$	$4 \cdot 10^{-3}$	6
N_ν	$\sigma(M_Z)$ [32]	$2.984 \pm 0.008\{0.006\}$	$5 \cdot 10^{-6}$	$1 \cdot 10^{-3}$	6
N_ν	$Z\gamma$ [34]	$2.69 \pm 0.15\{0.06\}$	$0.8 \cdot 10^{-3}$	$< 10^{-3}$	60
$\sin^2\theta_W^{eff} \times 10^5$	$A_{FB}^{lept.}$ [33]	$23099 \pm 53\{28\}$	0.3	0.5	55
$\sin^2\theta_W^{eff} \times 10^5$	$\langle\mathcal{P}_\tau\rangle, A_{\text{FB}}^{pol,\tau}$[32]	$23159 \pm 41\{12\}$	0.6	< 0.6	20
M_W [MeV]	ADLO [35]	$80376 \pm 33\{6\}$	0.5	0.3	12
$A_{FB,\mu}^{M_Z \pm 3.5\text{GeV}}$	$\frac{d\sigma}{d\cos\theta}$ [32]	$\pm 0.020\{0.001\}$	$1.0 \cdot 10^{-5}$	$0.3 \cdot 10^{-5}$	100

Table 1.1: The current systematic and statistical uncertainties on QED sensitive observables. The terms in {...} are the pure QED uncertainties. The FCC-ee error estimates have been taken from [36]. Reproduced from [37]

ignored at LEP, but cannot be ignored at future Higgs-Factories. For example, from a precise measurement of the total hadronic cross section of $e^+e^- \to f\bar{f}$ near the Z-pole, the mass and width of the Z boson can measured with an error of the order 0.1 MeV. The corresponding QED uncertainty will have to be reduced to $\delta_{QED} \leq 0.03\text{MeV}$ [38]. The inclusion of corrections up to $\mathcal{O}\left(\alpha^4 L^4\right)$, $L = \log\left(s/m_f^2\right)$, will become mandatory. In the first part of this thesis, we will explore how to model the emission of soft photons to all orders and how the logarithms associated with their emission are resummed using the Yennie-Frautschi-Suura [39] formulation. In the YFS approach, the photon emissions are treated in a fully differential form. The photons are explicitly created and the treatment of their phasespace is exact. An alternative inclusive approach to modelling the of soft collinear photons is the structure function approach [40] whereby, all of the logarithmic terms are collected in universal factors which are then resummed by the evolution of the DGLAP equations [41–44]. For a long time these structure functions have been known at leading-order accuracy [45–47] while in recent years these functions have been extended to next-to-leading logarithmic accuracy [48, 49].

We will present a process-independent algorithm for resumming initial state radiation (ISR) to all orders. A method for systematically including matrix element

corrections to the resummation will be introduced and we discuss the corrections to e^+e^- reactions. In the case of $e^+e^- \to f\bar{f}$ we will also discuss the resummation of final state radiation. A detailed comparison is performed against an existing implementation in the Monte Carlo event generator `KKMC` [50]. We then introduce a semi-analytical formulation of the ISR resummation. This approach was then implemented in a python program, the results from which were used to validate the full Monte Carlo calculation. We also consider the effect of ISR on import process for future lepton-lepton colliders such as, $e^+e^- \to ZH$, and $e^+e^- \to W^+W^-$.

In the second part of the thesis we shall present a study of $V+$jet production at the HL/HE-LHC. The accurate modelling of these process are essential for beyond the standard model (BSM) searches at future colliders. In Chapter 6 we discuss the importance of missing transverse energy (MET) in the search for BMS and how to control the relevant backgrounds, such as $Z(\nu\bar{\nu})+$jet, by means of precise calculations. The production of $W/Z+$jet will be calculated up NNLO in QCD and the theory uncertainties will be examined in depth.

Chapter 2

The SHERPA Framework

At particle colliders, like the LHC, collisions between incoming particles can lead
to a final state with hundreds of particles. Understanding these final states is an
extremely difficult theoretical challenge, with physical phenomena that range over
many orders of magnitude. At very high scales, perturbation theory can be used to
describe the interactions and production of particles, while at low scales the physics
is dominated by non-perturbative effects due to QCD confinement. This low scale
regime can only be described using phenomenological models, which are generally
tuned to data. These two scales are connected by an evolutionary process in which
partons at a high scale systematically emit QCD or QED radiation until they reach
a low scale cut-off. Each of these regimes are present at colliders and they need to be
modelled. This can be done in using separate Monte Carlo algorithms which can be
combined to simulate the full event. To achieve this difficult calculation has required
decades of work to develop the armoury of techniques used in simulating these events
accurately. Putting all of these together into one code will yield a general-purpose
event generator [51]. This thesis focuses on improving and utilising the physics of
one such generator, SHERPA. It is a member of the "big three", the others being
HERWIG [52,53] and PYTHIA [54,55], whose contributions to the experiments at the
LHC are invaluable. Nearly all analyses done at the ATLAS and CMS experiments
involve at least one of these codes. SHERPA has a highly modular framework, written

in C++, in which it provides the complete event generation from incoming beams to final state hadrons. In proceeding sections we introduce each module and give a short description of its physics content.

Hard-Scattering Matrix Element

The simulation of a scattering event begins with the calculation of the squared matrix element (ME). Once the hard-scattering configuration is known, the 4-momenta of the scattering particles can be sampled accordingly. This sampling allows one to determine the total production rate and differential distributions of the final-state objects to a given perturbative fixed-order accuracy, *e.g.* at tree-level or at next-to-leading order in the strong or electroweak coupling. As there are numerous processes of interest to users, both within the Standard Model and beyond, a high level of automation is not only highly desired but mandatory for the construction and evaluation of matrix elements.

SHERPA can calculate a wide variety of of MEs including, explicitly coded $2 \to 2$ squared amplitudes , tree level processes for large multiplicities, and can interface to external tools which can calculate MEs at the tree and one-loop level. There are two internal matrix-element generators (MEGs) within SHERPA, AMEGIC [56] and COMIX [57]. Both are fully automated and can generate full tree-level MEs for complicated final states. They both account for all correlations effects due to spin and color. Spin-0, spin-1/2 and spin-1 external particles can be handle by both and in addition, AMEGIC can also include spin-2 external particles. The MEGs allow for arbitrary couplings in both QCD and EW. This means that the user has the ability to calculate pure QCD or EW terms separately or to calculate specific interferences terms [58, 59].

In AMEGIC all tree-level Feynman diagrams are automatically generated. The diagrams are then transformed into helicity amplitudes, which for each set of external momenta are just complex numbers. In the construction of the diagrams, common

sub-diagrams are factored out and constructed only once thus dramatically reducing the computation time. The expressions for the amplitudes are written out as source code which is later automatically located and loaded.

COMIX calculates the tree-level matix-elements using the color-dressed Berends–Giele recursive relations [60,61], which is a tree-level version of the Dyson–Schwinger equations [62–64]. This algorithm has been show to be highly efficient for the calculation of processes with large multiplicities.

For BSM calculation SHERPA has an inbuilt interface to FEYNRULES [65,66]

Phase-Space Integration

The cross-section calculation requires the evaluation of multidimensional phasespace, typically that means an dimension of 3n-4 for an n-particle final state. In most cases the analytical solution is not known and we must turn to numerical methods. As the integrals of interest are, generally, high-dimensional integrals, Monte-Carlo integration is the obvious choice. This is due to the fact that in a Monte-Carlo method the uncertainty on the integrand scales like $\frac{1}{\sqrt{N}}$, for N sampled points, and its uncertainty is independent of the number of dimensions. SHERPA has a variety of methods which are used to evaluate integrals in high dimensional phasespace. These methods have been implemented in the *PHASIC* module. The overall objective of these methods is to perform a multichannel importance sampling, where the squared matrix element automatically provides the target distributions according to the propagators and vertices found in the Feynman diagram. The multi-channel integrator also provides an automatic optimisation for the individual channels as described in [67]. Typically AMEGIC will create one channel per Feynman diagram, whereas COMIX, due to its recursive nature, will reduce the growth of the integration channels to be exponential.

NLO **Matrix Elements**

For theoretical calculations in theLHC era, NLO calculations have become the industry standard. Due to the divergences in both virtual and real corrections, a cancellation scheme must be used to ensure a finite result. This has been implemented in SHERPA for NLO_{QCD} by automating the Catani-Seymour dipole subtraction formalism [68,69]. The renormalised virtual corrections are provided by external dedicated tools like BLACKHAT [70–72], GOSAM [73,74] MADGRAPH [75],OPENLOOPS [76] and RECOLA [77,78]. All of which can be used in SHERPA. As well as NLO_{QCD}, SHERPA can perform a subtraction for NLO_{EW} calculations [79] and NLO_{EW} virtuals can be provided by GOSAM, OPENLOOPS and RECOLA.

Parton Showers

In QCD, the evolution from the hard scale down to the hadronization scale is determined by parton-shower simulations. In these algorithms, the emission of QCD or QED particles off the initial and final state colored partons are iteratively produced from the hard process. This allows for the modelling of high-multiplicity final states consisting of partons at relatively low scale $Q_0 \approx 1$ GeV from a hard process at Q_{hard}. SHERPA has two parton showers implemented, CSSHOWER [80] and DIRE [81]. CSSHOWER is a shower based on the Catani-Seymour dipole factorisation, which was purposed in [82,83]. Each dipole contains a splitting parton and a colour-connected spectator parton. The shower evolves through sequential splittings of such dipoles. The dipole terms are calculated for initial-initial, initial-final and final-final emissions using unintegrated and spin-averaged operators which have be constructed in the large N_c limit.

DIRE [81] is the second parton shower implemented in SHERPA. Like CSSHOWER, DIRE is also based on the Catani-Seymour dipole subtraction. DIRE uses a symmetric ordering variable, based on the inverse soft Eikonal of the color dipole, which provides a closer resemblance to analytical resummation methods.

Matching and Merging

Another feature of SHERPA is the combination of the parton shower with the hard process. Matching [83,84] the parton shower to the hard process removes any double counting of NLO matrix element with the first emission of the parton shower. Sherpa employs the MC@NLO [85]. The multijet merging in SHERPA, first introduced in [86,87], has been a cornerstone since the creation of the generator. In-depth details of SHERPA's matching and merging are described in [88–91].

Hadronization

At low scales, final state hadrons are constructed by using SHERPA's hadronization models. The default hadronization in SHERPA is a variant of the cluster algorithm which has been implemented in AHADIC [92]. There is also an option to use the Lund string fragmentation model [93–95] These decays of these hadrons are implemented in the SHERPA module HADRONS which provides numerous matrix elements and form factors.

QED Corrections

SHERPA can provide QED corrections to hard or hadronic decays using an implementation of YFS resummation which has been implemented in the PHOTONS module [96]. These corrections can be applied to the leptonic decays electroweak bosons and to all hadronic decays. This resummation can also include higher order matrix elements to improve the accuracy of the calculation. The first part of this thesis will focus on extending the PHOTONS module to include corrections to e^+e^- processes. In particular, the implementation of the YFS resummation for ISR will be discussed in detail in Chapter 3.

Part I

Precision Simulations for Higgs Factories

Chapter 3

Yennie-Frautschi-Suura Resummation

3.1 Theory

The Yennie-Frautschi-Suura (YFS) formalism [39] provides a robust method for resumming the emission of real and virtual photons in the soft limit to all orders. The YFS resummation can be further improved by including exact fixed-order expression in a systematic way. In this chapter, we will first introduce the general YFS framework and then will concentrate on its applications to e^+e^- collisions.

By summing over all real and virtual photons, the total cross section is given by,

$$\sigma = \frac{1}{2s} \int \sum_{i=0}^{n_R} \frac{1}{n_R!} \, \mathrm{d}\Phi_q \, \mathrm{d}\Phi_{k_i} \, (2\pi)^4 \, \delta \left(P - \sum q_f - \sum k_i \right) \left| \sum_{n_V=0}^{\infty} \mathcal{M}_{n_R}^{n_V + \frac{1}{2} n_R} \right|^2. \quad (3.1.1)$$

In the matrix element notation that has been introduced here, the Born level contribution will be defined as $\mathcal{M}_0^0$, while the matrix element $\mathcal{M}_i^j$ will refer to the Born process plus i real photons evaluated at an overall coupling j in the electromagnetic coupling α. While this expression includes photon emissions to all orders it is an unrealistic ambition to be able to calculate all terms in Equation (3.1.1). In reality, we can only calculate the first few terms in the perturbative series.

Let us first consider the case of a single virtual photon. The factorised matrix element for this case can be written as

$$\mathcal{M}_0^1 = \alpha B \mathcal{M}_0^0 + M_0^1 , \qquad (3.1.2)$$

where M_0^1 is the infrared-subtracted matrix element including one virtual photon and it is finite as the photon momentum goes to zero. All soft divergences due to this virtual photon are contained in the universal factor B. YFS showed that the insertion of further virtual photons, in all possible ways, leads to

$$\mathcal{M}_0^0 = M_0^0,$$
$$\mathcal{M}_0^1 = \alpha B M_0^0 + M_0^1,$$
$$\mathcal{M}_0^2 = \frac{(\alpha B)^2}{2!} M_0^0 + \alpha B M_0^1 + M_0^2. \qquad (3.1.3)$$

For these we can see how the infrared subtracted matrix elements are constructed,

$$M_0^0 = \mathcal{M}_0^0,$$
$$M_0^1 = \mathcal{M}_0^2 - \alpha B M_0^0,$$
$$M_0^2 = \mathcal{M}_0^2 - \alpha B M_0^1 - \frac{(\alpha B)^2}{2!} M_0^0 \qquad (3.1.4)$$

And for a fixed order in α,

$$\mathcal{M}_0^{n_V} = \sum_{r=0}^{n_V} M_0^{n_V - r} \frac{(\alpha B)^r}{r!}. \qquad (3.1.5)$$

Summing the virtual photons to infinity,

$$\sum_{n_V=0}^{\infty} \mathcal{M}_0^{n_V} = \exp(\alpha B) \sum_{n_V=0}^{\infty} M_0^{n_V} . \qquad (3.1.6)$$

In QED this can be generalised to any number of real photons, such that

$$\left| \sum_{n_V=0}^{\infty} \mathcal{M}_{n_R}^{n_V + \frac{1}{2} n_R} \right|^2 = \exp(2\alpha B) \left| \sum_{n_V=0}^{\infty} M_{n_R}^{n_V + \frac{1}{2} n_R} \right|^2 . \qquad (3.1.7)$$

$M_{n_R}^{n_V + \frac{1}{2} n_R}$ is completely free of soft singularities due to virtual photons but it still may contain those due to real photons.

For a single real photon emission, the factorization occurs at the level of squared matrix elements and can be expressed as,

$$\frac{1}{2(2\pi)^3}\left|\sum_{n_V=0}^{\infty} M_1^{n_V+\frac{1}{2}}\right|^2 = \tilde{S}(k)\left|\sum_{n_V=0}^{\infty} M_0^{n_V}\right|^2 + \sum_{n_V=0}^{\infty} \tilde{\beta}_1^{n_V+1}(k)\,. \tag{3.1.8}$$

In this expression, all the singularities are contained within the eikonal, $\tilde{S}(k)$, and the $\tilde{\beta}_{n_R}^{n_V+n_R}$ are the infrared-finite squared matrix elements. They correspond to the Born level process plus emissions of n_R real and n_V virtual photons. For convenience we introduce the following notation,

$$\tilde{\beta}_{n_R} = \sum_{n_V=0}^{\infty} \tilde{\beta}_{n_R}^{n_V+n_R}\,. \tag{3.1.9}$$

The squared matrix element for n_R real emissions, summed over all possible virtual photon corrections, can be written as

$$\left(\frac{1}{2(2\pi)^3}\right)^{n_R}\left|\sum_{n_V=0}^{\infty} M_{n_R}^{n_V+\frac{1}{2}n_R}\right|^2 =$$

$$\tilde{\beta}_0 \prod_{i=1}^{n_R}\left[\tilde{S}(k_i)\right] + \sum_{i=1}^{n_R}\left[\frac{\tilde{\beta}_1(k_i)}{\tilde{S}(k_i)}\right]\prod_{j=1}^{n_R}\left[\tilde{S}(k_j)\right]$$

$$+ \sum_{\substack{i,j=1\\i\neq j}}^{n_R}\left[\frac{\tilde{\beta}_2(k_i,k_j)}{\tilde{S}(k_i)\tilde{S}(k_j)}\right]\prod_{l=1}^{n_R}\left[\tilde{S}(k_l)\right] + \ldots + \tilde{\beta}_{n_R}(k_1,\ldots,k_{n_R})\,. \tag{3.1.10}$$

Within this expression, all possible divergences due to the emission of soft photons are contained within the eikonals. There is no collinear divergence present, as the fermion mass prevents the photons from becoming fully collinear. It is therefore crucial that all fermion masses are included in any YFS calculation. The first term $\tilde{\beta}_0$ contains all virtual photon corrections to the Born matrix element. The second term in the expression corrects the approximation of $\tilde{S}(k_k)$ for the real emission of one additional photon. Similarly, the next term corrects for two real photons, and so on. If we demand that the expression agrees with the exact result up to $\mathcal{O}(\alpha^2)$ we have,

$$\left(\frac{1}{2(2\pi)^3}\right)^{n_R}\left|\sum_{n_V=0}^{\infty} M_{n_R}^{n_V+\frac{1}{2}n_R}\right|^2 =$$

$$\left(\tilde{\beta}_0^0 + \tilde{\beta}_0^1 + \tilde{\beta}_0^2\right) \prod_{i=1}^{n_R} \left[\tilde{S}\left(k_i\right)\right] + \sum_{i=1}^{n_R} \left[\frac{\tilde{\beta}_1^1\left(k_i\right) + \tilde{\beta}_1^2\left(k_i\right)}{\tilde{S}\left(k_i\right)}\right] \prod_{j=1}^{n_R} \left[\tilde{S}\left(k_j\right)\right]$$

$$+ \sum_{\substack{i,j=1 \\ i \neq j}}^{n_R} \left[\frac{\tilde{\beta}_2^2\left(k_i, k_j\right)}{\tilde{S}\left(k_j\right)\tilde{S}\left(k_j\right)}\right] \prod_{l=1}^{n_R} \left[\tilde{S}\left(k_l\right)\right] + \dots \tag{3.1.11}$$

Up to now we have been treating both initial and final state photons equally by including them in $n_R = n_I + n_F$. At this point it is useful to separate them, as later they will be treated differently in the MC algorithm. The approach we have chosen for our YFS resummation is known as exclusive exponentiation (EEX). This is a generalisation of YFS exponentiation, in which the soft photons are included independently for the initial and final states at the squared amplitude level. Any interference effects between the initial and final states are ignored for both the soft photon resummation and the $\tilde{\beta}$ terms.

To include initial-final interference (IFI) the YFS exponentiation has to be reformulated at the amplitude level. In [97] Jadach et al developed a method, which they called coherent exclusive exponentiation (CEEX), where the infrared divergences are summed to infinite-order at the amplitude level for both real and virtual photons. This allows for a correct treatment of IFI which is neglected in the EEX approach.

The EEX master formula is given by,

$$\left(\frac{1}{2(2\pi)^3}\right)^{n_I+n_F} \left|\sum_{n_V=0}^{\infty} M_{n_I+n_F}^{n_V+\frac{1}{2}(n_I+n_F)}\right|^2 =$$

$$\prod_{i=1}^{n_I} \left[\tilde{S}\left(k_i\right)\right] \prod_{j=1}^{n_R} \left[\tilde{S}\left(k_j\right)\right] \left(\tilde{\beta}_0 \right.$$

$$+ \sum_{j=1}^{n_I} \frac{\tilde{\beta}_{1I}(k_j)}{\tilde{S}\left(k_j\right)} + \sum_{l=1}^{n_F} \frac{\tilde{\beta}_{1F}(k_l)}{\tilde{S}\left(k_l\right)} + \sum_{n_I \geq j \geq k \geq 1} \frac{\tilde{\beta}_{2I}(k_j, k_k)}{\tilde{S}\left(k_j\right)\tilde{S}\left(k_k\right)}$$

$$\left. + \sum_{n_F \geq j' \geq k' \geq 1} \frac{\tilde{\beta}_{2F}(k_{j'}, k_{k'})}{\tilde{S}_F(k_{j'})\tilde{S}_F(k_{k'})} + \sum_{j=1}^{n_I}\sum_{k=1}^{n_F} \frac{\tilde{\beta}_{2IF}(k_j, k_k)}{\tilde{S}\left(k_j\right)\tilde{S}\left(k_k\right)} + \cdots\right). \tag{3.1.12}$$

Inserting this into our cross section formula Equation (3.1.1)

$$\sigma = \sum_{n_I=0}^{\infty}\sum_{n_F=0}^{\infty} \frac{1}{(n_I+n_F)!} \int d\Phi_f\, d\Phi_k\, (2\pi)^4\, \delta\left(P - \sum q_f - \sum k_i\right) e^{Y_f(\Omega)}$$

$$\prod_{i=1}^{n_I} \left[\tilde{S}\left(k_i\right)\right] \prod_{j=1}^{n_R} \left[\tilde{S}\left(k_j\right)\right] \left(\tilde{\beta}_0 + \sum_{j=1}^{n_I} \frac{\tilde{\beta}_{1I}(k_j)}{\tilde{S}\left(k_j\right)} + \sum_{l=1}^{n_F} \frac{\tilde{\beta}_{1F}(k_l)}{\tilde{S}\left(k_l\right)}\right.$$

$$+ \sum_{n_I \geq j \geq k \geq 1} \frac{\tilde{\beta}_{2I}(k_j, k_k)}{\tilde{S}(k_j)\,\tilde{S}(k_k)} + \sum_{n_F \geq j' \geq k' \geq 1} \frac{\tilde{\beta}_{2F}(k_{j'}, k_{k'})}{\tilde{S}_F(k_{j'})\tilde{S}_F(k_{k'})}$$

$$+ \sum_{j=1}^{n_I} \sum_{k=1}^{n_F} \frac{\tilde{\beta}_{2IF}(k_j, k_k)}{\tilde{S}(k_j)\,\tilde{S}(k_k)} + \cdots \Bigg). \tag{3.1.13}$$

In Equation (3.1.13) we have introduce the YFS form-factor which is defined as,

$$Y_f(\Omega) = 2\alpha \left[B + \tilde{B}(\Omega) \right]. \tag{3.1.14}$$

B has already been introduced in the case of virtual emissions but $\tilde{B}$ is new addition. It results from the fact that at each order in Equation (3.1.13) we have an integral of the form,

$$\sum_{n_R=0}^{\infty} \frac{1}{(n_R)!} \left(\int \frac{\mathrm{d}^3 k}{k^0} \tilde{S}(k)\, e^{-iyk} \right)^{n_R}. \tag{3.1.15}$$

where e^{-iyk} is extracted from the momentum conserving Dirac-delta. The divergences in this integral can be subtracted by introducing a soft region Ω,

$$\int \frac{\mathrm{d}^3 k}{k^0} \tilde{S}(k)\, e^{-iyk} = 2\alpha \tilde{B}(\Omega) + D(\Omega), \tag{3.1.16}$$

where,

$$2\alpha \tilde{B}(\Omega) = \int \frac{\mathrm{d}^3 k}{k^0} \tilde{S}(k) \left(1 - \Theta(k, \Omega) \right)$$

$$D(\Omega) = \int \frac{\mathrm{d}^3 k}{k^0} \tilde{S}(k) \left[\left(e^{-iyk} - 1 \right) \left(1 - \Theta(k, \Omega) \right) + e^{-iyk}\Theta(k, \Omega) \right]. \tag{3.1.17}$$

The Step function $\Theta(k, \Omega)$ has divided the phasespace into two regions. Ω contains the singular region with the infrared divergence, while $1-\Omega$ represents the remaining, infrared safe, phasespace. We define $\Theta(k, \Omega) = 1$ if the photon k does not reside in Ω and zero otherwise. Below we detail the individual terms in Equation (3.1.13).

- The eikonals are defined by

$$\tilde{S}(k) = \sum_{i<j} \tilde{S}_{ij}(k) = \frac{\alpha}{4\pi^2} Z_i Z_j \theta_i \theta_j \left(\frac{p_i}{p_i \cdot k} - \frac{p_j}{p_j \cdot k} \right)^2, \tag{3.1.18}$$

where the sum runs over all charged particle pairs and Z_i and Z_j are the charge of the particles and $\theta = \pm 1$ if the particle is incoming/outgoing. $p_{1,2}$ are the beam momenta oriented such that $p_{1,2} = \left(\frac{\sqrt{s}}{2}, 0, 0, \pm p_z \right)$

- Y_f is the YFS form factor,

$$Y_f(\Omega) = \sum_{i<j} Y_{ij}(\Omega) = 2\alpha \left[B_{ij} + \tilde{B}_{ij}(\Omega) \right], \qquad (3.1.19)$$

where the soft factors are defined as,

$$B_{ij} = -\frac{i}{8\pi^3} Z_i Z_j \theta_i \theta_j \int d^4 k \frac{1}{k^2} \left(\frac{2q_i\theta_i - k}{k^2 - 2(k \cdot q_i)\theta_i} - \frac{2q_j\theta_j + k}{k^2 + 2(k \cdot q_j)\theta_j} \right), \quad (3.1.20)$$

$$\tilde{B}_{ij}(\Omega) = \frac{1}{4\pi^2} Z_i Z_j \theta_i \theta_j \int d^4 k \delta(k^2) \left[1 - \Theta(k, \Omega) \right] \left(\frac{q_i}{qi \cdot k} + \frac{q_j}{qj \cdot k} \right)^2. \quad (3.1.21)$$

3.2 Algorithm

In this section we will introduce a process-independent algorithm for the generation of multiple soft photons across the entire phasespace, which only depends on the charged momenta of the Born process. For the phasespace generation we shall ignore higher-order corrections and reintroduce them later through a correction weight. We will begin with a discussion on how the initial state radiation is generated for arbitrary e^+e^- collisions, followed by a discussion on the final state radiation for $e^+e^- \to f\bar{f}$.

3.2.1 Initial State Radiation

This algorithm was first presented in [98] and we have recapitulated it here for completeness. While we concentrate on e^+e^- initial states, this method can be generalized to other massive charged particles. We will first simplify the distribution by neglecting higher-order β's in Equation (3.1.13) and later introduce a corrective weight to account for this simplification. By identifying $\beta_0 = d\sigma_{\text{Born}}(\hat{s})$, where $\sqrt{\hat{s}}$ is the reduced centre of mass energy, the total cross section, with respect to the Born phasespace, can be expressed as,

$$\sigma^{\text{ISR}} = e^{Y(\Omega(\epsilon))} \sum_{n=0}^{\infty} \frac{1}{n!} \int \prod_{i=1}^{n} \left[\frac{d^3 k_i}{k_i^0} \tilde{S}(p_1, p_2, k_i) \right] d\sigma_{\text{Born}}(\hat{s}) \qquad (3.2.1)$$

It also includes the integration over the Born phasespace, which we do not make explicit here as it is treated separately within the MC. To evaluate this integral we need to rewrite the multiphoton phasespace so that it is more suitable for Monte Carlo integration. Following the procedure detailed in Appendix A.2, the simplified cross-section can be written as two integrals, one when there are zero photon emissions and another for when soft photons have been emitted.

$$
\sigma_{\text{simple}}^{\text{ISR}} = e^{\frac{\gamma}{4} + Z_i Z_j \frac{\alpha}{\pi} \left(\frac{\pi^2}{3} - \frac{1}{2} \right)} \left[\int_0^\epsilon dv \, \gamma v^{\gamma - 1} \, d\sigma_{\text{Born}}(s) \right.
$$
$$
\left. + \int_\epsilon^{v_{\max}} dv \, d\sigma_{\text{Born}}(s(1-v)) \mathcal{J}_0(v) \bar{\gamma} v^{\bar{\gamma} - 1} \epsilon^{\gamma - \bar{\gamma}} \right]. \tag{3.2.2}
$$

As detailed in Appendix A.2 a change of variable $v = 1 - \frac{\hat{s}}{s}$ has been introduced. The lower integration limit ϵ correspond to the infrared cut-off on photon energy, $K_{\min} = \epsilon \frac{\sqrt{s}}{2}$. For the soft limit to hold we require $\epsilon \ll 1$. The new terms introduced in Equation (3.2.2) are defined as,

$$
\mathcal{J}_0(v) = \frac{1}{2} \left(1 + \frac{1}{\sqrt{1-v}} \right) \tag{3.2.3}
$$
$$
\gamma = \frac{2\alpha}{\pi} \left[\frac{1 + \beta_1 \beta_2}{\beta_1 + \beta_2} \ln \frac{(1 + \beta_1)(1 + \beta_2)}{(1 - \beta_1)(1 - \beta_2)} - 2 \right], \tag{3.2.4}
$$
$$
\bar{\gamma} = \frac{2\alpha}{\pi} \frac{1 + \beta_1 \beta_2}{\beta_1 + \beta_2} \ln \frac{(1 + \beta_1)(1 + \beta_2)}{(1 - \beta_1)(1 - \beta_2)}, \tag{3.2.5}
$$

where $A \leq 1$ and $\beta_i = \frac{|\vec{p_i}|}{p_i^0}$. The full cross-section needed to be simplified to remove any dependence on the total photon momentum. As we explained in Appendix A.2, this dependence will cause problems in the Monte Carlo as we only know $\tilde{K} = \sum_i k_i$ after we have generated all the momenta. Now that we have a simplified cross section, that is suitable for Monte Carlo integration, we need to correct for the simplifications we introduced.

- The first corrective weight is associated with dropping the mass term in the photon angular distribution in Equation (A.2.14). The weight is simply $w_1 = \prod_{i=1}^n \frac{g(\theta_i)}{\tilde{g}(\theta_i)}$, where $g(\theta)$ and $\tilde{g}(\theta)$ are defined in Equation (3.2.6). Respectively these result from the integration of the full eikonal and the reduced eikonal, in which terms $\mathcal{O}\left(\frac{m^2}{s}\right)$ are neglected.

- Setting $A = 1$ in Jacobian, $\mathcal{J}(\bar{K}, v) = \frac{1}{2}\left(1 + \frac{1}{\sqrt{1-Av}}\right)$, reduces the Jacobian to $\mathcal{J}_0$ and this simplification is corrected by $w_2 = \frac{\mathcal{J}}{\mathcal{J}_0}$.

- The third corrective weight is a veto on the individual photon energies and is defined as $w_3 = \prod_{i=1}^{n_R} \theta(k_i^0 - K_{\min})$.

- The fourth weight which is due to neglecting the higher order corrections and will be discussed in Section 3.3.

$$
\begin{aligned}
g(\theta) &= \frac{\alpha}{\pi^2}\left(\frac{2(1+\beta_1\beta_2)}{(1-\beta_1\cos\theta)(1+\beta_2\cos\theta)} - \frac{1-\beta_1^2}{(1-\beta_1\cos\theta)^2} - \frac{1-\beta_2^2}{(1+\beta_2\cos\theta)^2}\right), \\
\tilde{g}(\theta) &= \frac{\alpha}{\pi^2}\left(\frac{2(1+\beta_1\beta_2)}{(1-\beta_1\cos\theta)(1+\beta_2\cos\theta)}\right).
\end{aligned}
\tag{3.2.6}
$$

To obtain the total cross section from our simplified version we just multiply our simple distribution by the product of our corrective weights during the Monte Carlo integration. The corrected cross section is therefore defined as,

$$
\begin{aligned}
\mathrm{d}\sigma^{ISR} &= \prod_{i=1}^{2} w_i \, \mathrm{d}\sigma^{ISR}_{\text{simple}} \\
&= \prod_{i=1}^{n_R}\left[\theta(k_i^0 - K_{\min})\frac{g(\theta_i)}{\tilde{g}(\theta_i)}\right]\frac{\mathcal{J}(\bar{K}, v)}{\mathcal{J}_0(v)}\, \mathrm{d}\sigma^{ISR}_{\text{simple}}
\end{aligned}
\tag{3.2.7}
$$

Now all that remains to complete our calculation is to integrate Equation (3.2.7) over v, which can be preformed by standard MC methods. Once the main integration variable, v, is known the photons can be explicitly constructed. The number of photons is given by a Poissonian distribution with an average,

$$
\begin{aligned}
\bar{n} &= \int_{E_{min}}^{E_{max}} \frac{d^3k}{k^0}\tilde{S}(k) \\
&= -\frac{\alpha}{\pi}Z_1 Z_2 \theta_1 \theta_2 \ln\left(\frac{E_{max}}{E_{min}}\right)\left(\frac{1+\beta_1\beta_2}{\beta_1+\beta_2}\ln\frac{(1+\beta_1)(1+\beta_2)}{(1-\beta_1)(1-\beta_2)} - 2\right).
\end{aligned}
\tag{3.2.8}
$$

Then the n_R photon momenta are distributed as and rescaled as described in Appendix A.2. A reference frame is defined as $P = p_1 + p_2 - \sum_i k_i$ and the incoming momenta are then expressed as $\hat{p}_{1/2} = \left(\frac{\sqrt{\hat{s}}}{2}, 0, 0, \pm\hat{p}_z\right)$, where,

$$
\hat{p}_z = \frac{1}{2\sqrt{\hat{s}}}\left[(\hat{s} - (m_1 - m_2)^2)(\hat{s} - (m_1 + m_2)^2)\right]^{\frac{1}{2}}
\tag{3.2.9}
$$

which are rotated in the z-direction and then boosted in P. The new momenta are passed to SHERPA's phasespace module PHASIC, which constructs the final states from the reduced initial states according to the structure of the Feynman diagrams.

Phasespace Integration

At this point it is worth addressing how Equation (3.2.2) is generated in SHERPA. Usually, SHERPA calculates cross sections of the form,

$$\sigma_X = \sum_{ij} \int dx_1 dx_2 \, f_i(x_1, \mu_f) f_j(x_2, \mu_f) \hat{\sigma}_{ij \to X}(x_1, x_2; \mu_f, \mu_R) \tag{3.2.10}$$

where f_i are, depending on the initial state, either parton distribution or an electron structure function, and $\hat{\sigma}$ is the partonic cross section which includes the final state phasespace. This convolution is evaluated by using a change of variable $x_{1,2} \to \frac{M}{\sqrt{s}} e^{\pm Y}$ where $M^2 = \hat{s} = x_1 x_2 s$ and $Y = \frac{1}{2} \ln \left(\frac{x_1}{x_2} \right)$ is the rapidity. The integral is now preformed over $\hat{s}$ and Y instead of $x_{1/2}$, which is a standard transformation that converts Equation (3.2.10) to a more Monte Carlo friendly form. However, as the YFS approach to ISR does not factorize the emission based on incoming particles, but treats them together, there is no rapidity integral and only an integration over $\hat{s}$ is needed. This is quite obvious when inspecting Equation (3.2.2), that the only integration needed is over $v = 1 - \frac{\hat{s}}{s}$. To accommodate this, a new YFS specific integrator was implemented in the SHERPA framework using multi-channel importance sampling [67].

3.2.2   Final State Radiation

In this section, we present an algorithm for generating final state QED radiation. The algorithm was developed by Jadach et al in [50]. The algorithm focuses on the emission of final state soft photons in $e^+ e^- \to f \bar{f}$, $f \neq e$. The algorithm will be presented in a reference frame X, defined by $X = (\sqrt{s_x}, 0, 0, 0)$, where $s_x = (p_1 + p_2 - \sum_i k_i)$, $p_{1,2}$ are the initial state four-momentum, and k_i are the soft photons

emitted from the initial state. Let us consider the FSR part of Equation (3.1.13)

$$\mathcal{F}_{\bar{n}} = \frac{1}{\bar{n}!} \int_{4m_f^2}^{s_x} ds_Q \prod_{i=1}^{\bar{n}} \int \frac{d^3\bar{k}_i}{\bar{k}_i^0} \tilde{S}_f(\bar{k}_i) \Theta(\bar{k}_i - E_{\min}) \delta\left(s_X - \left(Q + \sum_{j=0}^{\bar{n}} \bar{k}_j \right)^2 \right) e^{Y(q_1, q_2)}$$
(3.2.11)

where $\bar{k}_i$ are the final state soft photons which are defined in the rest frame of the outgoing momentum $Q = q_1 + q_2$. $E_{\min}$ is the energy cut off for the photons. Again, we use an explicit polar parametrization for the photon momentum and with this we can eliminate the Dirac delta function.

$$\int_{4m_f^2}^{s_x} ds_Q \, \delta\left(s_X - \left(Q + \sum_{j=0}^{\bar{n}} \bar{k}_j \right)^2 \right) = \int_{4m_f^2}^{s_x} ds_Q \, \delta\left(s_X - s_Q \left(1 + \tilde{K}^0 + \frac{1}{4}\tilde{K}^2 \right) \right)$$

$$= \frac{\Theta(s_Q - 4m_f^2)}{1 + \tilde{K}^0 + \frac{1}{4}\tilde{K}^2},$$
(3.2.12)

where,

$$\tilde{K} = \sum_{i=0}^{\bar{n}} \tilde{k}_i,$$

$$\tilde{k}_i = x_i(1, \sin\theta_i \cos\phi_i, \sin\theta_i \sin\phi_i, \cos\theta_i).$$
(3.2.13)

This means that s_Q now depends on the photon momentum,

$$s_Q = \frac{s_X}{1 + \tilde{K}^0 + \frac{1}{4}\tilde{K}^2}.$$
(3.2.14)

The eikonal term can be treated the same as in the ISR case with the substitution $m_e \to m_f$, $s \to s_Q$.

$$\int \frac{d^3\bar{k}_i}{\bar{k}_i^0} \tilde{S}_f(\bar{k}_i) = \int \frac{dx_i}{x_i} \int \frac{d\phi_i}{2\pi} \int d(\cos\theta_i) \, g(\theta_i),$$
(3.2.15)

$$g(\theta) = Z_i Z_j \frac{2\alpha}{\pi} \left(\frac{2(1 + \beta_i\beta_j)}{(1 - \beta_i\cos\theta)(1 + \beta_j\cos\theta)} - \frac{1 - \beta_i^2}{(1 - \beta_i\cos\theta)^2} - \frac{1 - \beta_j^2}{(1 + \beta_j\cos\theta)^2} \right).$$
(3.2.16)

where $\beta_i = \frac{|\vec{p}_i|}{p_i^0}$. This leads to a partially factorized form of Equation (3.2.11).

$$\mathcal{F}_n = \frac{1}{\bar{n}!} \prod_{i=1}^{\bar{n}} \int_{\epsilon_f}^{\infty} \frac{dx_i}{x_i} \int_0^{2\pi} \frac{d\phi_i}{2\pi} \int_{-1}^{1} d\cos\theta_i \frac{\alpha}{\pi} g(\theta_i) \frac{\Theta\left(s_Q - 4m_f^2 \right)}{1 + \tilde{K}^0 + \frac{1}{4}\tilde{K}^2} e^{Y_F(q_1, q_2)}.$$
(3.2.17)

Equation (3.2.17) is not yet in a fully factorised form desirable for a Monte Carlo simulation. Ideally, we would want Equation (3.2.11) expressed as a product of $\bar{n}$ independent integrals for each photon. This is not yet the case for Equation (3.2.17), as there is an explicit dependence on the sum of the photon momenta in s_Q. Another issue that complicates matters is the fact that the upper limit can be quite large, for example in the case of a hard FSR photon, which can be inefficient for MC integration. A solution can be found by introducing a change of variables,

$$y_i = \frac{x_i}{1 + \sum_j x_j} = \frac{x_i}{1 + \tilde{K}^0}, \qquad (3.2.18)$$

where $K = \frac{\sqrt{s_Q}}{2}\tilde{K}$. This transforms Equation (3.2.17) to our primary distribution,

$$\mathcal{F}_n = \frac{1}{\bar{n}!}\prod_{i=1}^{\bar{n}} \int_{\frac{\epsilon_f}{1+\tilde{K}^0}}^1 \frac{dy_i}{y_i} \int_0^{2\pi} \frac{d\phi_j}{2\pi} \int_{-1}^1 d\cos\theta_i \frac{\alpha}{\pi} g\left(\theta_i\right),$$
$$\times \frac{1 + \tilde{K}^0}{1 + \tilde{K}^0 + \frac{1}{4}\tilde{K}^2}\Theta(s_Q - 4m_f^2)e^{Y_F(q_1,q_2)}. \qquad (3.2.19)$$

The new lower limit on the photon energy also depends on the total photon momentum, which is not ideal. This can be fixed by setting $\epsilon_f = \delta_f(1 + \tilde{K}^0)$ where $\delta_f \ll 1$. This substitution leads to a new minimum energy for the soft photons, $E_{\min} = \delta_f\frac{\sqrt{s_Q}}{2}(1 + \tilde{K}^0)$. Now we are in a position to introduce some simplifications, as we did in the ISR case, to make Equation (3.2.19) more suited for MC integration.

- To remove any dependence on the photon momentum in s_Q is achieved trivially by replacing $s_Q \to s_X$.

- We drop the mass term in $g\left(\theta_i\right)$ for numerical stability, which leads to a corrective weight $\prod_{i=1}^{\bar{n}} \frac{g(\theta_i)}{\tilde{g}(\theta_i)}$.

- $\frac{1+\tilde{K}^0}{1+\tilde{K}^0+\frac{1}{4}\tilde{K}^2}\Theta(s_Q - 4m_f^2) \to 1$. This simplification was done to remove a complicated dependence on the photon momentum.

- $e^{Y_F(q_1,q_2)} \to e^{\bar{\gamma}\ln\left(\delta_f\right)}$

With these simplifications we arrive at a FSR differential distribution that can be generated from uniform random numbers.

$$\frac{d\mathcal{F}_{\bar{n}}}{\prod_{i=1}^{\bar{n}} dy_i d\cos\theta_i d\phi_i} = e^{\bar{\gamma}\ln(\delta_f)} \left(\frac{\alpha}{2\pi^2}\right)^{\bar{n}} \prod_{i=1}^{\bar{n}} \frac{\Theta(y_i - \delta_f)}{y_i} \tilde{g}\left(\theta_i, \frac{m_f^2}{s_X}\right), \qquad (3.2.20)$$

and the corrective weight for this simplified distribution is given by,

$$w_{\text{FSR}} = e^{\gamma_f \ln(\delta_f(1+\tilde{K}^0)) - \bar{\gamma}\ln(\delta_f)} \frac{1 + \tilde{K}^0}{1 + \tilde{K}^0 + \frac{1}{4}\tilde{K}^2} \Theta(s_Q - 4m_f^2) \prod_{i=1}^{\bar{n}} \frac{g(\theta_i)}{\tilde{g}(\theta_i)}. \qquad (3.2.21)$$

While it is not obvious, it can be shown that the FSR photon multiplicity is again distributed according to a Poissonian. Summing over all photons and integrating Equation (3.2.20) yields,

$$\begin{aligned}
\sum_{\bar{n}}^{\infty} \mathcal{F}_n &= \sum_{\bar{n}}^{\infty} \frac{1}{\bar{n}!} \prod_{i=1}^{\bar{n}} \int_{\delta_f}^1 \frac{dy_i}{y_i} \int_0^{2\pi} \frac{d\phi_i}{2\pi} \int_{-1}^1 d\cos\theta_i \frac{\alpha}{\pi} \tilde{g}\left(\theta_j\right) e^{\bar{\gamma}\ln(\delta_f)} \\
&= \sum_{\bar{n}}^{\infty} e^{\bar{\gamma}\ln(\delta_f)} \frac{1}{\bar{n}!} \left(\bar{\gamma}\ln\frac{1}{\delta_f}\right)^{\bar{n}} = 1
\end{aligned} \qquad (3.2.22)$$

From this it can be seen that the average for the photon multiplicity is $\langle\bar{n}\rangle = \bar{\gamma}\ln\frac{1}{\delta_f}$. Once we know the multiplicity for a given event we can distribute the photon momenta as described in Appendix A.3. To correct the final state momentum for photon emission, we define a frame $Q = \left(\sqrt{s_Q}, 0, 0, 0\right)$ and a frame $X = Q - \sum_i k_i$. We boost the final states into the frame X, then we perform a random Euler rotation, and finally we boost-back the fermions to the frame X. The Euler rotations have no special geometrical meaning, it is just performed to erase the fermions direction before we boost-back to X.

3.2.3   Infrared Boundary for FSR and ISR

In our previous discussions we have described how the multi photon phasespace for initial and final state emissions is generated. We have already introduced infrared domains in which the photons may reside. For the ISR photons the domain Ω_I is defined by rejecting all photons with $k_I^0 < \frac{\sqrt{s}}{2}\epsilon$ and for FSR the domain is defined

by $k_F^0 < \delta_f \left(s_Q + \frac{2 \sum k_F}{Q} \frac{\sqrt{s_Q}}{2} \right)$ where $s_Q = Q^2 = (q_1 + q_2)^2$. Both of these limits are defined in the CMS frame of the corresponding dipole. These two regions need to be combined to avoid any violation of the IR domains. This can be done by choosing δ_f small enough that the FSR domain lies with the ISR domain. This will also require that we remove any photon that resides in $\delta\Omega = \Omega_I \setminus \Omega_F$. This removal process does not come for free. As we are in essence redefining the IR domain the photon phasespace integration will have changed and a new distribution for the MC has to be calculated. The photons in $\delta\Omega$ are not completely hidden as they are still present in the FSR weight.

$$\lim_{k_i \to 0} W_{\mathrm{FSR}}(n, k_1, \cdots, k_i, \cdots, k_n) =$$

$$W_{\mathrm{FSR}}(n - 1, k_1, \cdots, k_{i-1}, k_{i+1}, \cdots, k_n) \frac{g(\theta_i, \frac{m_f^2}{s_Q})}{\tilde{g}(\theta_i, \frac{m_f^2}{s})} \qquad (3.2.23)$$

and even the softest photon contributes to $g/\tilde{g}$. To calculate the effect from the photons in $\delta\Omega$ we evaluate the following integral,

$$\int_{\delta\Omega} \frac{d^3 k}{k^0} \tilde{S}(k) \frac{g(\theta_i, \frac{m_f^2}{s_Q})}{\tilde{g}(\theta_i, \frac{m_f^2}{s})} = 2\alpha Q_f^2 \left(\tilde{B}(\Omega_I; \bar{q}_1, \bar{q}_2) - \tilde{B}(\Omega_F; \bar{q}_1, \bar{q}_2) \right). \qquad (3.2.24)$$

We have multiplied our FSR weight by a corrective factor which removes this additional term.

$$W_{\mathrm{Hidden}} = \exp\left[-2\alpha Q_F^2 \left(\tilde{B}(\Omega_I; \bar{q}_1, \bar{q}_2) - \tilde{B}(\Omega_F; \bar{q}_1, \bar{q}_2) \right) \right.$$

$$\left. +2\alpha Q_F^2 \left(\tilde{B}(\Omega_I; q_1, q_2) - \tilde{B}(\Omega_F; q_1, q_2) \right) \right] \qquad (3.2.25)$$

where $q_{1,2}$ are the final state momenta after the photon emission and $\bar{q}_{1,2}$ are scaled momenta such that $\bar{q}_i^2 = m_i^2 \frac{s_Q}{s}$. The second term in the exponential is used to remove $\tilde{B}(\Omega_F)$ from the original YFS form factor as Ω_I now includes Ω_F. For more detail, see [50] where Jadach et al work this out in great detail.

3.3   Higher-Order Corrections in YFS

The inclusion of exact fixed order calculations in the YFS algorithm is achieved by a multiplicative corrective weight, W_c, which is defined as,

$$
W_C = 1 + \frac{1}{\tilde{\beta}_0^0} \left(\tilde{\beta}_0^1 + \sum_{i=1}^{n_R} \frac{\tilde{\beta}_1^1}{\tilde{S}(k_i)} \right)
$$
$$
+ \frac{1}{\tilde{\beta}_0^0} \left(\tilde{\beta}_0^2 + \sum_{i=1}^{n_R} \frac{\tilde{\beta}_1^1(k_i)}{\tilde{S}(k_i)} + \sum_{\substack{i,j=1 \\ i \neq j}}^{n_R} \frac{\tilde{\beta}_2^2(k_i, k_j)}{\tilde{S}(k_i)\tilde{S}(k_j)} \right) + \frac{1}{\tilde{\beta}_0^0}\mathcal{O}\left(\alpha^3\right) \qquad (3.3.1)
$$

In the $\mathcal{O}\left(\alpha\right)$ expansion, the first term in brackets is the next-to-leading order (NLO) correction, followed in second bracket by the next-to-next-to-leading order (NNLO) correction. While the series can be extended to all orders we have truncated it to $\mathcal{O}\left(\alpha^2\right)_{\text{Prag}}$ for the purpose of this thesis. As discussed in Section 3.1 the $\tilde{\beta}_{n_R}^{n_R+n_V}$ can be constructed using real and virtual corrections to the the born level matrix element M_0^0. Explicit expression in terms of matrix element corrections are displayed below up to $\mathcal{O}\left(\alpha^2\right)$.

$$
\tilde{\beta}_0^0 = M_0^0 M_0^{0*}
$$
$$
\tilde{\beta}_0^1 = M_0^0 M_0^{1*} + M_0^0 M_0^{0*}
$$
$$
\tilde{\beta}_1^1 = \frac{1}{2(2\pi)^3} M_1^{\frac{1}{2}} M_1^{\frac{1}{2}*} - \tilde{S}(k)\tilde{\beta}_0^0
$$
$$
\tilde{\beta}_0^2 = M_0^0 M_0^{2*} + M_0^2 M_0^{0*} + M_0^1 M_0^{1*}
$$
$$
\tilde{\beta}_1^2 = \frac{1}{2(2\pi)^3} \left(M_1^{\frac{3}{2}} M_1^{\frac{1}{2}*} + M_1^{\frac{1}{2}} M_1^{\frac{3}{2}*} \right) - \tilde{S}(k)\tilde{\beta}_1^0
$$
$$
\tilde{\beta}_2^2 = \left(\frac{1}{2(2\pi)^3} \right)^2 M_2^1 M_2^{1*} - \sum_{\substack{i,j=1 \\ i \neq j}}^{n_R} \tilde{S}(k_i)\tilde{\beta}_1^1(k_j) - \tilde{S}(k_i)\tilde{S}(k_j)\tilde{\beta}_0^0 \qquad (3.3.2)
$$

In the remainder of this chapter we will discuss the contributions to Equation (3.3.1) that have been implemented in Sherpa's new YFS module. In particular, we will discuss the matrix element corrections that have been explicitly added in the leading-log (LL) limit. Future implementations will hopefully not have to depend on hard coded corrections but instead use automated tools to calculate the contributions to Equation (3.3.2). Let us now introduce the notation we use. In a typical perturb-

ative calculation higher order correction are included order-by-order in a coupling constants. A fixed order calculation which is said to be $\mathcal{O}\left(\alpha^n\right)$ accurate means that all contributions beyond this are set to zero. However, including exponentiation in the calculation the simple order-by-order picture becomes distorted. This is due to the fact the exponentiation sums up the soft photon emissions to infinite order. As we are also including calculations in the leading-log approximation we need to keep track of which $\alpha^n L^m$ terms we include. So following the notation of [99] we introduce a pragmatic definition of $\mathcal{O}\left(\alpha^n\right)$ and label it $\mathcal{O}\left(\alpha^n\right)_{\mathrm{Prag}}$ which has incomplete sub-leading terms. This new format is depicted in Figure 3.1. As the terms in Fig-
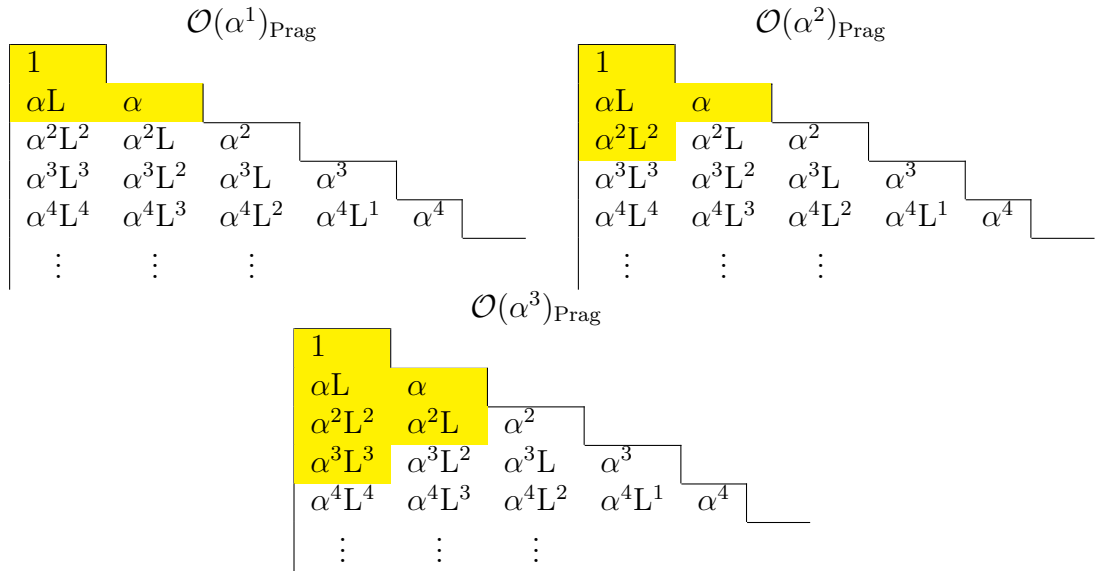
Figure 3.1: Contributions to the leading and sub-leading QED corrections. The first column is the leading logarithmic (LL) contribution, the second column is the next-to-leading (NLL) and so on. We have highlighted the terms that contribute to our pragmatic expansion.

ure 3.1 refer to the accuracy of the βs it is worth mention that the exponentiation is applied to all terms. Particular the first row in Figure 3.1, which is in fact a pure exponentiated calculation, we will sometimes refer to as $\mathcal{O}\left(\alpha^0\right)_{\mathrm{Prag}}$ accurate. If we consider the magnitude of the contributions in Figure 3.1 it can be seen that the numerically important terms should not be summed up row or column wise but instead should be summed diagonally. These corrections have been known for a long time and have been calculated and developed in [40, 100–105]. and the explicit

Process	Order	ISR Corrections	FSR Corrections
$e^+e^- \to f\bar{f}$	$\mathcal{O}\left(\alpha^1\right)_{\text{Prag}}$	R + V	R + V
	$\mathcal{O}\left(\alpha^2\right)_{\text{Prag}}$	RR + RV + VV	RR + RV + VV
$e^+e^- \to VV$	$\mathcal{O}\left(\alpha^1\right)_{\text{Prag}}$	R + V	-
	$\mathcal{O}\left(\alpha^2\right)_{\text{Prag}}$	RR + RV + VV	

Table 3.1: The highest order diagrams included in SHERPA's YFS implementation.

expressions for Equation (3.3.2) can be found in [99]. In Table 3.1 we summarize the corrections that have been implemented. In particular at $\mathcal{O}\left(\alpha^1\right)_{\text{Prag}} = \mathcal{O}\left(\alpha, L\alpha\right)$ the contributing corrections are, the one real photon correction $\tilde{\beta}_1^1$, and loop correction to the Born $\tilde{\beta}_0^1$, which is calculated in the LL limit. For $\mathcal{O}\left(\alpha^2\right)_{\text{Prag}} = \mathcal{O}\left(\alpha, L\alpha, L^2\alpha^2\right)$ the corrections include, the two real photon term $\tilde{\beta}_2^2$, the two loop correction to the Born, $\tilde{\beta}_0^2$, and the one loop one real correction $\tilde{\beta}_1^2$.

Chapter 4

Results

In this chapter we will present numerical results from the YFS implementation in SHERPA. First, we shall compare the total cross section from SHERPA with the results of a separate semi-analytical calculation of Equation (3.1.13). Secondly, we will present a comparison with an existing MC tool, `KKMC` [50, 98], in which YFS resummation has been implemented. Predictions of total cross sections are compared with experimental results from LEP. We will also discuss the production WW and ZH at energies relevant for future colliders.

4.1 Semi-Analytical Approach

We shall briefly present the semi-analytical approach to soft photon resummation and compare the results from this approach with our implementation in SHERPA. As discussed in [99] it can be shown that Equation (3.1.13) can be approximated by relatively simple integrals. This method involves integrating the entire phasespace analytically as far as possible. This will then leave one or two dimensional integrals which can be evaluate using non-MC methods such as numerical quadrature. The non-MC approach was quite popular for predicting simple observables at LEP. For example, it was used to calculate the cross section for $e^+e^- \to f\bar{f}$, including ISR and FSR effects, in tools like TOPAZO [106] and ZFITTER [107]. While the

non-MC approach is far easier to implement than a MC algorithm, it does have significant disadvantages. Generally, they are unable to take into account complex experimental cuts as the phasespace is not explicitly constructed. Improving the perturbative accuracy of the semi-analytical approach is rather complicated, as increasing the multiplicity of the final state makes the analytical integration of the phasespace difficult, if not impossible. Even with these disadvantages the semi-analytical approach can provide an accurate prediction of the total cross section at certain orders. It is therefore a useful independent validation of the MC algorithm. For ISR, the semi-analytical formula can be written as,

$$\sigma = \int_{v_{\min}}^{v_{\max}} dv \left[e^{\frac{\gamma}{4} + \gamma_{\mathrm{Euler}} + \frac{\alpha}{\pi}\left(-\frac{1}{2} + \frac{\pi^2}{3}\right)} \frac{\gamma v^{\gamma-1}}{\Gamma(1+\gamma)} d\sigma_{\mathrm{Born}}(s(1-v)) \left[\mathcal{S} + \mathcal{H}(v)\right] \right] \quad (4.1.1)$$

where $\gamma = \frac{2\alpha}{\pi}\left(\log\frac{s}{m_f^2} - 1\right)$, m_f is the mass of the initial state lepton, Γ is the gamma function and γ_{Euler} is the Euler-Mascheroni constant. The expressions for $\mathcal{S}$ and $\mathcal{H}(v)$ are given in Table 4.2. $d\sigma_{\mathrm{Born}}$ is the spin-averaged differential Born level cross section for $e^+e^- \to f\bar{f}$, which is also integrated over the scattering angle θ. We implemented a non-MC calculation of Equation (4.1.1) in a simple Python program, where the integral was evaluated using adaptive quadrature methods from the SciPy library [108]. The total cross section was calculated at various different $v_{\max}$, a trivial cut that can be applied in the non-MC approach, and was compared against predictions from SHERPA. The input parameters used for both calculations are given in Table 4.1. The lower integration limit, $v_{\min}$, was set to 10^{-5}. The reduction of $v_{\max}$ was truncated at 0.1 as lower values caused numerical instabilities in the python implementation.

The deviation between SHERPA's cross section and the semi-analytical result is given in Figure 4.1. As we can see in the figure there is an excellent agreement for all orders. The deviation between the two implementation is at the 0.1% level. This results, gives us confidence that our prediction for the total cross section is correct. However, it tells us nothing about the differential distributions that are fully generated in SHERPA. In the next section we investigate and validate the full MC approach against

	Mass [GeV]	Width [GeV]
Z	91.1876	2.4952
W	80.385	2.085
H	125	0.00407
e	0.000511	-
μ	0.105	-
$\alpha_{\mathrm{QED}}^{-1}(0)$	137.03599976	

Table 4.1: Electroweak input parameters in the $\alpha(0)$ scheme.
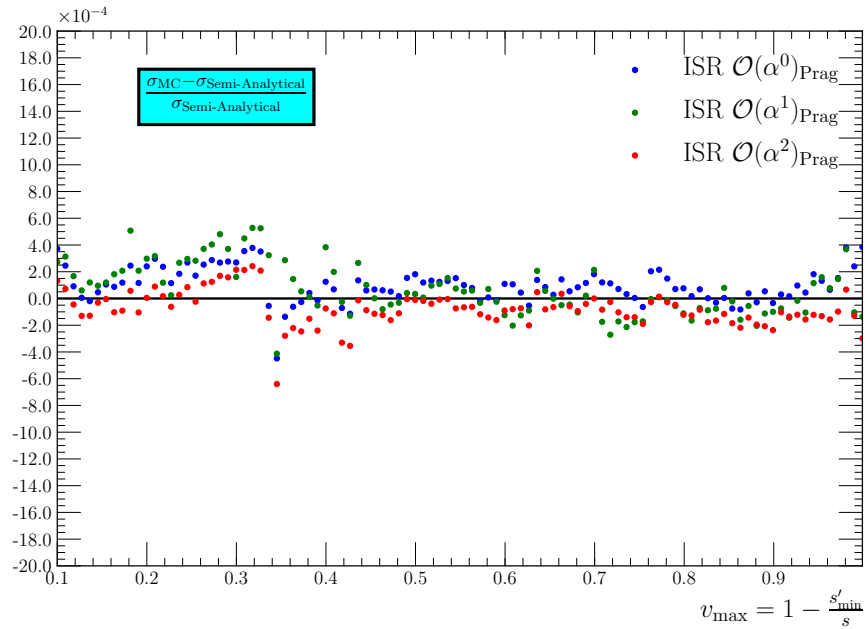
Figure 4.1: Plot of the deviation of the SHERPA cross section from the semi-analytical calculated according to Equation (4.1.1) with increasing cuts on v.

	$\mathcal{S}$	$\mathcal{H}(v)$
$\mathcal{O}(\alpha^0)_{\mathrm{Prag}}$	1	$-\frac{1}{4}\gamma \ln(1-v) - \frac{1}{2}\frac{\alpha}{\pi}\ln^2(1-v)$
$\mathcal{O}(\alpha^1)_{\mathrm{Prag}}$	$1 + \frac{\gamma}{2}$	$v\left(-1+\frac{v}{2}\right) + \gamma\left[-\frac{v^2}{2} - \frac{(1-v)^2}{4}\ln(1-v)\right]$
$\mathcal{O}(\alpha^2)_{\mathrm{Prag}}$	$1 + \frac{\gamma}{2} + \frac{\gamma^2}{8}$	$v\left(-1+\frac{v}{2}\right) + \gamma\left[-\frac{v}{2} - \frac{1+3(1-v)^2}{4}\ln(1-v)\right]$

Table 4.2: Contributions to the functions $\mathcal{S}$ and $\mathcal{H}(v)$ for the semi-analytical approach in Equation (4.1.1).

existing implementation in `KKMC`. In future works, this method will be extended to include FSR effects that can then be used to validate the FSR implementations. It has not been implemented here as the inclusion of FSR is relatively new in SHERPA and will be discussed further in Section 4.2.

4.2   Comparison to `KKMC`

Setup

In the comparison between SHERPA and `KKMC`, we considered the process $e^+e^- \to \mu^+\mu^- + n\gamma$ at the Z-pole energy of $\sqrt{s} = 91.2$ GeV. In this calculation we choose to use the $\alpha(0)$ electroweak scheme. As we are examining the effects of multiple soft photon emissions, $\alpha(0)$ is the natural choice since the QED coupling of soft photons should be evaluated in the Thompson limit. In this scheme the widths of the Gauge bosons are taken to be fixed, $\sin\theta_W$ is calculated from the W and Z masses as $\sin\theta_W = \sqrt{1 - \frac{M_W^2}{M_Z^2}}$. Both the electron and muon masses are included, as required by the YFS formalism. We set the infrared cut-off to be $E_{cut}^\gamma = 1\text{MeV}$. In `KKMC`, we turn off any effects from FSR. For the matrix elements we use the exclusive exponentiation (EEX) implementation in both `KKMC` and SHERPA.

ISR Comparison

Here we will compare results from SHERPA with `KKMC` for initial state radiation, including matrix element corrections up to $\mathcal{O}\left(\alpha^2\right)_{\text{Prag}}$. In Figures 4.2 to 4.4 we plot some key observables related to ISR. In the left plot of Figure 4.2 we compare the number of initial state photons, normalised to unity, generated in SHERPA, compared to the multiplicity generated in `KKMC`. SHERPA and `KKMC` are in excellent agreement with each other to well below the 0.05% level. Next, we show the distribution of the sum of the photon energy $\sum_n E_\gamma$. This plot has a distinct peak at $\frac{\sqrt{s}}{2}$. The energy
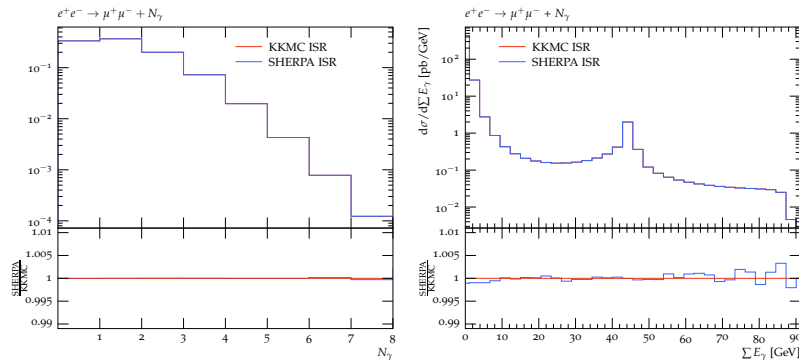
Figure 4.2: The left plot is the total number of soft photons produced by ISR in KKMC and in SHERPA. The plot on the right is the sum of the photon energies, $\sum E_\gamma$, taken in the rest frame of the final state.

$\sqrt{s}$ [GeV]	Born	$\mathcal{O}\left(\alpha^0\right)_{\text{Prag}}$	$\mathcal{O}\left(\alpha^1\right)_{\text{Prag}}$	$\mathcal{O}\left(\alpha^2\right)_{\text{Prag}}$
SHERPA σ [nb]	1.8719	1.3151	1.3755	1.3762
KKMC σ [nb]	1.8719	1.3151	1.3755	1.3762

Table 4.3: Table of total cross sections for $e^+e^- \to \mu^+\mu^-$ production including ISR corrections.

of a single photon is constrained to be less than $\frac{\sqrt{s}}{2}$, so for an event to have a total photon energy beyond this, at least two hard photons are needed.

The next distribution we consider is the invariant mass of the final state particles in Figure 4.3. In the first frame we present the nominal predictions from SHERPA. The blue line represents the exponentiated $\mathcal{O}\left(\alpha^0\right)_{\text{Prag}}$, without any matrix element corrections, the green line is the matched $\mathcal{O}\left(\alpha^1\right)_{\text{Prag}}$ including matrix element correction, and the red represents the $\mathcal{O}\left(\alpha^2\right)_{\text{Prag}}$. SHERPA and KKMC are again in complete agreement at level of 0.1%.

In Figure 4.5 we examine the differences between the individual orders. The distributions are normalized to unity to emphasize the differences in the shape. In the soft limit the all the distribution tend to the same value, while away from the soft limit we see that the $\mathcal{O}\left(\alpha^1\right)_{\text{Prag}}$ distribution is undershooting the highest-order.

In Figure 4.4 we compare the p_T distribution from of the virtual boson at each order. Due to the fully exclusive nature of the YFS formalism, the virtual boson in $e^+e^- \to$
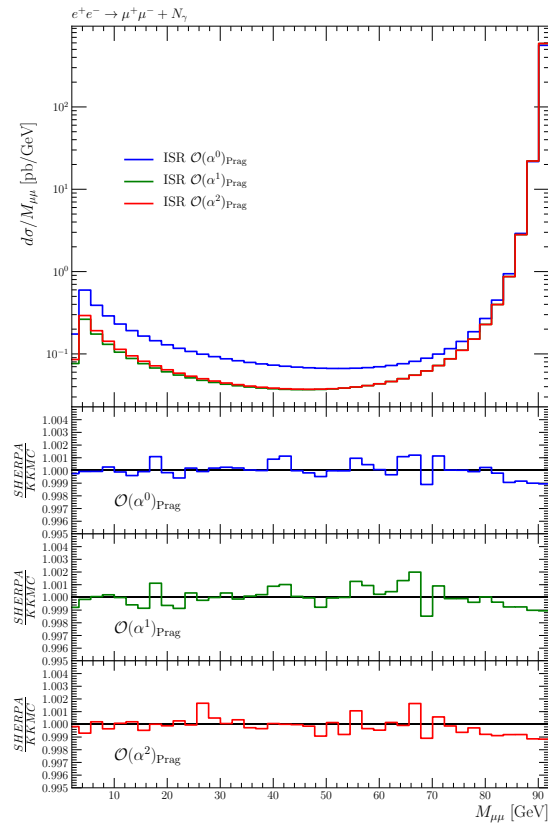
Figure 4.3: Plot of the invariant mass distribution of the final state
particles. The nominal plots from SHERPA are displayed
in the main frame. The sub-plots are the ratios with
respect to KKMC.
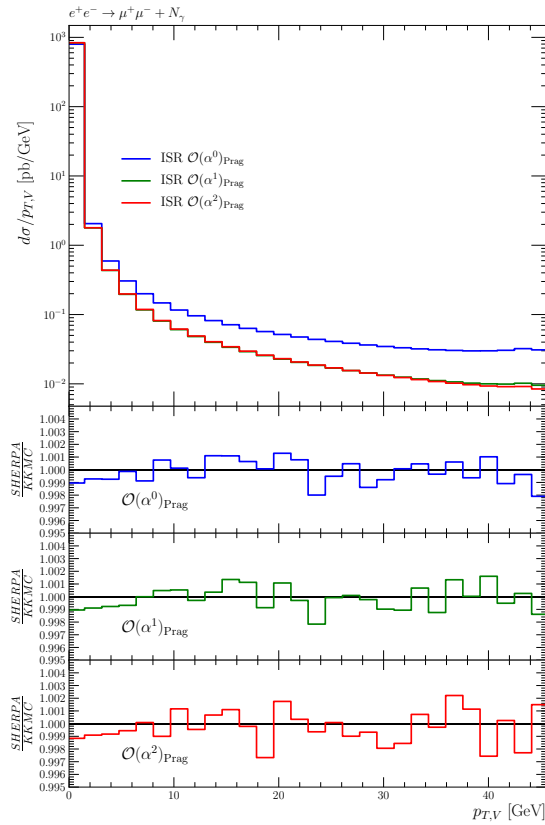
Figure 4.4: Plot of p_T distribution of the virtual boson. The nominal plots from SHERPA are displayed in the main frame. The sub-plots are the ratios with respect to KKMC.
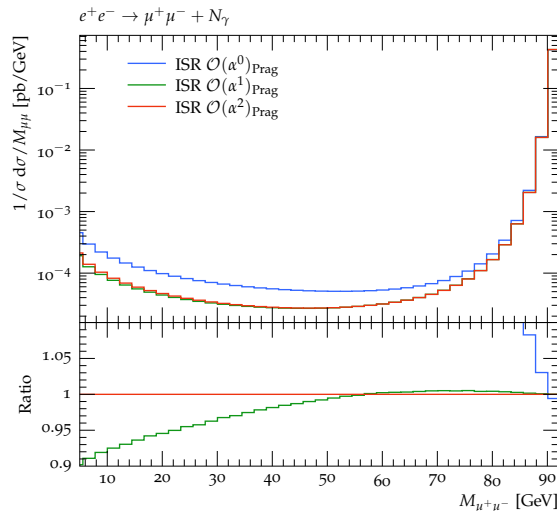
Figure 4.5: Plot of the invariant mass distribution of the final state muons. In the main frame the nominal predictions are shown normalized to unity. The ratio is take with respect to $\mathcal{O}\left(\alpha^2\right)_{\text{Prag}}$
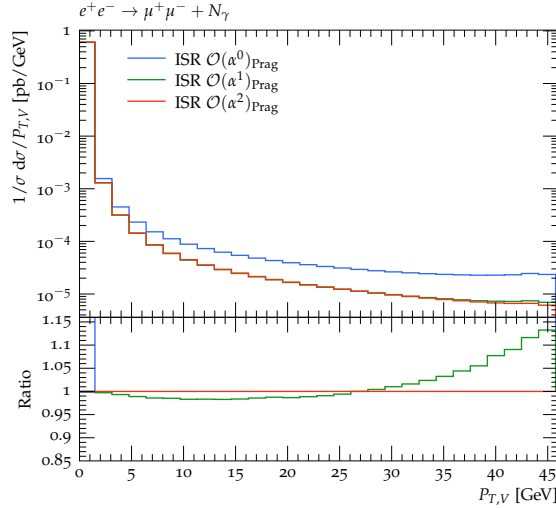
Figure 4.6: Plot of p_T distribution of the virtual boson at different orders. The ratio is taken with respect to $\mathcal{O}\left(\alpha^2\right)_{\text{Prag}}$.

$\mu^+\mu^-$ does have a p_T spectrum. The explicit creation of the real photons cause the initial state momenta to recoil against their emissions. In other inclusive approaches to ISR such a distribution would not be visible as the p_T is fully integrated out. To probe the p_T in the inclusive approach, a matching to a QED shower would need to implemented. We see that the p_T distribution is again in excellent agreement, at the level of 0.1%, between the two generators at all orders. In Figure 4.6 we compare the p_T distributions from SHERPA at different orders. We see that in the first bin there is little deviation between the orders.This bin generally corresponds to events where the photon multiplicity is zero. If there are no photons in an event then there are no higher-order corrections and Equation (3.3.1) reduces to one. The $\mathcal{O}\left(\alpha^0\right)_{\text{Prag}}$ term deviates strongly from the higher-order terms while the $\mathcal{O}\left(\alpha^1\right)_{\text{Prag}}$ term has a small deviation at low p_T it grows to be the order of 10% when compared to $\mathcal{O}\left(\alpha^2\right)_{\text{Prag}}$.

FSR Comparison

Recently, we have attempted to include FSR effects, for $e^+e^- \rightarrow f\bar{f}$, in our YFS algorithm as described in Section 3.2.2. We will present the results that have been obtained so far but the FSR treatment is not as advanced as the ISR. Due to the
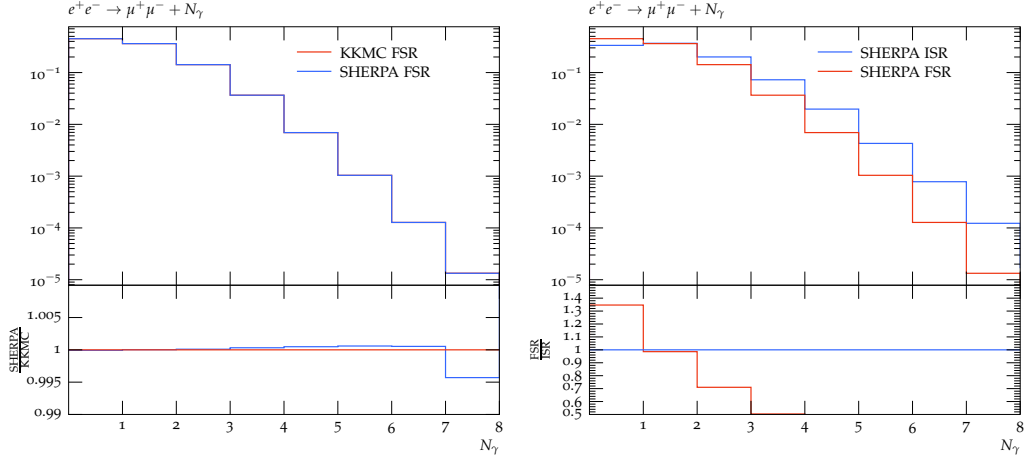
Figure 4.7: In the left plot we have a comparison between KKMC and
SHERPA for FSR multiplicity. On the right, we compare
the multiplicities of ISR and FSR photons at $\mathcal{O}\left(\alpha^0\right)_{\mathrm{Prag}}$

factorised treatment of ISR and FSR in the EEX approach, it is possible to neglect the contribution from ISR. While this is not a phenomenologically important option for e^+e^- physics, it is useful test of our FSR implementation. A similar option exists in KKMC and therefore we can compare FSR only corrections to $e^+e^- \to \mu^+\mu^-$. For the FSR calculation we use the same input parameters as ISR case, namely the parameters in Table 4.1. We are only presenting the results from the $\mathcal{O}\left(\alpha^0\right)_{\mathrm{Prag}}$ simulation. Including the higher-order corrections yield large deviations, sometimes as large as 50%, between KKMC and SHERPA, both in the total cross-section and in the differential distributions. The source of this deviation is believed to be in SHERPA's corrective weight as given by Equation (3.3.1).

In Figure 4.7 we have two plots related to the photon multiplicity. In the first, we are comparing the number of photons emitted by the final state particles between KKMC and SHERPA. The agreement between the two generators is within 0.5%. In the second plot, we compare the number of photons emitted by the initial state and those emitted by the final state. The muons, which are heavier, radiate less photons then the lighter electrons in the initial state. This result expected, as it is well know in electrodynamics that the radiation from a charged particle with mass M is $\propto \frac{1}{M^4}$.
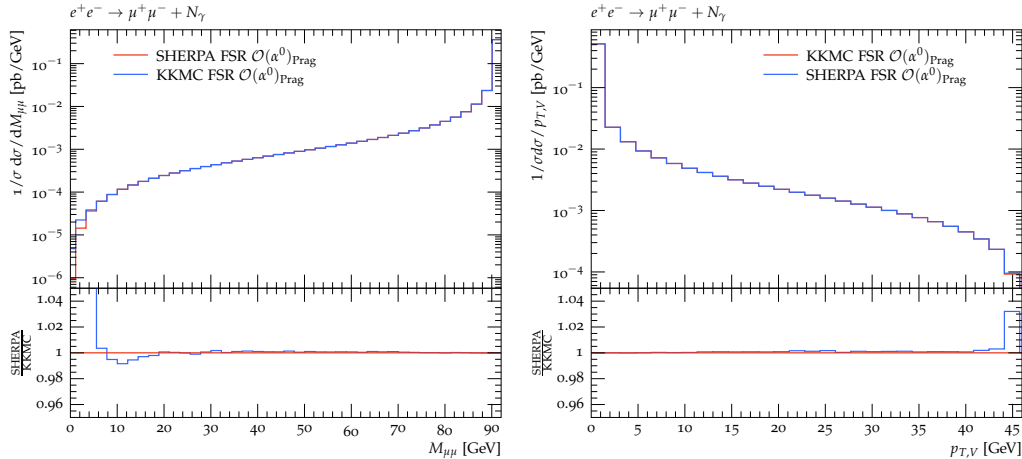
Figure 4.8: In the left plot we have the invariant mass distribution
of the final state particles and on the left we have the
p_T distribution of the exchange boson including effects
from FSR at $\mathcal{O}\left(\alpha^0\right)_{\mathrm{Prag}}$

In Figure 4.8 we have plotted two differential distributions for FSR corrections to
$e^+e^- \to \mu^+\mu^-$. In the first, we consider the invariant mass distribution of the final
state muons. Above 20 GeV there is good agreement between KKMC and SHERPA
but below that we see deviations between the two. The reason for this deviation
has yet to be found but it may be due an unknown phasespace cut missing from
the SHERPA implementation. Similarly, there is generally good agreement between
KKMC and SHERPA for the p_T distribution with the exception of the last bin. These
deviations unfortunately become enhanced when ISR is included as we can see in
Figure 4.9. We do note that for realistic experimental cuts, particular for those at
LEP, the deviation is removed by cuts on $\sqrt{\hat{s}}$ which tended to be greater than 75
GeV.

4.3 W^+W^- Production

In this section we examine the effects of ISR on W^+W^- production at the FCC-
ee collider. At the FCC-ee there is a planned two year run at energies near the
W^+W^- threshold, first at $\sqrt{s} = 157.5$ GeV and followed by a run at $\sqrt{s} = 162.5$
GeV [21]. With a predicted total luminosity of $12ab^{-1}$ it is expected to produce on
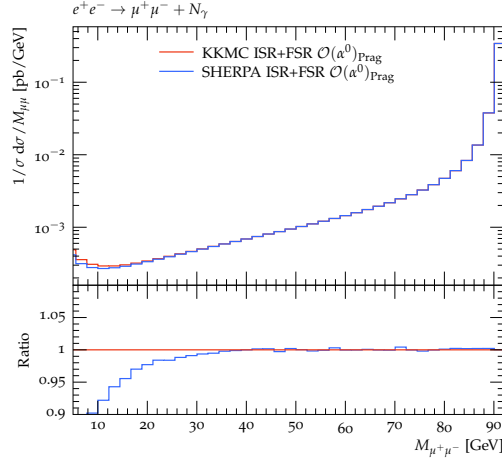
Figure 4.9: Plot of the invariant mass distribution of the final state particles including ISR and FSR resummation.

the order of 10^8 W^+W^-. It is predicted that the fit of the W mass and width from the $e^+e^- \to W^+W^-$ cross section will yield a precision of 0.5 MeV for the mass and 1.2 MeV for the width. At this level of experimental uncertainty it is crucial that the theory uncertainty is not allowed to dominate. It is therefore critical that the emission of soft photons is modelled to the highest possible accuracy.

In simulation of W^+W^- production, we model the ISR using the new YFS implementation in SHERPA and we include fixed-order corrections up to $\mathcal{O}\left(\alpha^2\right)_{\text{Prag}}$. We neglect any photon emissions from a boson line or from the final state. While the ISR corrections are numerically the largest, the FSR terms can be quite sizeable [109] and will need to be taken into account for future Higgs factories. While the interference between ISR and FSR could be neglected at LEP, due to the narrow width of the W boson, these effects will have to be taken into account at a future e^+e^- collider. We also neglect corrective terms due to the final state Coulomb corrections which can be important in threshold production. While this calculation is by no means complete, it is a crucial first step in improving the theoretical modelling of $e^+e^- \to W^+W^-$. We use the G_μ scheme to describe the electroweak input parameters and we have taken the CKM matrix to be diagonal. All mass terms are included for massive particles. We consider the fully inclusive production of W^+W^- including all decay channels and we do not apply any cuts on fiducial phasespace.

	Born	$\mathcal{O}\left(\alpha^0\right)_{\text{Prag}}$	$\mathcal{O}\left(\alpha^1\right)_{\text{Prag}}$	$\mathcal{O}\left(\alpha^2\right)_{\text{Prag}}$
σ [pb]	4.165	2.846	2.990	2.994

Table 4.4: Table of total cross sections for fully inclusive $e^+e^- \to W^+W^-$ production.
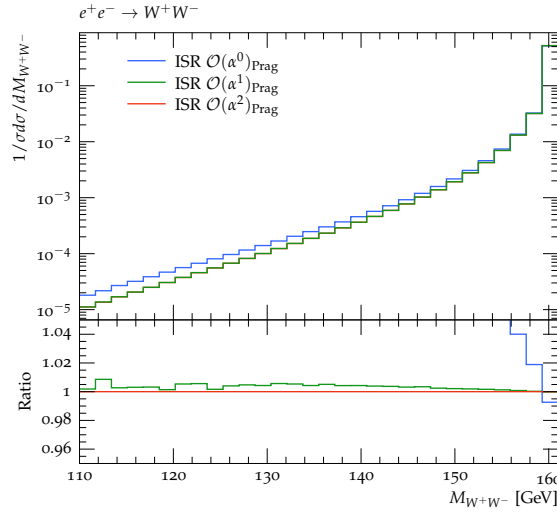
Figure 4.10: Plot of the W^+W^- invariant mass for $e^+e^- \to W^+W^-$ at $\sqrt{s} = 161\text{GeV}$ including effects of ISR up to $\mathcal{O}\left(\alpha^2\right)_{\text{Prag}}$. The ratio is taken with respect to the highest order $\mathcal{O}\left(\alpha^2\right)_{\text{Prag}}$.

The differential distribution of the invariant mass of the W^+W^- pair is shown in Figure 4.10. The distribution has been normalized to unity to emphasis difference in the shape between the different orders. We can see that the exponentiated term, $\mathcal{O}\left(\alpha^0\right)_{\text{Prag}}$, has a large deviation from the higher-order corrections over most of the mass range while in the soft limit the deviation is around a percent. While for the $\mathcal{O}\left(\alpha^1\right)_{\text{Prag}}$ we see a much better convergence to the $\mathcal{O}\left(\alpha^2\right)_{\text{Prag}}$ term. In the soft limit the two predictions exactly agree while for lower mass values there is 0.1-1% level difference. In Table 4.4 we list the total cross-sections for the different orders. We can estimate the uncertainty due to missing higher-order terms by considering the difference between $\mathcal{O}\left(\alpha^2\right)_{\text{Prag}}$ and $\mathcal{O}\left(\alpha^1\right)_{\text{Prag}}$ [110]. We this conservative error is on the order of 0.2%.

4.4 HZ Production

Experimentally measuring the properties of the Higgs-boson to the highest possible precision is a key objective of future lepton-lepton colliders. The main production of Higgs-bosons at e^+e^- colliders proceed through two channels, the Higgsstrahlung reaction $e^+e^- \to ZH$, and WW fusion $e^+e^- \to (W^+W^- \to H)\nu\bar{\nu}$. In this section we will focus on $e^+e^- \to ZH$ production at the purposed collider FCC-ee. The cross section for this process is at a maximum at $\sqrt{s} = 260$ GeV but due to the luminosity profile the event rate per unit time is maximum at $\sqrt{s} = 240$ GeV [21].

We consider the production of Z and Higgs bosons at $\sqrt{s} = 240$ GeV. For the theoretical calculation the electroweak parameters where chosen according the G_μ scheme. The masses and widths of the boson correspond to those inTable 4.1. The ISR includes matrix element corrections up to $\mathcal{O}\left(\alpha^2\right)_{\text{Prag}}$. The total cross-section predictions are given in Table 4.5. From this we can see that the inclusion ISR decreases the total cross-section by 18-20%. The error estimate, due to missing higher-order QED corrections, is found to be of the order 0.2%. The ZH threshold mass is plotted in Table 4.5, where we consider the Z decaying to muons and the

	Born	$\mathcal{O}\left(\alpha^0\right)_{\text{Prag}}$	$\mathcal{O}\left(\alpha^1\right)_{\text{Prag}}$	$\mathcal{O}\left(\alpha^2\right)_{\text{Prag}}$
σ [pb]	0.2532	0.2046	0.2138	0.2141

Table 4.5: Table of total cross sections for fully inclusive $e^+e^- \rightarrow ZH$ production.
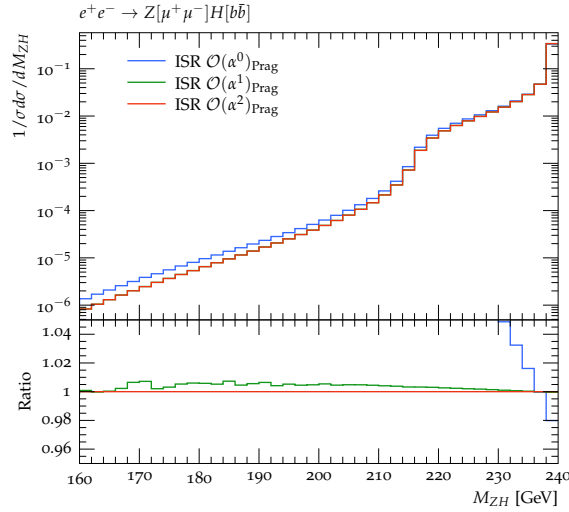
Figure 4.11: Plot of the ZH invariant mass for $e^+e^- \rightarrow Z[\mu^+\mu^-]H[b\bar{b}]$ at $\sqrt{s} = 240$ GeV including effects of ISR up to $\mathcal{O}\left(\alpha^2\right)_{\text{Prag}}$. The ratio is taken with respect to the highest order $\mathcal{O}\left(\alpha^2\right)_{\text{Prag}}$.

Higgs to $b\bar{b}$. The $\mathcal{O}\left(\alpha^0\right)_{\mathrm{Prag}}$ is larger than the higher-order predictions away from the soft limit, again showing that the exponentiation alone is not a sufficient description of ISR. The higher-order corrections, $\mathcal{O}\left(\alpha^1\right)_{\mathrm{Prag}}$ and $\mathcal{O}\left(\alpha^2\right)_{\mathrm{Prag}}$, are in agreement in the soft limit while away from this limit there is a small deviation.

4.5   Comparison to Data

In this section, we will present a comparison of predictions from SHERPA to data taken at LEP. The data we will present will only contain leptonic final states. This will allows us to test the the YFS implementation in a cleaner environment. For processes that have hadronic final states can introduce other systematic uncertainties, that we wish to neglect.

$e^+e^- \to f\bar{f}$
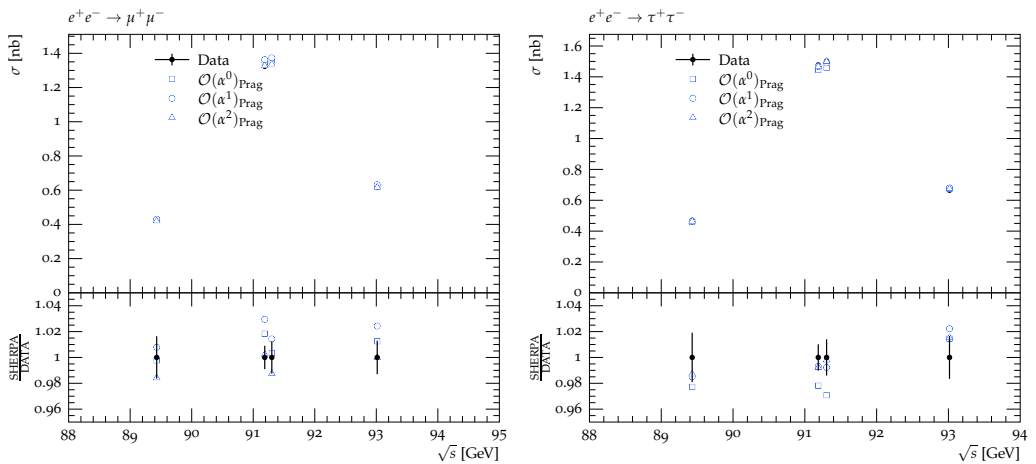
Figure 4.12: Plot of the total cross section of $e^+e^- \to \mu^+\mu^-/\tau^+\tau^-$ as predicted by SHERPA including YFS resummation for ISR matched up to $\mathcal{O}\left(\alpha^2\right)_{\mathrm{Prag}}$ compared to data from DELPHI [111].

In Figure 4.12 and Tables 4.6 and 4.7 we present the total cross section predictions for the inclusive fermion-antifermion production at energies around the Z pole. We call these events inclusive as they include the Z resonance while observables
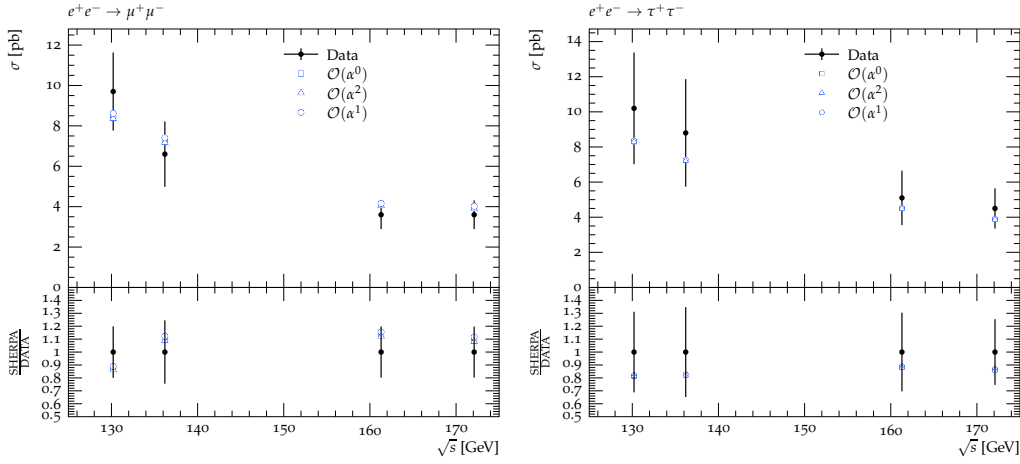
Figure 4.13: Plot of the total cross section of $e^+e^- \to \mu^+\mu^-/\tau^+\tau^-$ as predicted by SHERPA including YFS resummation for ISR matched up to $\mathcal{O}\left(\alpha^2\right)_{\mathrm{Prag}}$ compared to data from DELPHI [112]. This represents the events that satisfy $\frac{M_{f\bar{f}}}{\sqrt{s}} \geq 0.85$.
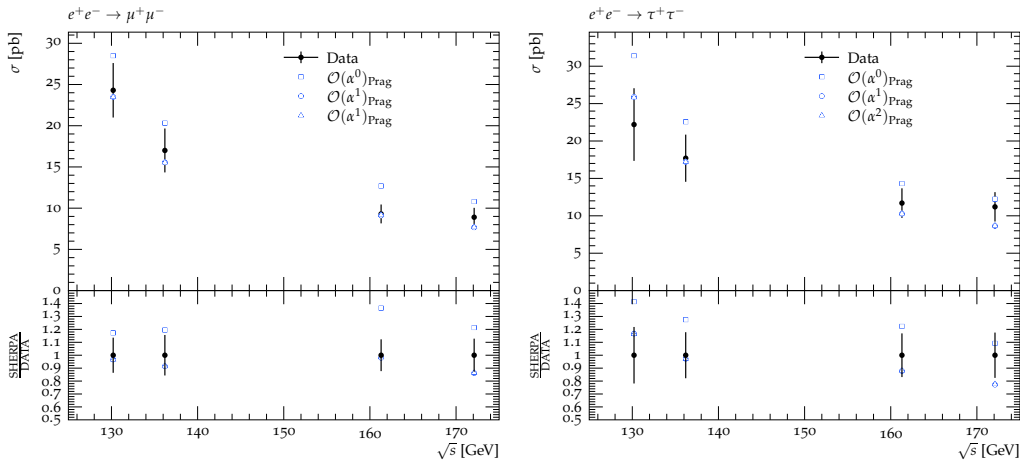
Figure 4.14: Plot of the total cross section of $e^+e^- \to \mu^+\mu^-/\tau^+\tau^-$ as predicted by SHERPA including YFS resummation for ISR matched up to $\mathcal{O}\left(\alpha^2\right)_{\mathrm{Prag}}$ compared to data from DELPHI [112]. This represents events that satisfy $M_{f\bar{f}} \geq 75\mathrm{GeV}$.

$\sqrt{s}$ [GeV]	$\mathcal{O}\left(\alpha^0\right)_{\mathrm{Prag}}$	$\mathcal{O}\left(\alpha^1\right)_{\mathrm{Prag}}$	$\mathcal{O}\left(\alpha^2\right)_{\mathrm{Prag}}$	DELPHI
89.431	0.426	0.430	0.420	0.427 ± 0.007
91.1187	1.348	1.363	1.327	1.324 ± 0.012
91.1302	1.358	1.373	1.336	1.354 ± 0.017
93.3015	0.624	0.631	0.616	0.617 ± 0.008

Table 4.6: Table of total cross sections, in units of nb, for $e^+e^- \to \mu^+\mu^-$

which do not are labelled exclusive. The theoretical predictions are calculated using SHERPA including YFS resummation for both initial and final states, which for ISR is matched up to $\mathcal{O}\left(\alpha^2\right)_{\mathrm{Prag}}$. The processes that are considered are, $e^+e^- \to \mu^+\mu^-$ and $e^+e^- \to \tau^+\tau^-$. The Bhabha scattering process, $e^+e^- \to e^+e^-$, is not included in this analysis due to the incorrect treatment of T-channel divergence in SHERPA. The reference data is taken from the DELPHI experiment [111–113] unless otherwise stated. To accurately compare with data we will need to apply cuts to the fiducial phasespace corresponding to experimental cuts. For $e^+e^- \to f\bar{f}$ the following cuts were applied

- For $e^+e^- \to \mu^+\mu^-$, the highest muon momentum had to be at least 30 GeV.

- The polar angle of the fermions was required to be in the region of $20^\circ \leq \theta_\mu \leq 120^\circ$.

- For the inclusive events the invariant mass had to satisfy $M_{\mathrm{inv}}(f\bar{f}) > 75$ GeV and for exclusive events $\frac{M_{\mathrm{inv}}(f\bar{f})}{E_{cm}} > 0.85$

We can see from Figure 4.12 that there is excellent agreement for the $\mu^+\mu^-$ finals for orders greater than $\mathcal{O}\left(\alpha^1\right)_{\mathrm{Prag}}$. We can see that at $\sqrt{s} = 91.1187$ GeV the resummation alone, i.e. $\mathcal{O}\left(\alpha^0\right)_{\mathrm{Prag}}$, and the first matched term, i.e. $\mathcal{O}\left(\alpha^1\right)_{\mathrm{Prag}}$, are insufficient to replicate the experimental results. The $\mathcal{O}\left(\alpha^0\right)_{\mathrm{Prag}}$ calculation deviates from the experimental value, including the error, by $\approx 1.7\%$. There is a larger deviation for the $\mathcal{O}\left(\alpha^1\right)_{\mathrm{Prag}}$ term by $\approx 3.1\%$

$\sqrt{s}$ [GeV]	$\mathcal{O}\left(\alpha^0\right)_{\mathrm{Prag}}$	$\mathcal{O}\left(\alpha^1\right)_{\mathrm{Prag}}$	$\mathcal{O}\left(\alpha^2\right)_{\mathrm{Prag}}$	DELPHI
89.431	0.459	0.463	0.464	0.470 ± 0.009
91.1187	1.444	1.467	1.466	1.477 ± 0.015
91.1302	1.458	1.490	1.500	1.502 ± 0.021
93.3015	0.674	0.670	0.675	0.665 ± 0.011

Table 4.7: Table of total cross sections, in units of nb, for $e^+e^- \rightarrow \tau^+\tau^-$

$\sqrt{s}$ [GeV]	$\mathcal{O}\left(\alpha^0\right)_{\mathrm{Prag}}$	$\mathcal{O}\left(\alpha^1\right)_{\mathrm{Prag}}$	$\mathcal{O}\left(\alpha^2\right)_{\mathrm{Prag}}$	DELPHI
130.2	8.5	8.6	8.3	9.7 ± 1.9
136.2	7.3	7.4	7.2	6.6 ± 1.6
161.3	4.1	4.1	4.0	3.6 ± 0.7
172.1	4.0	4.0	3.9	3.6 ± 0.7

Table 4.8: Table of total cross sections, in units of pb, for $e^+e^- \rightarrow \mu^+\mu^-$

We also compare the cross sections for exclusive $e^+e^- \rightarrow f\bar{f}$ production in the range 130 to 172 GeV. The comparison to data is presented in Figures 4.13 and 4.14. Again, we see quite good agreement between the theory and experiment with the exception of the $\tau^+\tau^-$ predictions at 172.1 GeV. While the higher order terms agree with the experimental data, the exponentiated only term overshoots the data by a small margin. This deviation is not present in Figure 4.13 which is not surprising. The deviation between $\mathcal{O}\left(\alpha^0\right)_{\mathrm{Prag}}$ and the higher term is more pronounced as $\sqrt{s'}$ decreases. Therefore the stricter cut of $\frac{M_{f\bar{f}}}{\sqrt{s}} \geq 0.85$ will reduce differences between the different orders.

$e^+e^- \rightarrow W^+W^- \rightarrow \ell\nu_\ell\ell'\nu_{\ell'}$

In this section we explore the leptonic decays of $e^+e^- \rightarrow W^+W^-$ and compare it to measurements made by the DELPHI experiment [113] from 161 GeV to 209 GeV. For this calculation we only consider three doubly resonant Feynman diagrams, namely the so called CC03 [114]. These consist of two s-channel exchanges, γ and Z, and

$\sqrt{s}$ [GeV]	$\mathcal{O}\left(\alpha^0\right)_{\mathrm{Prag}}$	$\mathcal{O}\left(\alpha^1\right)_{\mathrm{Prag}}$	$\mathcal{O}\left(\alpha^2\right)_{\mathrm{Prag}}$	DELPHI
130.2	8.3	8.4	8.3	10.2 ± 3.1
136.2	7.2	7.3	7.2	8.8 ± 3.1
161.3	4.5	4.5	4.5	5.1 ± 1.5
172.1	3.9	3.8	3.9	4.5 ± 1.1

Table 4.9: Table of total cross sections, in units of pb, for $e^+e^- \rightarrow \tau^+\tau^-$
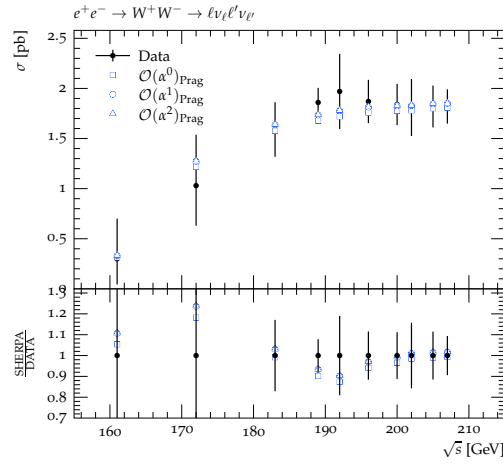
Figure 4.15: Plot of the total cross section of $e^+e^- \rightarrow W^+W^- \rightarrow \ell\nu_\ell\ell'\nu_{\ell'}$ as predicted by SHERPA including YFS resummation matched up to $\mathcal{O}\left(\alpha^2\right)_{\mathrm{Prag}}$. The reference data is from DELPHI [113].

a t-channel ν exchange. Given that CC03 is subset of the full $e^+e^- \rightarrow 4f$ set, it is gauge dependent but due to the small energies at LEP this dependence produces a negligible effect [110].

For the numerical set-up we chose our electroweak parameter corresponding to the G_μ scheme. We only include ISR corrections up to $\mathcal{O}\left(\alpha^2\right)_{\mathrm{Prag}}$. To provide an accurate description of the experimental results we implemented the following cuts. The most energetic photon had to have an energy less than $0.25\sqrt{s}$ and the angle in the plane perpendicular to the beam axis between the charged particles system and the most energetic photon was required to be less than 170°. Finally, the energy of the charged particles had to be greater than $0.04\sqrt{s}$ and the energy of the particles with $|\cos(\theta)| < 0.9$ had to exceed $0.06\sqrt{s}$.

$\sqrt{s}$ [GeV]	$\mathcal{O}\left(\alpha^0\right)_{\text{Prag}}$	$\mathcal{O}\left(\alpha^1\right)_{\text{Prag}}$	$\mathcal{O}\left(\alpha^2\right)_{\text{Prag}}$	DELPHI
161	0.30	0.32	0.32	$0.3^{+0.3}_{-0.4}$
172	1.22	1.27	1.28	$1.03^{+0.5}_{-0.39}$
183	1.57	1.64	1.64	$1.59^{+0.26}_{-0.26}$
189	1.68	1.74	1.74	$1.86^{+0.14}_{-0.14}$
192	1.72	1.78	1.78	$1.97^{+0.37}_{-0.37}$
196	1.76	1.81	1.82	$1.87^{+0.21}_{-0.21}$
200	1.78	1.83	1.83	$1.84^{+0.2}_{-0.2}$
202	1.79	1.83	1.83	$1.81^{+0.28}_{-0.28}$
205	1.80	1.85	1.85	$1.82^{+0.2}_{-0.2}$
207	1.81	1.85	1.85	$1.82^{+0.16}_{-0.16}$

Table 4.10: Table of total cross sections, in units of pb, for ee $\rightarrow$ $W^+W^- \rightarrow \ell\nu_\ell\ell'\nu_{\ell'}$

The results from SHERPA is compared with data from DELPHI in Table 4.10 and fig. 4.15. Our cross section predictions agree with the data at all energies. We see that the higher-order corrections increase the cross sections when compared to $\mathcal{O}\left(\alpha^0\right)_{\text{Prag}}$ and they remain stable with respect to each other. It is worth noting that the differences between $\mathcal{O}\left(\alpha^1\right)_{\text{Prag}}$ and $\mathcal{O}\left(\alpha^2\right)_{\text{Prag}}$ are well below the experimental error and are not displayed in Table 4.10.

Chapter 5

Conclusion

In this part, we have presented the theoretical formulation of the YFS resumma-tion for both real and virtual photons and shown that all logarithms due to the emission of soft photons can been resummed to all orders in QED. A method for systematically improve the accuracy of this method, by the inclusion of higher-order matrix elements, was introduced and we discussed a pragmatic implementation of these corrections. We have implemented this resummation in a new SHERPA mod-ule, YFS++, and we have described, in detail, the algorithm for the resummation of ISR in a process independent manner. We also describe an algorithm for the resummation of FSR in the process $e^+e^- \to f\bar{f}$.

For both the ISR and FSR, the treatment of the multi-photon phasespace has been done in a fully analytical manner and all simplifications have been corrected for in the Monte Carlo. The photon momenta are explicitly constructed and are distributed according to the YFS eikonals. We have also shown how the YFS resummation can be matched to higher order corrections in a systematic way. These corrections, in the LL limit, have been explicitly presented in a form that agrees with existing tools, in particular `KKMC`. The are two main reasons for our choice of corrections. The first is motivated purely by physics. The inclusion of these terms are necessary to reach the required precision desired by future experiments. While the inclusion of these terms brings the precision to the level of $0.1 - 0.5\%$ further improvements will be needed

as discussed in Chapter 1. The second reason we chose these distributions is that they are exactly the ones implemented in KKMC. This mirroring of their approach will allow us to test our implementation of YFS against their code. The results of this comparison has been presented in Chapter 4. The ISR resummation in SHERPA and in KKMC's has been shown to be in agreement to within 0.1% of each other up to $\mathcal{O}\left(\alpha^2\right)_{\mathrm{Prag}}$.

Part II

Precision Simulations for

HL/HE-LHC

Chapter 6

V+jets Predictions for Future Hadron Colliders

6.1 Introduction

A powerful probe for Dark Matter (DM) searches at hadronic colliders are high-energy jets recoiling against missing transverse energy (MET) [115]. MET is a crucial experimental measurement, that is used in the identification and study of Standard Model (SM) W or Z Bosons. As well as being a powerful probe for DM, MET is omnipresent in nearly all BSM searches at the LHC and will continue to be a feature at the future hadron colliders [36, 116–118] experiments. These searches will require precise control of the relevant backgrounds, such as $Z(\nu\bar{\nu})$ + jet, in the signal region. The $Z(\nu\bar{\nu})$ + jet can be extrapolated, using precise theoretical calculations, from the $Z(\ell^+\ell^-)$ + jet, $W(\ell\nu)$ + jet and γ + jet data taken in the control regions. The dominant background to these searches is $Z(\nu\bar{\nu})$ + jet, followed by $W(\ell\nu)$ + jet. Unfortunately, the former can be limited by the statistics due to the large branching ratio of Z boson to neutrinos when compared to the $Z \rightarrow \ell^+\ell^-$ branching ratio. However, the $W(\ell\nu)$ + jet channel provides larger statistics which will make it possible to access higher p_T ranges. The accurate measurements of visible vector boson signatures can provide experimental constraints on $Z(\nu\bar{\nu})$ + jet
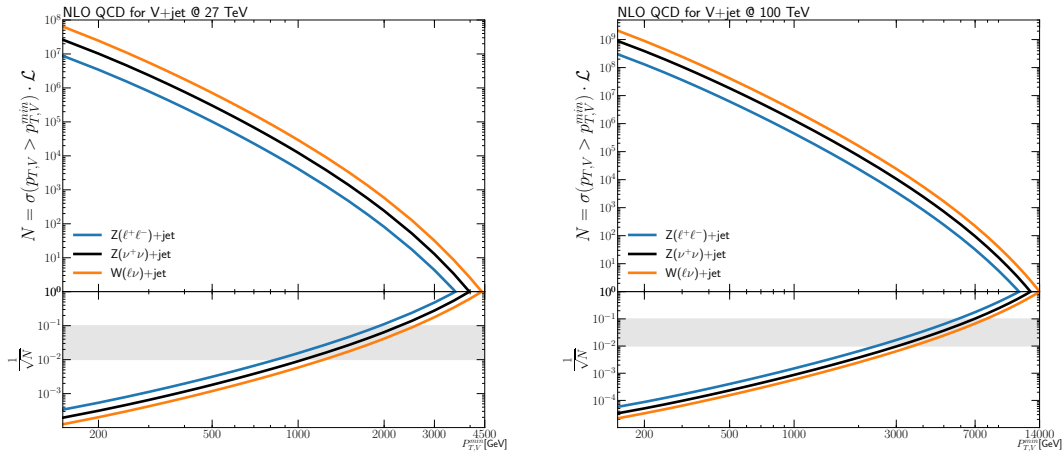
Figure 6.1: Event rates for W/Z+jets as a function of the minimum p_T of the production of W/Z + jet at the HE-LHC and FCC-hh including the fiducial cuts. The lower plot represents the statistical uncertainty based on $\frac{1}{\sqrt{N}}$. The grey band represents the 1-10% range. The luminosity $\mathcal{L}$ is assumed to be 3000fb^{-1} for the HE-LHC and 15 ab^{-1} for FCC-hh.

production at large MET. For example, the production of $Z(\ell^+\ell^-)$ + jets provides the most direct and reliable estimates for $Z(\nu\bar{\nu})$ + jets. In Figure 6.1, we show the expected event rates for W/Z + jets at the HE-LHC/FCC-hh. The $Z(\ell^+\ell^-)$ + jets allows an estimate of the the $Z(\nu\bar{\nu})$ + jets rates at an accuracy below 1% up to 800 GeV, for the HE-LHC, and up to 2.5 TeV for the FCC-hh. The $W(\ell\nu)$ + jets can extend this range to 1.2 TeV and 3.8 TeV respectively. These extrapolations will require precise control over the shape of the distributions. The choice of inputs for the theory calculation, for example the choice of factorization and renormalization scales, can effect the shape of the p_T distributions and hence effect the extrapolation. In the next sections we will present our approach to calculating scale uncertainties.

6.2   Monte Carlo Reweighting

The reweighting of MC samples is a method of combining MC calculations, at different levels of theory, to account for their respective uncertainties in a simple system-

atic way. Mathematically, the reweighting of a generic observable can be expressed
as,

$$\frac{\mathrm{d}}{\mathrm{d}x}\frac{\mathrm{d}}{\mathrm{d}\vec{y}}\sigma^{(V)}(\eta_{\mathrm{MC}}, \eta_{\mathrm{TH}}) \approx \frac{\mathrm{d}}{\mathrm{d}x}\frac{\mathrm{d}}{\mathrm{d}\vec{y}}\sigma_{\mathrm{MC}}^{(V)}(\eta_{\mathrm{MC}})\left(\frac{\frac{\mathrm{d}}{\mathrm{d}x}\sigma_{\mathrm{TH}}^{(V)}(\eta_{\mathrm{TH}})}{\frac{\mathrm{d}}{\mathrm{d}x}\sigma_{\mathrm{MC}}^{(V)}(\eta_{\mathrm{MC}})}\right). \qquad (6.2.1)$$

In our case of V+jet production, the variable x corresponds to the vector boson p_T,
and $\vec{y}$ are the remaining differential variables. The labels MC and TH represent the
Monte Carlo and higher-order predictions respectively. η_{MC} and η_{TH} are nuisance
parameters that parametrise the corresponding uncertainties. In the analysis of the
uncertainties the MC uncertainties must be correlated across the numerator and
denominator in Equation (6.2.1) but they can be kept uncorrelated across different
processes with the exception of $Z(\ell^+\ell^-)$+jet and $Z(\nu\bar{\nu})$+jet. An advantage to this
reweighting is that the individual terms on the r.h.s of Equation (6.2.1) do not
need to be calculated with the same set-up. Only the definition and binning of the
observable x needs to be consistent in all three terms. There are two conditions that
need to be fulfilled in order to ensure an optimal combination of MC and higher-order
calculations. The theory calculations should describe the differential distributions
in the reweighting with a higher precision, or at least equal, when compared to the
MC sample.

$$\Delta\left(\frac{\mathrm{d}}{\mathrm{d}x}\sigma_{\mathrm{TH}}^{(V)}\right) \leq \Delta\left(\frac{\mathrm{d}}{\mathrm{d}x}\sigma_{\mathrm{MC}}^{(V)}\right). \qquad (6.2.2)$$

It is worth noting that in some cases a particular choice of observable x may not
guarantee that Equation (6.2.2) holds, in particular when using state-of-the-art pre-
dictions. In fact, there are a range of observables for which MC is more accurate
than TH. For example, MC better describes the low p_T region by resumming the
logarithms associated with the emission of soft partons. MC also provides a more
accurate description of multi-particle emissions, and it provides a prediction for the
decay of hadrons, all of which are not present in the fixed-order calculation. Ideally
the variable x should have minimal dependence on the above MC aspects that are
not present in the higher order calculations. A natural choice for us is the p_T of the
vector-boson which has a minimal sensitivity to the multi-jet emissions. The region

	Mass [GeV]	Width [GeV]
Z	91.1876	2.4955
W	80.385	2.0897
H	125	0.0
t	173.2	1.339

Table 6.1: Electroweak input parameters for V+jet Study

in which the vector-bosons p_T is low, $p_T^V \ll m_V$, should be excluded to ensure that Equation (6.2.2) holds. Furthermore, any non-perturbative contribution from the MC, e.g hadronization, hadron decays, MPI and UE, should not be included in the variable x.

These considerations are by no means universal. They are presented here as we are discussing searches for dark matter based on the inclusive MET distributions. A more exclusive search would of course introduce more subtleties for example, if a search was sensitive to the tails of inclusive jet-p_T or H_T distributions the lack of multi-jet emissions, which provide a large contribution to the tails, can be a serious issue and for such a search multi-jet merging should be employed [119].

6.3 Input Parameters

In this section we provide the input parameters used in the theoretical calculation. The mass and widths of the SM parameters are stated in Table 6.1. The complex mass scheme [120] is used to describe all unstable particles, where the widths are absorbed into the renormalised masses,

$$\mu_i^2 = M_i^2 - i\Gamma_i M_i, \quad \text{for } i = W, Z, t. \tag{6.3.1}$$

The EW couplings are derived from the gauge-boson masses and the Fermi constant, $G_\mu = 1.16637 \times 10^{-5} \text{GeV}^{-2}$, using

$$\alpha = \left| \frac{\sqrt{2} \sin^2 \theta_w \mu_W G_\mu}{\pi} \right|, \tag{6.3.2}$$

and the weak mixing angle is given by,

$$\sin^2\theta_w = 1 - \cos^2\theta_w = 1 - \frac{\mu_W^2}{\mu_Z^2}, \tag{6.3.3}$$

which is complexed valued. The G_μ scheme is the preferred choice for W/Z + jet production, as it provides an optimal description of pure SU(2) interactions.

The CKM matrix is taken to be diagonal. This choice is justifiable as the difference with respect to a non-diagonal CKM matrix for LO and NLO W + jet production is $\approx 5\%$. The PDF set that was used is the NNPDF31_nnlo_as [121–123] which include supplementary QED corrections. To be consistent with the PDF's five-flavour scheme, b-quarks are treated as massless and diagrams with initial state b-quarks are taken into account. All light quarks are treated as massless. The strong coupling used in the matrix element calculation are taken from the PDFs. Again, to ensure consistency the decoupling scheme is used to renormalise the top-quark loops, which are included at NLO. At NNLO QCD no top-quark loops are present in the calculation.

6.3.1 Physical Objects

Charged Leptons

Physical distributions associated with leptons, such as their p_T, are known to be highly sensitive to the treatment of QED radiation. To reduces this sensitivity all leptons are "dressed". This means that the leptons must be recombined with collinear photons that lie within a cone defined as

$$\Delta R_{\ell\gamma} = \sqrt{\Delta\phi_{\ell\gamma}^2 + \Delta\eta_{\ell\gamma}^2} < R, \tag{6.3.4}$$

where R is the radius of recombination which is chosen to be $R = 0.1$. This choice will capture most of the collinear final state photons and will reduce the contribution from large angle photons to a negligible level. The W and Z bosons four momentum

are constructed from the dressed leptons in the final state. In line with standard experimental practice, both electrons and muons are dressed.

Neutrinos

At the parton level only neutrinos that originate from the decay of a vector boson are considered in the calculations of $pp \rightarrow \ell\ell/\ell\nu/\nu\bar{\nu}$+jet. In Monte Carlo samples neutrinos can arise from the decays of hadrons and to avoid any bias such neutrinos should not be included at the Monte Carlo truth level.

QCD Partons

To reduce the bias between the modelling of jets in the MC simulation and the perturbative calculations, reweighting and theory calculations should be performed with inclusive vector-boson p_T. In this study we do not impose any jet definition or jet cuts and all our predictions.

W and Z

The W and Z bosons four momenta are defined as

$$p^{\mu}_{W^{\pm}} = p^{\mu}_{\ell^{\pm}} + p^{\mu}_{\nu_{\ell^{\pm}}}, \quad p^{\mu}_{Z} = p^{\mu}_{\ell^{+}} + p^{\mu}_{\ell^{-}}, \tag{6.3.5}$$

where, as stated before, the leptons and neutrinos are the result of W and Z decays.

6.3.2 Computational Framework

For the calculation of the $Z/W^{\pm}$+jet cross-sections we employed the most accurate calculations available. The fixed-ordered LO and NLO are calculated using SHERPA [124]+OPENLOOPS [125]. SHERPA provides the Born and real-subtracted amplitudes while the virtual amplitudes are calculated by OPENLOOPS, which uses tensor reduction algorithms provide by COLLIER [126] or CUTTOOLS [127]. The

process	extra cuts	observable
$pp \to \ell^+ \nu_\ell + \text{jet}$	none	$p_{T,\ell^+\nu_\ell}$
$pp \to \ell^- \bar{\nu}_\ell + \text{jet}$	none	$p_{T,\ell^-\bar{\nu}_\ell}$
$pp \to \ell^+ \ell^- + \text{jet}$	$m_{\ell\ell} > 30\,\text{GeV}$	$p_{T,\ell^+\ell^-}$

Table 6.2: Extra selection cuts, and observables for the various V + jet processes.

NNLO QCD predictions, for both $pp \to Z + \text{jet}$ and $pp \to W + \text{jet}$, have been obtained from the parton-level generator NNLOJET, which can calculate fully differential distributions at NNLO using the antenna subtraction formalism [128–136].

Cuts

The Monte Carlo calculations were performed in a fully inclusive V+Jet set-up with a single cut on the boson p_T,

$$p_{T,V} > 50\text{GeV}, \quad \text{for} \quad V = W^\pm, Z. \tag{6.3.6}$$

This cut is essential to ensure the perturbative calculation does not suffer due to a lack of QCD resummation. For the final state leptons and MET there are no cuts on the p_T or the rapidity and there are no restrictions on QCD radiation in the region of the leptons and MET. The process specific cuts for the differential predictions are summarised in Table 6.2. For $pp \to \nu\bar{\nu}$ all three neutrino flavours are taken into account. For the leptonic decaying W and Z bosons only a single lepton flavour is used which for this analysis is the electron.

An additional cut is applied to the invariant mass of the $\ell^+\ell^-$ system. This is used to avoid far off-shell contributions, especially from $\gamma \to \ell^+\ell^-$ at low invariant mass. The low choice of $m_{\ell^+\ell^-} > 30GeV$ is chosen to minimise the cross section loss due to photon radiation, which will shift events from the Z-peak region to a lower mass region.

6.4   Higher-Order QCD Predictions

Predictions are provided, where possible, at NNLO QCD accuracy. However, to accurately analyse the theoretical uncertainties, LO and NLO QCD contributions are calculated and presented. It is also useful to introduce a K-factor, $K_{N^kLO}^{(V)}(x, \boldsymbol{\mu})$, which describes the ratio of higher order terms to the LO predictions.

$$N^k LO_{\text{QCD}}(\boldsymbol{\mu}) = K_{N^kLO}^{(V)}(x, \boldsymbol{\mu}) LO_{\text{QCD}}(\boldsymbol{\mu}_0). \qquad (6.4.1)$$

The dependence on the renormalization and factorization scales, $\boldsymbol{\mu} = (\mu_R, \mu_F)$, is absorbed into the K-factors, while LO predictions on the r.h.s. of Equation (6.4.1) are taken at the central scale, $\boldsymbol{\mu}_0 = (\mu_{R,0}, \mu_{F,0})$. For the central scale we adopt the commonly used choice

$$\mu_{R,0} = \mu_{F,0} = \mu_0 = \hat{H}_T/2, \qquad (6.4.2)$$

where the total transverse energy, $\hat{H}_T$, is defined as the scalar sum of the transverse energy of all parton-level final-state objects,

$$\hat{H}_T = E_{T,V} + \sum_{i \in \{q,g\}} |p_{T,i}|. \qquad (6.4.3)$$

Any quarks and gluons that are radiated in the (N)NLO QCD corrections are included in $\hat{H}_T$, and the vector-boson transverse energy, $E_{T,V}$, is computed using the total (off-shell) four-momentum of the corresponding decay products, *i.e.*

$$E_{T,Z}^2 = p_{T,\ell^+\ell^-}^2 + m_{\ell^+\ell^-}^2, \quad E_{T,W}^2 = p_{T,\ell\nu}^2 + m_{\ell\nu}^2. \qquad (6.4.4)$$

6.5   QCD uncertainties

Both the factorisation and renormalisation scales do not represent a physical scale and as such no physical observable should depend on them. Indeed, when a calculation is performed to all orders any dependence on a scale μ cancels. If the

perturbative series is truncated at a finite order a dependence on μ will manifest. This dependence reflects our lack of knowledge of higher-order terms and should be presented as a theoretical uncertainty. The standard approach to estimate the theory uncertainty due to a specific scale choice is to consider a standard seven-point variations the central scale μ_0, *i.e.*

$$\frac{\boldsymbol{\mu}_i}{\mu_0} = \left\{ (1,1),(2,2),(0.5,0.5),(2,1),(1,2),(1,0.5),(0.5,1) \right\}, \qquad (6.5.1)$$

where $i = 0, \ldots 6$. Nominal predictions and related uncertainties are defined as the centre and the half-width of the band resulting from the above variations. In terms of K-factors this corresponds to

$$K_{N^k LO}^{(V)}(x) = \frac{1}{2} \left[K_{N^k LO}^{(V,max)}(x) + K_{N^k LO}^{(V,min)}(x) \right], \qquad (6.5.2)$$

$$\delta^{(1)} K_{N^k LO}^{(V)}(x) = \frac{1}{2} \left[K_{N^k LO}^{(V,\mathrm{max})}(x) - K_{N^k LO}^{(V,\mathrm{min})}(x) \right], \qquad (6.5.3)$$

with

$$K_{N^k LO}^{(V,max)}(x) = max \left\{ K_{N^k LO}^{(V)}(x, \boldsymbol{\mu}_i) \, | 0 \leq i \leq 6 \right\},$$

$$K_{N^k LO}^{(V,min)}(x) = min \left\{ K_{N^k LO}^{(V)}(x, \boldsymbol{\mu}_i) \, | 0 \leq i \leq 6 \right\}. \qquad (6.5.4)$$

As the K-factors themselves include the scale variations the LO K-factor will differ from unity. These constant scale variations provide an overall change to the normalization and tend not to provide any information on shape uncertainties, which is needed for an accurate extrapolation from low p_T to high p_T. To give a reasonably conservative estimate of the shape uncertainty we introduce an additional shape variation,

$$\delta^{(2)} K_{N^k LO}^{(V)}(x) = \delta^{(1)} K_{N^k LO}^{(V)}(x) \omega(x), \qquad (6.5.5)$$

which is the standard scale uncertainty from Equation (6.5.3) multiplied by a function, $\omega(x)$, which represents a shape distortion. It is defined as,

$$\omega(p_T) = \frac{p_T^2 - p_{T,0}^2}{p_T^2 + p_{T,0}^2}, \qquad (6.5.6)$$

which behaves as $\omega(p_T) \to \pm 1$ for high and low p_T respectively. $p_{T,0}$ is the reference value which is chosen to be $p_{T,0} = 700$ GeV, for $\sqrt{s} = 27$ TeV, and 1.2 TeV for $\sqrt{s} = 100$ TeV. Another key uncertainty is due to the correlation across the $V + jet$ processes which can play an important role in the fits of $Z(\nu\bar{\nu}) + jet$ dark matter backgrounds. In QCD there is little difference between the processes $pp \to W + $ jet and $pp \to Z + $ jet at high $p_T \gg M_{W,Z}$. With this in mind it is expected that the QCD uncertainties will be highly correlated. This means that there will be little dependence on V in the K-factors and the corresponding errors at high p_T. To model the uncertainties due to these correlated processes we take the difference of the known K-factors to the Z K-factors,

$$\delta^{(3)} K^{(V)}_{N^k LO}(x) = \Delta K^{(V)}_{N^k LO}(x) - \Delta K^{(Z)}_{N^k LO}(x), \tag{6.5.7}$$

where $\Delta K^{(V)}$ is taken from the highest known term in the perturbative expansion

$$\Delta K^{(V)}_{N^k LO}(x) = \frac{\Delta K^{(V)}_{N^k LO}(x)}{\Delta K^{(V)}_{N^{k-1} LO}(x)} - 1, \tag{6.5.8}$$

This uncertainty can is calculated using the central scale throughout this chapter. The choice of Z as the reference distribution is arbitrary but changing it results in little or no change in $\delta^{(3)} K^{(V)}_{N^k LO}(x)$ as the overall shift will largely cancel.

6.6   Numerical Results

The nominal distributions for the vector-boson p_T in $W/Z + $ jet production and their ratios at LO, NLO and NNLO are presented for $\sqrt{s} = 27$ TeV and $\sqrt{s} = 100$ TeV in Figures 6.2, 6.3, 6.6 and 6.7. In all plots W refers to the combined W^+ and W^- distributions. In Figure 6.2 the QCD uncertainties from Equations (6.5.3), (6.5.5) and (6.5.7) are combined in quadrature while in Figures 6.3, 6.6 and 6.7 the individual errors are presented.

At both energies we can see that at high p_T the QCD corrections and uncertainties behave in a similar way, which show that the QCD corrections are independent of

Figure 6.2: Higher-order QCD predictions and uncertainties for $Z(\ell^+\ell^-)$ + jet and $W^\pm(\ell\nu)$ + jet production at 27 TeV and 100 TeV. Absolute predictions at LO, NLO and NNLO QCD are displayed in the main frame. The ratio plots show results for individual processes normalised to NLO QCD. The bands correspond to the QCD uncertainties Equations (6.5.3), (6.5.5) and (6.5.7) combined in quadrature.

the vector-boson. In Figure 6.2, the LO uncertainties are of the order 20-30% while the NLO corrections, which amount to a correction of 30-40% compared to the LO, have QCD uncertainties are in the range 10-20%. The NNLO correction is a further increase the cross section by 5-10% with a scale uncertainties 2-10%. Figures 6.3 and 6.4 show that the two largest source of uncertainty in the p_T distribution are the scale variations in Equation (6.5.3) and the uncertainty due to the shape variations in Equation (6.5.5). The contribution from the process-correlation uncertainty in Equation (6.5.7) is the smallest, as expected.

The K-factors in Figures 6.6 and 6.7 are stable at both energies and do not change drastically over the p_T range. In the lower frames we see the individual contributions to the total uncertainty from Equations (6.5.3), (6.5.5) and (6.5.7) divided by $K^{(V)}_{N^kLO}$ so to show the relative contribution. $\delta^{(1)}K^{(V)}_{N^kLO}$ and $\delta^{(2)}K^{(V)}_{N^kLO}$ gradually grow as p_T increase with $\delta^{(2)}K^{(V)}_{N^kLO}$ transitioning from a negative impact to a positive one as the

p_T approaches $p_{T,0}$. $\delta^{(3)}K^{(V)}_{N^kLO}$ provides the smallest contribution to the uncertainty and it remains stable across most of the p_T range. At NNLO the uncertainty on the K-factors is greatly reduced, by a factor ≈ 2, compared to the NLO case. All three $\delta^{(i)}K^{(V)}_{N^kLO}$ maintain the same shape but there magnitudes have all been reduced, in particular the process-correlation uncertainty has nearly vanished.
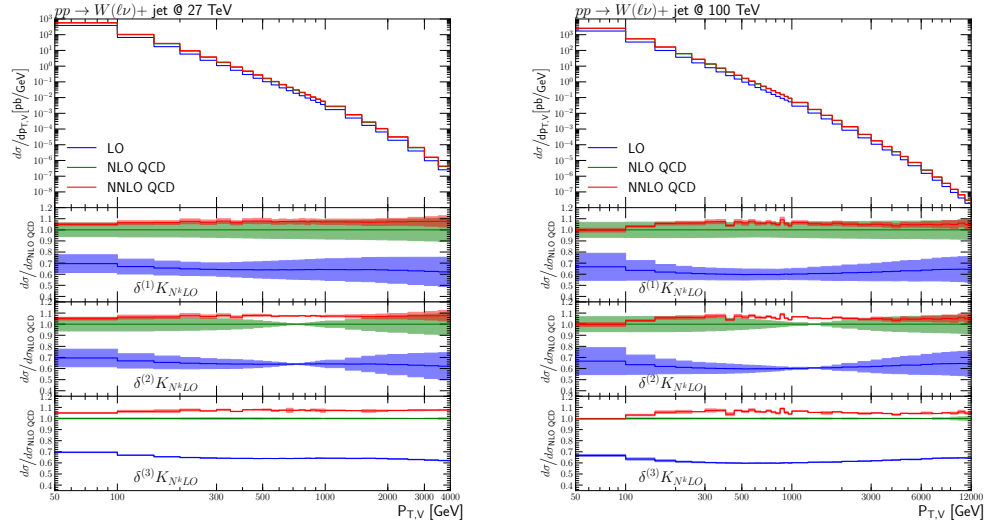
Figure 6.3: Higher-order QCD predictions and uncertainties for $W^{\pm}(\ell\nu)$ + jet production at 27 TeV and 100 TeV. Absolute predictions at LO, NLO and NNLO QCD are displayed in the main frame. The ratio plots show results for individual processes normalised to NLO QCD. The bands correspond to the QCD uncertainties, $\delta^{(i)}K_{N^kLO}$, i.e. scale uncertainties according to Equations (6.5.3), (6.5.5) and (6.5.7).
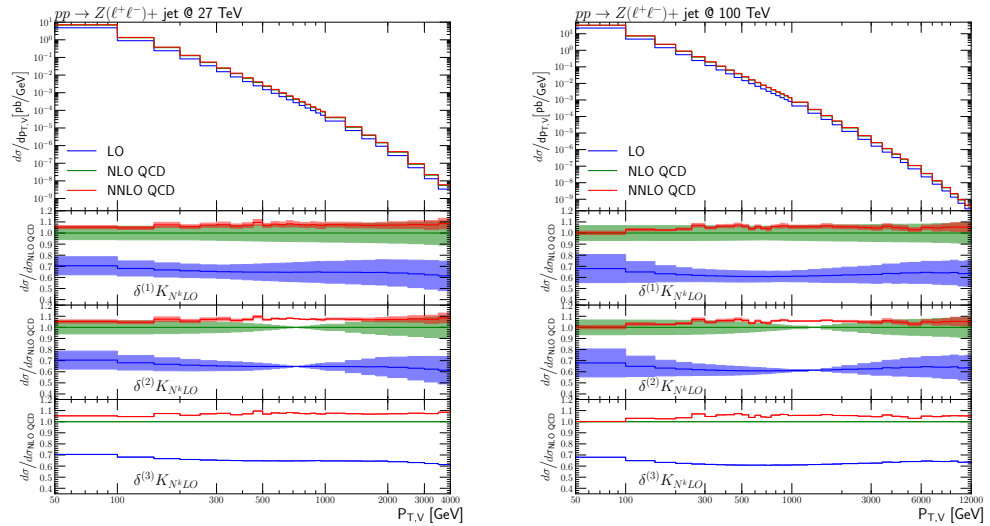
Figure 6.4: Higher-order QCD predictions and uncertainties for $Z(\ell^+\ell^-)$ + jet production at 27 TeV and 100 TeV. Absolute predictions at LO, NLO and NNLO QCD are displayed in the main frame. The ratio plots show results for individual processes normalised to NLO QCD. The bands correspond to the QCD uncertainties, δK_{N^kLO}, i.e. scale uncertainties according to Equations (6.5.3), (6.5.5) and (6.5.7).
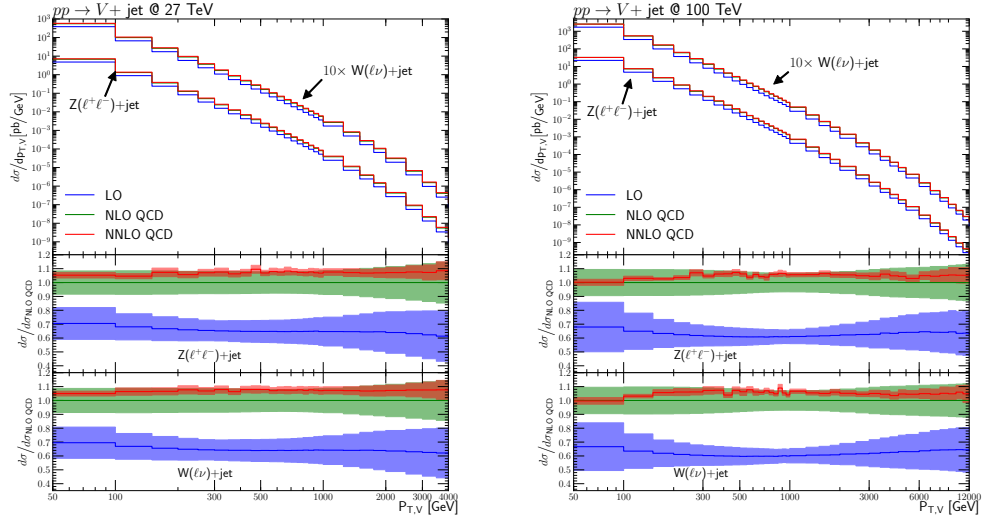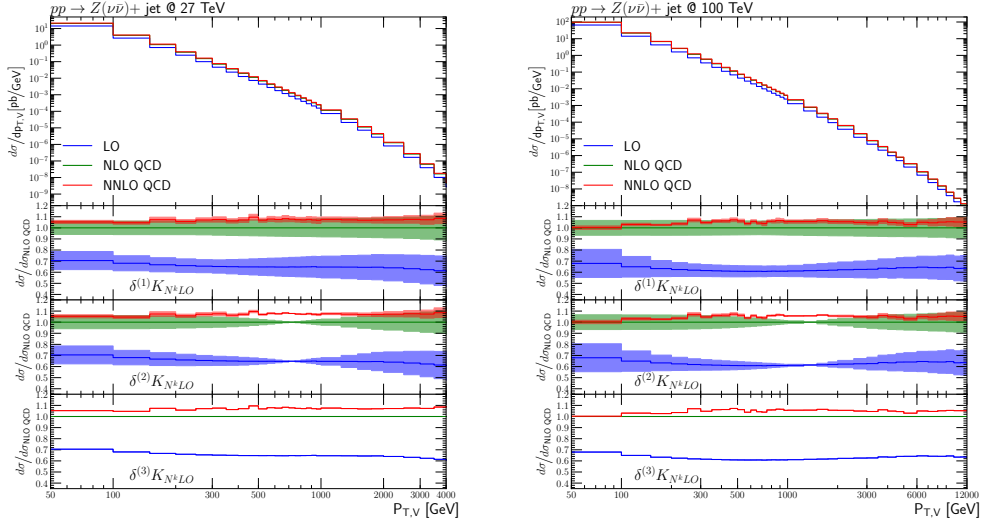
Figure 6.5: Higher-order QCD predictions and uncertainties for $Z(\ell^+\ell^-)$+jet and $W^\pm(\ell\nu)$+jet production at 27 TeV and 100 TeV. Absolute predictions at LO, NLO and NNLO QCD are displayed in the main frame. The ratio plots show results for individual processes normalised to NLO QCD. The bands correspond to the QCD uncertainties, δK_{N^kLO}, i.e. scale uncertainties according to Equations (6.5.3), (6.5.5) and (6.5.7).
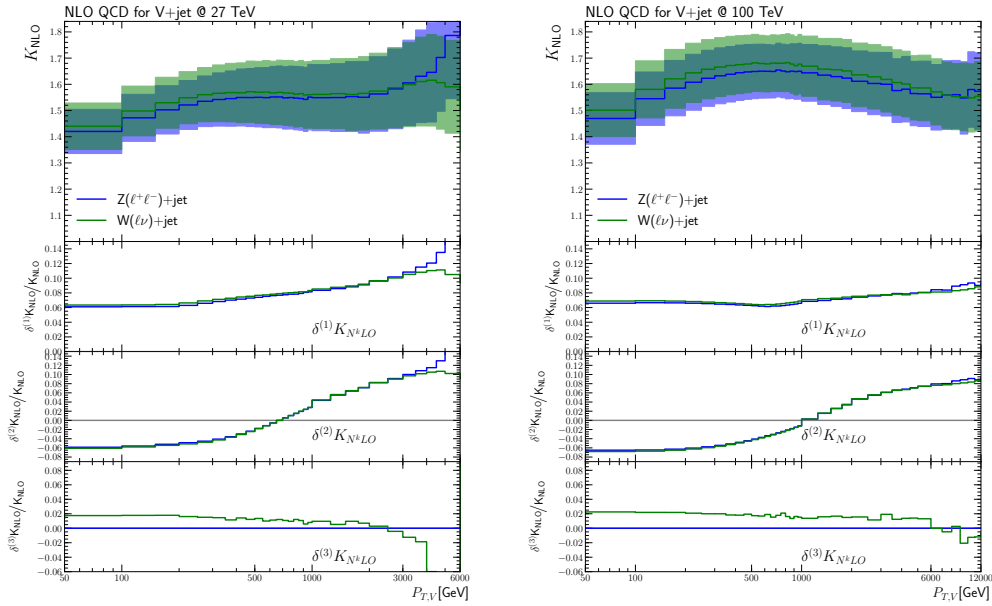
Figure 6.6: Plot of the K-factor for $Z(\ell^+\ell^-)$ + jet and $W^\pm(\ell\nu)$ + jet production at 27 TeV and 100 TeV. The K-factors are taken at NLO with respect to LO are presented in the main frame. The lower frames corresponds to there errors given by Equations (6.5.3), (6.5.5) and (6.5.7) which are divided by K_{NLO}.
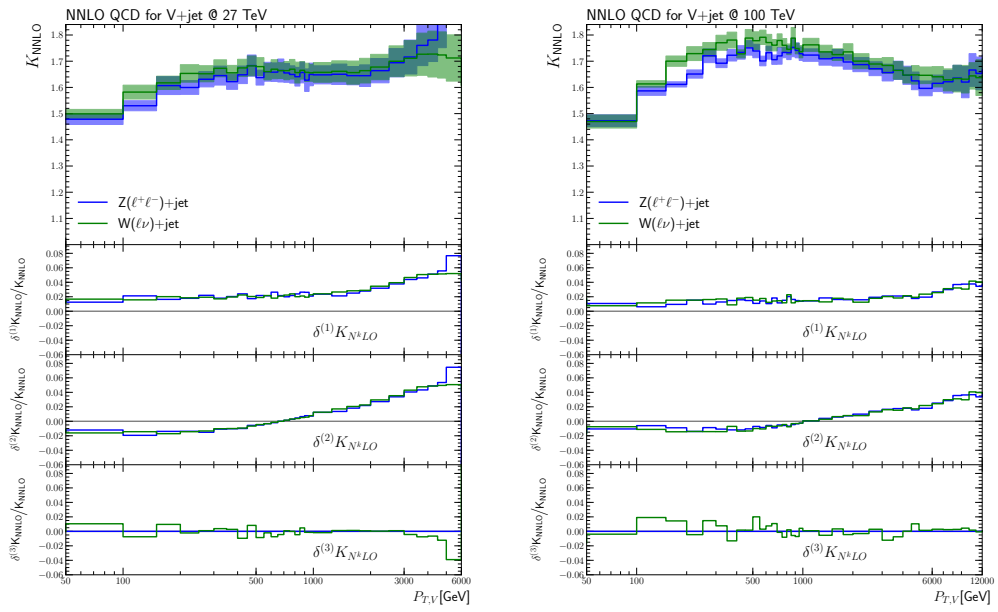
Figure 6.7: Plot of the K-factor for $Z(\ell^+\ell^-) + \mathrm{jet}$ and $W^\pm(\ell\nu) + \mathrm{jet}$ production at 27 TeV and 100 TeV. The K-factors are taken at NNLO with respect to NLO are presented in the main frame. The lower frames corresponds to there errors given by Equations (6.5.3), (6.5.5) and (6.5.7) which are divided by K_{NNLO}.

Chapter 7

Conclusion

The control of the MET background is crucial to maximise the potential of the HL/HE-LHC for BSM searches. These backgrounds can be calculated directly or they can be related to experimental data by calculating similar V+jet processes, in particular $W(\ell\nu)$ + jet and $Z(\ell^+\ell^-)$ + jet which have been the focus of the previous chapter. Another important process that needs to be consider in the future is γ + jet production. When this study was first undertaken the NNLO prediction of this process was under development in NNLOJET. Recently, the calculation has been completed [137] and in the future it should undergo the same analysis that was preformed on W/Z + jet.

We have calculated the inclusive vector-boson p_T distributions for W/Z + jet using the most advanced tools available. The predictions have been produced up to NNLO in QCD and the associated scale uncertainties have been studied in detail. The scale uncertainties, defined in Equation (6.5.3), were chosen so they had a strong correlation across the full p_T range. They were then enhanced with a shape uncertainty in Equation (6.5.5), which was anti-correlated across the p_T. Both of these uncertainties are process-independent while the third uncertainty we introduced is process dependent. It was defined as the difference between K-factors for different process and is given in Equation (6.5.7). The QCD corrections are substantial. For NLO they are in the range of 10-20%, while for NNLO they can range from 2% to as high

as 10%. The scale uncertainties of the NLO and NNLO are consistent with each other, not only in the p_T distribution but also in the K-factors.

While this analysis has shown a detailed understanding of scale and shape uncertainties in $V + \mathrm{jet}$ production it is only the first step towards a complete theoretical treatment. Notably we have not included any $\mathrm{NLO_{EW}}$ corrections and nor have investigated the PDF uncertainties. The $\mathrm{NLO_{EW}}$ are known to contribute significantly at high p_T due to the logarithmic enhancement. The role of PDF uncertainties should be taken into account in a future study. In particular, these uncertainties can be quite significant at high p_T and large x, where the PDFs tend to be less precise.

We have shown that for future colliders it is possible to constrain theoretical errors for the p_T of bosons to the level of a few percent. This level of precision will be a valuable contribution for future MET+jet searches.

Appendix A

Details on YFS Resummation

In this appendix, we will present the MC algorithm used to generate the full phasespace for YFS resummation. In particular, we will present how the photon momenta are generated and distributed according to the YFS eikonals.

A.1 YFS Infrared Functions

In this appendix, we present some analytical representations of the YFS infrared (IR) functions corresponding to the emission of virtual and real photons from a pair of charged massive particles. As already defined in Chapter 3 the YFS-Form-Factor $Y(\Omega)$ reads

$$ Y(\Omega) = 2\alpha \sum_{i<j} \left(\mathcal{R}e \, B(p_i, p_j) + \tilde{B}(p_i, p_j, \Omega) \right) , $$

where the virtual eikonal factor is given by

$$ B(p_i, p_j) \;\; = \;\; -\frac{i}{8\pi^3} Z_i Z_j \theta_i \theta_j \int \frac{\mathrm{d}^4 k}{k^2} \left(\frac{2p_i \theta_i - k}{k^2 - 2(k \cdot p_i)\theta_i} + \frac{2p_j \theta_j + k}{k^2 + 2(k \cdot p_j)\theta_j} \right)^2 , $$

and the real eikonal factor reads

$$ \tilde{B}(p_i, p_j, \Omega) \;\; = \;\; \frac{1}{4\pi^2} Z_i Z_j \theta_i \theta_j \int \mathrm{d}^4 k \, \delta(k^2) \left(1 - \Theta(k, \Omega) \right) \left(\frac{p_i}{(p_i \cdot k)} - \frac{p_j}{(p_j \cdot k)} \right)^2 . $$

Here Z_i and Z_j are the charges of particles i and j in units of the positron charge, respectively, and $\theta_{i,j} = \pm 1$ for final (initial) state particles. Ω is the region of the phase space for which the soft photons cannot be resolved. The divergences present in this expression need to be regularised, which can be achieved by either introducing a fictitious small photon mass m_γ, as in the original YFS paper [39], or through dimensional regularisation.

Virtual IR Function

Here we present the expression for the virtual part of the YFS for any two charged massive particles.

$$
\begin{aligned}
2\alpha \mathcal{R}B(p_1, p_2) \;=\; & -Z_i Z_j \theta_i \theta_j \frac{\alpha}{\pi} \Bigg[\left(\frac{1}{\rho} \ln \frac{\mu(1+\rho)}{m_1 m_2} - 1 \right) \ln \frac{m_\gamma^2}{m_1 m_2} + \frac{\mu\rho}{s} \ln \frac{\mu(1+\rho)}{m_1 m_2} \\
& + \frac{m_1^2 - m_2^2}{2s} \ln \frac{m_1}{m_2} + \frac{1}{\rho} \left(\pi^2 - \frac{1}{2} \ln \frac{\mu(1+\rho)}{m_1^2} \ln \frac{\mu(1+\rho)}{m_2^2} \right. \\
& \left. - \frac{1}{2} \ln^2 \frac{m_1^2 + \mu(1+\rho)}{m_2^2 + \mu(1+\rho)} - \mathrm{Li}_2(\zeta_1) - \mathrm{Li}_2(\zeta_2) \right) - 1 \Bigg],
\end{aligned}
\qquad \text{(A.1.1)}
$$

where,

$$
\begin{aligned}
\mu \;&=\; p_1 p_2, \quad s = 2\mu + m_1^2 + m_2^2, \\
\rho \;&=\; \sqrt{1 - \left(\frac{m_1 m_2}{\mu} \right)^2}, \\
\zeta_i \;&=\; \frac{2\mu\rho}{m_i^2 + \mu(1+\rho)}.
\end{aligned}
\qquad \text{(A.1.2)}
$$

Real IR Function

Here we present an expression for the IR function $\tilde{B}$ which corresponds to the the emission of a real photon $k \in \Omega$ from a dipole consisting of two charged massive particles p_1 and p_2.

$$
\begin{aligned}
2\alpha \tilde{B}(p_1, p_2) \;=\; & -Z_i Z_j \theta_i \theta_j \frac{\alpha}{\pi} \Bigg[\left(\frac{1}{\rho} \ln \frac{\mu(1+\rho)}{m_1 m_2} - 1 \right) \ln \frac{\omega}{m_\gamma^2} + \frac{1}{2\beta_1} \ln \frac{1+\beta_1}{1-\beta_1} \\
& + \frac{1}{2\beta_2} \ln \frac{1+\beta_2}{1-\beta_2} + \mu G\left(p_1, p_2 \right) \Bigg],
\end{aligned}
\qquad \text{(A.1.3)}
$$

where $\beta_i = \frac{|\vec{p}_i|}{E_i}$ and μ, ρ are defined in Appendix A.1 and ω is the momentum cut-off specifying Ω in the frame $\tilde{B}$ is to be evaluated in. $G(p_1, p_2)$ is a complicated function that can be expressed as a combination of logarithms and dilogarithms,

$$
\begin{aligned}
G(p_1, p_2) \; = \; & \frac{1}{\sqrt{(Q^2 + M^2)(Q^2 + \delta^2)}} \left[\ln \frac{\sqrt{\Delta^2 + Q^2} - \Delta}{\Delta^2 + Q^2 + \Delta} \left[\chi_{23}^{14}(\eta_1) - \chi_{23}^{14}(\eta_0) \right] \right. \\
& \left. + Y(\eta_1) - Y(\eta_0) \right],
\end{aligned}
\tag{A.1.4}
$$

where,

$$
\begin{aligned}
\chi_{kl}^{ij} \; = \; & \ln \left| \frac{(\eta - y_i)(\eta - y_j)}{(\eta - y_k)(\eta - y_l)} \right| \\
Y(\eta) \; = \; & Z_{14}(\eta) + Z_{21}(\eta) + Z_{32}(\eta) - Z_{34}(\eta) + \frac{1}{2} \chi_{34}^{12}(\eta) \chi_{14}^{23}(\eta) \\
Z_{ij}(\eta) \; = \; & 2\mathrm{Li}_2 \left(\frac{y_j - y_i}{\eta - y_i} \right) + \frac{1}{2} \ln^2 \left| \frac{\eta - y_i}{\eta - y_j} \right|,
\end{aligned}
\tag{A.1.5}
$$

and

$$
\begin{aligned}
\eta_0 \; = \; & \sqrt{E_2^2 - m_2^2}, \eta_1 = \sqrt{E_1^2 - m_1^2} + \sqrt{\Delta^2 + Q^2} \\
y_{1,2} \; = \; & \frac{1}{2} \left[\sqrt{\Delta^2 + Q^2} - E + \frac{M\delta \pm \sqrt{(Q^2 + M^2)(Q^2 + \delta^2)}}{\sqrt{\Delta^2 + Q^2} + \Delta} \right] \\
y_{3,4} \; = \; & \frac{1}{2} \left[\sqrt{\Delta^2 + Q^2} + E + \frac{M\delta \pm \sqrt{(Q^2 + M^2)(Q^2 + \delta^2)}}{\sqrt{\Delta^2 + Q^2} - \Delta} \right],
\end{aligned}
\tag{A.1.6}
$$

where the following notation has been introduced,

$$
\begin{aligned}
\Delta \; = \; & E_1 - E_2, E = E_1 + E_2, \\
\delta \; = \; & m_1 - m_2, M = m_1 + m_2, \\
Q^2 \; = \; & -(p_1 - p_2)^2.
\end{aligned}
\tag{A.1.7}
$$

A.2   ISR Algorithm

In this section we will derive an algorithm for the emission of multiple soft photons from the initial state of $e^+ e^-$ collisions. We will take the beam momentum p_1 and

p_2 to be in the CMS frame where,

$$p_{1,2} = \left(\frac{\sqrt{s}}{2}, 0, 0, \pm p_z \right) \tag{A.2.1}$$

Neglecting higher-order corrections the, YFS cross section in Equation (3.1.13) is given by,

$$\sigma^{\text{ISR}} = e^{Y(\Omega(\epsilon))} \sum_{n=0}^{\infty} \frac{1}{n!} \int d\hat{s} \, d\sigma_{\text{Born}} \left(\hat{s} \right) \prod_{i=1}^{n} \left[\frac{d^3 k_i}{k_i^0} \tilde{S}(p_1, p_2, k_i) \Theta \left(k_i - E_{\text{min}} \right) \right]$$
$$\times \delta^4 \left(\hat{s} - (P - \sum_j k_j)^2 \right) \tag{A.2.2}$$

Let us introduce a new integration variable,

$$v = 1 - \frac{\hat{s}}{s} = \frac{2KP - K^2}{P^2}, \text{ and } P = p_1 + p_2, \quad K = \sum_{i=1}^{n} k_i. \tag{A.2.3}$$

Here p_i are the initial state momenta before any photon emissions and k_i are the photon momenta. This then transforms Equation (A.2.2), which becomes,

$$\sigma^{\text{ISR}} = e^{Y(\Omega(\epsilon))} \int_{\epsilon}^{v_{max}} dv \, d\sigma_{\text{Born}} \left(s(1 - v) \right)$$
$$\sum_{n=0}^{\infty} \frac{1}{n!} \int \prod_{i=1}^{n} \left[\frac{d^3 k_i}{k_i^0} \tilde{S}(p_1, p_2, k_i) \Theta \left(k_i - E_{\text{min}} \right) \right] \delta^4 \left(v - \frac{2KP - K^2}{P^2} \right) \tag{A.2.4}$$

$\Theta \left(k_i - E_{\text{min}} \right)$ is a cut introduced to ensure that soft singular regions are excluded from the integration region as $\Theta \left(k_i - E_{\text{min}} \right) = \Theta(\frac{2k_i^0}{\sqrt{s}} - \epsilon)$. Any dependence on this infrared cut-off is exactly cancelled by the YFS form factor [39, 138],

$$
\begin{aligned}
e^{Y(\Omega(\epsilon))} &= e^{\frac{-2\alpha}{\pi} Z_i Z_j \alpha \left(\tilde{B}(p_1, p_2, \epsilon) + \mathcal{R}e \left(B(p_1, p_2) \right) \right)} \\
&= e^{\frac{-2\alpha}{\pi} Z_i Z_j \left(\tilde{B}(p_1, p_2) + \int \frac{d^3 k}{k^0} \tilde{S}(k) \left(1 - \theta \left(k^0 - \frac{\epsilon \sqrt{s}}{2} \right) \right) \right)} \\
&= e^{\gamma \ln(\epsilon) + \frac{\gamma}{4} - Z_i Z_j \frac{\alpha}{\pi} (\frac{\pi^2}{3} - \frac{1}{2})}, \tag{A.2.5}
\end{aligned}
$$

where $Z_{i,j}$ are the electric charges of the incoming fermions in units of the electron charge. This expression is taken in the limit $\frac{m_f^2}{s} \ll 1$ while the full expression for a given dipole can be found in Appendix A.1. The relative numerical difference between this approximation and the full calculation was checked and found to be

of the order 10^{-8} [1]. The upper integration limit $v_{\max}$ must satisfy kinematical constraints defined by the final state particles. Introducing a simpler constraint than the one in Equation (A.2.3) we have,

$$\sigma_n^{\text{ISR}}(v) = e^{Y(\Omega(\epsilon))} \int_\epsilon^{v_{max}} dv \, d\sigma_{\text{Born}}(\hat{s}) \int \prod_{i=1}^n \left[\frac{d^3 k_i}{k_i^0} \tilde{S}(k_i) \right]$$
$$\times \delta\Big(v - \frac{2KP - K^2}{P^2}\Big) \prod_{i=1}^{n-1} \theta(k_i^0 - k_{i+1}^0)\theta(k_n^0 - \frac{\sqrt{s}}{2}\epsilon) \qquad (A.2.6)$$

Here, the photon energies have been rearranged at the expense of the symmetry factor and therefore Θ^{cm} is replaced by a single θ function depending on the energy of the softest photon. Introducing a new variable and a delta function which represents this simpler constraint,

$$\sigma_n^{\text{ISR}}(v) = e^{Y(\Omega(\epsilon))} \int_\epsilon^{v_{max}} dv \, \sigma_{\text{Born}}(\hat{s}) \int d\lambda \prod_{i=1}^n \frac{d^3 k_i}{k_i^0} \tilde{S}(k_i)\delta\Big(\lambda - \frac{2k_1 P}{vP^2}\Big)$$
$$\times \delta\Big(v - \frac{2KP - K^2}{P^2}\Big) \prod_{i=1}^{n-1} \theta(k_i^0 - k_{i+1}^0)\theta(k_n^0 - \frac{\sqrt{s}}{2}\epsilon) \qquad (A.2.7)$$

Now all photon momenta are rescaled, $k = \lambda\bar{k}$, and the old $\delta-$function can be removed by integrating over λ.

$$\sigma_n^{\text{ISR}}(v) = e^{Y(\Omega(\epsilon))} \int_\epsilon^{v_{max}} dv \, \sigma_{\text{Born}}(\hat{s}) \int d\lambda \prod_{i=1}^n \frac{\lambda^3 d^3 \bar{k}_i}{\lambda\bar{k}_i^0}\frac{1}{\lambda^2} \tilde{S}(\bar{k}_i)\delta\Big(\lambda - \frac{\lambda 2\bar{k}_1 P)}{vP^2}\Big)$$
$$\times \delta\Big(v - \frac{\lambda 2\bar{K}P - \lambda^2 \bar{K}^2}{P^2}\Big) \prod_{i=1}^{n-1} \theta(\lambda\bar{k}_i^0 - \lambda\bar{k}_{i+1}^0)\theta(\lambda\bar{k}_n^0 - \frac{\sqrt{s}}{2}\epsilon) \qquad (A.2.8)$$

After removing the old $\delta-$function the resulting integral is given by,

$$\sigma^{\text{ISR}}(v) = e^{Y(\Omega(\epsilon))} \int_\epsilon^{v_{max}} dv \, \sigma_{\text{Born}}(\hat{s}) \int \prod_{i=1}^n \frac{d^3 \bar{k}_i}{\bar{k}_i^0}\delta\Big(\frac{2\bar{k}_1^0}{\sqrt{s}} - v\Big)$$
$$\times \theta(\bar{k}_1^0 - \bar{k}_2^0)\theta(\bar{k}_2^0 - \bar{k}_3^0)\cdots\theta(\bar{k}_{n-1}^0 - \bar{k}_n^0)\theta(\lambda_0\bar{k}_n^0 - \frac{\sqrt{s}}{2}\epsilon)$$
$$\times \mathcal{J}(\bar{K}, v) \qquad (A.2.9)$$

This gives us a new constraint on the most energetic photon, $\bar{k}_1^0 = v\frac{\sqrt{s}}{2}$. $\mathcal{J}$ and

---

[1]The user may chose to use the full calculation by setting "YFS_FULL_FORM: true" in the runcard

λ_0 are algebraic functions resulting from removing the old delta function and are defined as,

$$
\mathcal{J}(\bar{K}, v) = \frac{1}{2}\left(1 + \frac{1}{\sqrt{1 - Av}}\right), \quad A = \frac{\bar{K}^2 P^2}{(\bar{K} P)^2}, \quad \bar{K} = \sum_{i=1}^{n} k_i \quad \text{(A.2.10)}
$$

$$
\lambda_0 = v\frac{P^2}{\bar{K} P}\frac{1}{1 + \sqrt{1 - Av}}, \quad\quad\quad\quad\quad\quad\quad\quad \text{(A.2.11)}
$$

where $A \leq 1$ and $0 \leq \lambda_0 \leq 1$. It is worth noting that if there is only one photon or if the invariant mass of the photon system is 0 then both the old and the new constraints are the same and therefore there is no need to introduce a rescaling. For these case, the Jacobian disappears and $\lambda_0 \to 1$.

The next step in the algorithm is to introduce an explicit form for the photon momentum. A natural choice is to parametrise the momentum using polar coordinates.

$$
k_i = \lambda_0 \bar{k}_i = \lambda_0 \frac{\sqrt{s}}{2} x_i (1, \sin\theta_i \cos\phi_i, \sin\theta_i \sin\phi_i, \cos\theta_i). \quad \text{(A.2.12)}
$$

In this parametrisation the eikonal term is given by,

$$
\frac{d^3 k_i}{k_i^0}\tilde{S}(k_i) = \frac{d^3 \bar{k}_i}{\bar{k}_i^0}\tilde{S}(\bar{k}_i) = \frac{dx_i}{x_i}\,d(\cos\theta_i)\,d\phi_i\,g(\theta_i), \quad \text{(A.2.13)}
$$

and $g(\theta)$ is given by,

$$
g(\theta) = \frac{\alpha}{\pi^2}\left(\frac{2(1 + \beta_1\beta_2)}{(1 - \beta_1\cos\theta)(1 + \beta_2\cos\theta)} - \frac{1 - \beta_1^2}{(1 - \beta_1\cos\theta)^2} - \frac{1 - \beta_2^2}{(1 + \beta_2\cos\theta)^2}\right),
$$
$$
\text{(A.2.14)}
$$

where $\beta_i = \frac{|\vec{p}_i|}{p_i^0}$. Inserting this into Equation (3.2.1) we arrive at a new expression for the total cross-section

$$
\sigma^{\text{ISR}} = e^{Y(\Omega(\epsilon))}\int_\epsilon^{v_{\text{max}}} dv\,\sigma_{\text{Born}}\left(s\left(1 - v\right)\right)[\delta(v) +
$$
$$
\sum_{n=1}^{\infty}\prod_{i=1}^{n}\int_\epsilon^v \frac{dx_i}{x_i}\int_{-1}^{1}d(\cos\theta_i)\int_0^{2\pi}d\phi_i\,g\left(\theta_i\right)
$$
$$
\times\delta(v - x_1)\theta(x_1 - x_2)\cdots\theta(x_{n-1} - x_n)\theta(\lambda_0 x_n - \epsilon)\mathcal{J}(\bar{K}, v)\Big], \quad \text{(A.2.15)}
$$

The transition from Equation (3.2.1) to Equation (A.2.15) involved no approximations or simplifications and the two equations are exactly equal to each other, the

latter merely has had its phasespace reorganised. It is now nearly possible to generate Equation (A.2.15) from uniform random numbers. However, this is complicated by the presence of the term $\theta(\lambda_0(\bar{K}, v)x_n - \epsilon)$. This factor corresponds to the IR cut-off of the photon energy and therefore it is problematic to generate photon momenta satisfying this condition as it depends on their sum. Similarly, the dependence of the Jacobian on the photon momentum also provides a complication and will have to be simplified. These simplifications will be corrected for later on in the algorithm. To avoid the problem we simply set λ_0 and A to 1.

$$\theta(\lambda_0(\bar{K}, v)x_n - \epsilon) \to \theta(x_n - \epsilon), \quad \mathcal{J} \to \mathcal{J}_0(v) = \frac{1}{2}(1 + \frac{1}{\sqrt{1-v}}), \qquad \text{(A.2.16)}$$

and correct for this through suitable weights at the end. For numerical stability it is also necessary to correct Equation (A.2.14) by dropping the mass terms.

$$g(\theta) \to \tilde{g}(\theta) = \left(\frac{2(1 + \beta_1 \beta_2)}{(1 - \beta_1 \cos\theta)(1 + \beta_2 \cos\theta)} \right). \qquad \text{(A.2.17)}$$

These simplifications reduce Equation (A.2.15), which is an exact equation, to a new simplified distribution that can be generated from uniform random numbers. With a final change of variable $y_i = \ln x_i$,

$$\begin{aligned}
\sigma_{\text{simple}}^{\text{ISR}} = e^{Y(\Omega(\epsilon))} \int_0^{v_{\max}} & dv\, d\sigma_{\text{Born}}(s(1-v))\, \mathcal{J}_0(v) \\
\times\ & \left(\delta(v) + \frac{1}{v} \sum_{n=1}^{\infty} \prod_{i=1}^{n} \left[\int_{\ln\epsilon}^{\ln v} dy_i \int_{-1}^{1} d(\cos\theta_i)\, \tilde{g}(\theta_i) \int_0^{2\pi} d\phi_i \right] \right. \\
\times\ & \left. \delta(\ln(v) - y_1)\theta(y_1 - y_2)\,\theta(y_2 - y_3) \cdots \theta(y_n - \ln(\epsilon)) \right).
\end{aligned} \qquad \text{(A.2.18)}$$

The integrals over the angles and y_i can be done analytically yielding,

$$\begin{aligned}
\sigma_{\text{simple}}^{\text{ISR}} =\ & e^{Y(\Omega(\epsilon))} \int_0^{v_{\max}} dv\, d\sigma_{\text{Born}}(s(1-v))\, \mathcal{J}_0(v) \Bigg\{ \delta(v) + \\
& + \theta(v - \epsilon)\frac{1}{v}\sum_{n=1}^{\infty} \frac{1}{(n-1)!} \left[\ln\left(\frac{v}{\epsilon}\right) \frac{2\alpha}{\pi} \frac{1 + \beta_1\beta_2}{\beta_1 + \beta_2} \ln \frac{(1 + \beta_1)(1 + \beta_2)}{(1 - \beta_1)(1 - \beta_2)} \right]^{n-1} \Bigg\}.
\end{aligned} \qquad \text{(A.2.19)}$$

Summing over all photons and removing a factor $e^{\gamma \ln(\epsilon)} = \epsilon^{\gamma} = \int_0^{\epsilon} dv\, \gamma v^{\gamma-1}$ from

$e^{Y(\Omega(\epsilon))}$ we have our master formula,

$$\sigma_{\text{simple}}^{\text{ISR}} = e^{\frac{\gamma}{4} + Z_i Z_j \frac{\alpha}{\pi}\left(\frac{\pi^2}{3} - \frac{1}{2}\right)} \left[\int_0^{\epsilon} dv\, \gamma v^{\gamma - 1}\, d\sigma_{\text{Born}}\left(s\right) \right.$$

$$\left. + \int_{\epsilon}^{v_{\max}} dv\, d\sigma_{\text{Born}}\left(s(1 - v)\right) \mathcal{J}_0(v) \bar{\gamma} v^{\bar{\gamma} - 1} \epsilon^{\gamma - \bar{\gamma}} \right]. \tag{A.2.20}$$

where,

$$
\begin{aligned}
\gamma &= \frac{2\alpha}{\pi} \left[\frac{1 + \beta_1 \beta_2}{\beta_1 + \beta_2} \ln \frac{\left(1 + \beta_1\right)\left(1 + \beta_2\right)}{\left(1 - \beta_1\right)\left(1 - \beta_2\right)} - 2 \right], \\
\bar{\gamma} &= \frac{2\alpha}{\pi} \frac{1 + \beta_1 \beta_2}{\beta_1 + \beta_2} \ln \frac{\left(1 + \beta_1\right)\left(1 + \beta_2\right)}{\left(1 - \beta_1\right)\left(1 - \beta_2\right)}.
\end{aligned}
\tag{A.2.21}
$$

This cross-section is now ready to be calculated at the Monte Carlo level.

A.3   Photon Generation

In this section we shall discuss the explicit construction of the photon momentum in the Monte Carlo. As mention in Appendix A.2 the photon momentum are describe using polar coordinates.

Photon Angles

There are two angles used in the parametrisation of the photon momentum that have to be generated. The first, ϕ, is trivial and is given by,

$$\phi = 2\pi \#, \tag{A.3.1}$$

where $\#$ is uniformly generated random number $\in (0, 1)$. The remaining angle θ is slightly more complex. It is generated by sampling from the $\tilde{S}\left(k\right)$distribution,

$$
\begin{aligned}
\tilde{S}\left(k\right) &\propto \left(\frac{p_1}{p_1 k} - \frac{p_2}{p_2 k} \right)^2, \\
&= \left(\frac{p_1^2}{\left(p_1 k\right)^2} + \frac{p_2^2}{\left(p_2 k\right)^2} - \frac{2 p_1 p_2}{\left(p_1 k\right)\left(p_2 k\right)} \right).
\end{aligned}
\tag{A.3.2}
$$

By taking p_1 and p_2 to be the beam momenta, i.e $p_{1/2} = \left(\frac{\sqrt{s}}{2}, 0, 0, \pm p_z \right)$, the eikonal can be written as

$$\tilde{S}(k) \propto \left(\frac{1 - \beta_1^2}{(1 - \beta_1 \cos \theta)^2} + \frac{1 - \beta_2^2}{(1 - \beta_2 \cos \theta)^2} - \frac{2(1 + \beta_1 \beta_2)}{(1 - \beta_1 \cos \theta)(1 + \beta_2 \cos \theta)} \right), \text{(A.3.3)}$$

where $\beta_i = \frac{|\vec{p_i}|}{p_i^0}$. The interference term can be rewritten as,

$$\frac{1}{(1 - \beta_1 \cos(\theta_i))(1 + \beta_2 \cos(\theta_i))} = \frac{\beta_1 \beta_2}{\beta_1 + \beta_2} \left(\frac{1}{\beta_2(1 - \beta_1 \cos(\theta_i))} + \frac{1}{\beta_1(1 + \beta_2 \cos(\theta_i))} \right).$$
$$\text{(A.3.4)}$$

Then $\cos(\theta_i)$ can be generated according to either of the two terms in the interference. For example it can be generated according to $\left(1 - \beta_1 \cos(\theta_i)\right)^{-1}$

$$\int_{-1}^{y} d \cos(\theta_i) \frac{1}{1 - \beta_1 \cos(\theta_i)} = \# \int_{-1}^{1} d \cos(\theta_i) \frac{1}{1 - \beta_1 \cos(\theta_i)},$$

$$\ln \left(\frac{1 + \beta_1}{1 - \beta_1 y} \right) = \# \left(\ln \left(\frac{1 + \beta_1}{1 - \beta_1} \right) \right),$$

$$\cos(\theta_i) = \frac{1}{\beta_1} \left(1 - (1 + \beta_1) \left(\frac{1 - \beta_1}{1 + \beta_1} \right)^{\#} \right). \quad \text{(A.3.5)}$$

The probability associated with this distribution is given by,

$$P_i = \frac{\ln \left(\frac{1 + \beta_1}{1 - \beta_1} \right)}{\ln \left(\frac{1 + \beta_1}{1 - \beta_1} \right) + \ln \left(\frac{1 + \beta_2}{1 - \beta_2} \right)} \quad \text{(A.3.6)}$$

Then $\cos(\theta_i)$ can be the generated according to $\left(1 + \beta_1 \cos(\theta_i)\right)^{-1}$ with a probability of $P_j = 1 - P_i$,

$$\cos(\theta_i) = \frac{1}{\beta_1} \left(1 - (1 - \beta_1) \left(\frac{1 + \beta_1}{1 - \beta_1} \right) \right). \quad \text{(A.3.7)}$$

The correction weight for this distribution is given by,

$$W = \frac{\frac{2(1 + \beta_1 \beta_2)}{(1 - \beta_1 \cos \theta)(1 + \beta_2 \cos \theta)} - \frac{1 - \beta_1^2}{(1 - \beta_1 \cos \theta)^2} - \frac{1 - \beta_2^2}{(1 - \beta_2 \cos \theta)^2}}{\frac{2(1 + \beta_1 \beta_2)}{(1 - \beta_1 \cos(\theta_i))(1 + \beta_2 \cos(\theta_i))}}. \quad \text{(A.3.8)}$$

Bibliography

[1] G. Aad et al., ATLAS Collaboration collaboration, *Observation of a new particle in the search for the Standard Model Higgs boson with the ATLAS detector at the LHC*, `arXiv:1207.7214` [hep-ex].

[2] S. Chatrchyan et al., CMS Collaboration collaboration, *Observation of a new boson at a mass of 125 GeV with the CMS experiment at the LHC*, Phys.Lett. **B716** (2012), 30–61, [`arXiv:1207.7235` [hep-ex]].

[3] G. Aad et al., ATLAS, CMS collaboration, *Combined Measurement of the Higgs Boson Mass in pp Collisions at $\sqrt{s} = 7$ and 8 TeV with the ATLAS and CMS Experiments*, Phys. Rev. Lett. **114** (2015), 191803, [`arXiv:1503.07589` [hep-ex]].

[4] G. Aad et al., ATLAS collaboration, *Measurements of Higgs boson production and couplings in the four-lepton channel in pp collisions at center-of-mass energies of 7 and 8 TeV with the ATLAS detector*, Phys. Rev. D **91** (2015), no. 1, 012006, [`arXiv:1408.5191` [hep-ex]].

[5] S. Chatrchyan et al., CMS collaboration, *Measurement of the Properties of a Higgs Boson in the Four-Lepton Final State*, Phys. Rev. D **89** (2014), no. 9, 092007, [`arXiv:1312.5353` [hep-ex]].

[6] G. Aad et al., ATLAS collaboration, *Observation and measurement of Higgs boson decays to WW^* with the ATLAS detector*, Phys. Rev. D **92** (2015), no. 1, 012006, [`arXiv:1412.2641` [hep-ex]].

[7] G. Aad et al., ATLAS collaboration, *Study of (W/Z)H production and Higgs boson couplings using $H \to WW^*$ decays with the ATLAS detector*, JHEP **08** (2015), 137, [`arXiv:1506.06641` [hep-ex]].

[8] S. Chatrchyan et al., CMS collaboration, *Measurement of Higgs Boson Production and Properties in the WW Decay Channel with Leptonic Final States*, JHEP **01** (2014), 096, [`arXiv:1312.1129` [hep-ex]].

[9] G. Aad et al., ATLAS collaboration, *Search for $H \to \gamma\gamma$ produced in association with top quarks and constraints on the Yukawa coupling between the top quark and the Higgs boson using data taken at 7 TeV and 8 TeV with the ATLAS detector*, Phys. Lett. B **740** (2015), 222–242, [`arXiv:1409.3122` [hep-ex]].

[10] G. Aad et al., ATLAS collaboration, *Search for the Standard Model Higgs boson produced in association with top quarks and decaying into $b\bar{b}$ in pp collisions at $\sqrt{s}$ = 8 TeV with the ATLAS detector*, Eur. Phys. J. C **75** (2015), no. 7, 349, [`arXiv:1503.05066` [hep-ex]].

[11] G. Aad et al., ATLAS collaboration, *Search for the associated production of the Higgs boson with a top quark pair in multilepton final states with the ATLAS detector*, Phys. Lett. B **749** (2015), 519–541, [`arXiv:1506.05988` [hep-ex]].

[12] V. Khachatryan et al., CMS collaboration, *Search for the associated production of the Higgs boson with a top-quark pair*, JHEP **09** (2014), 087, [`arXiv:1408.1682` [hep-ex]], [Erratum: JHEP 10, 106 (2014)].

[13] G. Aad et al., ATLAS collaboration, *Search for the $b\bar{b}$ decay of the Standard Model Higgs boson in associated (W/Z)H production with the ATLAS detector*, JHEP **01** (2015), 069, [`arXiv:1409.6212` [hep-ex]].

[14] S. Chatrchyan et al., CMS collaboration, *Search for the Standard Model Higgs Boson Produced in Association with a W or a Z Boson and Decaying to Bottom Quarks*, Phys. Rev. D **89** (2014), no. 1, 012003, [`arXiv:1310.3687` [hep-ex]].

[15] G. Aad et al., ATLAS collaboration, *Evidence for the Higgs-boson Yukawa coupling to tau leptons with the ATLAS detector*, JHEP **04** (2015), 117, [arXiv:1501.04943 [hep-ex]].

[16] S. Chatrchyan et al., CMS collaboration, *Evidence for the 125 GeV Higgs boson decaying to a pair of τ leptons*, JHEP **05** (2014), 104, [arXiv:1401.5041 [hep-ex]].

[17] G. Aad et al., ATLAS collaboration, *A search for the dimuon decay of the Standard Model Higgs boson with the ATLAS detector*, arXiv:2007.07830 [hep-ex].

[18] A. M. Sirunyan et al., CMS collaboration, *Evidence for Higgs boson decay to a pair of muons*, arXiv:2009.04363 [hep-ex].

[19] J. de Blas et al., *Higgs Boson Studies at Future Particle Colliders*, JHEP **01** (2020), 139, [arXiv:1905.03764 [hep-ph]].

[20] A. Freitas et al., *Theoretical uncertainties for electroweak and Higgs-boson precision measurements at FCC-ee*, arXiv:1906.05379 [hep-ph].

[21] A. Abada et al., FCC collaboration, *FCC-ee: The Lepton Collider: Future Circular Collider Conceptual Design Report Volume 2*, Eur. Phys. J. ST **228** (2019), no. 2, 261–623.

[22] M. Koratzinos, FCC-ee study collaboration, *FCC-ee accelerator parameters, performance and limitations*, Nucl. Part. Phys. Proc. **273-275** (2016), 2326–2328, [arXiv:1411.2819 [physics.acc-ph]].

[23] M. Dong et al., CEPC Study Group collaboration, *CEPC Conceptual Design Report: Volume 2 - Physics & Detector*, arXiv:1811.10545 [hep-ex].

[24] CEPC Study Group collaboration, *CEPC Conceptual Design Report: Volume 1 - Accelerator*, arXiv:1809.00285 [physics.acc-ph].

[25] *A Multi-TeV Linear Collider Based on CLIC Technology: CLIC Conceptual Design Report.*

[26] *Physics and Detectors at CLIC: CLIC Conceptual Design Report,* `arXiv:1202.5940` [physics.ins-det].

[27] P. Lebrun, L. Linssen, A. Lucaci-Timoce, D. Schulte, F. Simon, S. Stapnes, N. Toge, H. Weerts and J. Wells, *The CLIC Programme: Towards a Staged e+e- Linear Collider Exploring the Terascale : CLIC Conceptual Design Report,* `arXiv:1209.2543` [physics.ins-det].

[28] G. Aarons et al., ILC collaboration, *International Linear Collider Reference Design Report Volume 2: Physics at the ILC,* `arXiv:0709.1893` [hep-ph].

[29] G. Aarons et al., ILC collaboration, *ILC Reference Design Report Volume 1 - Executive Summary,* `arXiv:0712.1950` [physics.acc-ph].

[30] G. Aarons et al., ILC collaboration, *ILC Reference Design Report Volume 4 - Detectors,* `arXiv:0712.2356` [physics.ins-det].

[31] *The International Linear Collider Technical Design Report - Volume 3.II: Accelerator Baseline Design,* `arXiv:1306.6328` [physics.acc-ph].

[32] S. Schael et al., ALEPH, DELPHI, L3, OPAL, SLD, LEP Electroweak Working Group, SLD Electroweak Group, SLD Heavy Flavour Group collaboration, *Precision electroweak measurements on the Z resonance,* Phys. Rept. **427** (2006), 257–454, [`hep-ex/0509008`].

[33] D. Abbaneo et al., ALEPH, DELPHI, L3, OPAL, LEP Electroweak Working Group, SLD Heavy Flavor, Electroweak Groups collaboration, *A Combination of preliminary electroweak measurements and constraints on the standard model,* `hep-ex/0112021`.

[34] G. Abbiendi et al., OPAL collaboration, *Photonic events with missing energy in e+ e- collisions at S**(1/2) = 189-GeV*, Eur. Phys. J. C **18** (2000), 253–272, [hep-ex/0005002].

[35] S. Schael et al., ALEPH, DELPHI, L3, OPAL, LEP Electroweak collaboration, *Electroweak Measurements in Electron-Positron Collisions at W-Boson-Pair Energies at LEP*, Phys. Rept. **532** (2013), 119–244, [arXiv:1302.3415 [hep-ex]].

[36] A. Abada et al., FCC collaboration, *FCC Physics Opportunities: Future Circular Collider Conceptual Design Report Volume 1*, Eur. Phys. J. C **79** (2019), no. 6, 474.

[37] S. Jadach and M. Skrzypek, *QED challenges at FCC-ee precision measurements*, Eur. Phys. J. C **79** (2019), no. 9, 756, [arXiv:1903.09895 [hep-ph]].

[38] S. Jadach and M. Skrzypek, *Theory challenges at future lepton colliders*, Acta Phys. Polon. B **50** (2019), 1705, [arXiv:1911.09202 [hep-ph]].

[39] D. R. Yennie, S. C. Frautschi and H. Suura, *The Infrared Divergence Phenomena and High-Energy Processes*, Ann. Phys. **13** (1961), 379–452.

[40] E. Kuraev and V. S. Fadin, *On Radiative Corrections to e+ e- Single Photon Annihilation at High-Energy*, Sov. J. Nucl. Phys. **41** (1985), 466–472.

[41] G. Altarelli and G. Parisi, *Asymptotic freedom in parton language*, Nucl. Phys. **B126** (1977), 298–318.

[42] V. N. Gribov and L. N. Lipatov, *Deep inelastic e-p scattering in perturbation theory*, Sov. J. Nucl. Phys. **15** (1972), 438–450.

[43] L. N. Lipatov, *The parton model and perturbation theory*, Sov. J. Nucl. Phys. **20** (1975), 94–102.

[44] Y. L. Dokshitzer, *Calculation of the structure functions for deep inelastic scattering and e^+e^- annihilation by perturbation theory in quantum chromodynamics*, Sov. Phys. JETP **46** (1977), 641–653.

[45] M. Cacciari, A. Deandrea, G. Montagna and O. Nicrosini, *QED structure functions: A Systematic approach*, Europhys. Lett. **17** (1992), 123–128.

[46] M. Skrzypek, *Leading logarithmic calculations of QED corrections at LEP*, Acta Phys. Polon. B **23** (1992), 135–172.

[47] M. Skrzypek and S. Jadach, *Exact and approximate solutions for the electron nonsinglet structure function in QED*, Z. Phys. C **49** (1991), 577–584.

[48] V. Bertone, M. Cacciari, S. Frixione and G. Stagnitto, *The partonic structure of the electron at the next-to-leading logarithmic accuracy in QED*, JHEP **03** (2020), 135, [`arXiv:1911.12040` [hep-ph]].

[49] S. Frixione, *Initial conditions for electron and photon structure and fragmentation functions*, JHEP **11** (2019), 158, [`arXiv:1909.03886` [hep-ph]].

[50] S. Jadach, B. F. L. Ward and Z. Wąs, *The precision Monte Carlo event generator $\mathcal{KK}$ for two- fermion final states in e^+e^- collisions*, Comput. Phys. Commun. **130** (2000), 260–325, [`hep-ph/9912214`].

[51] A. Buckley et al., *General-purpose event generators for LHC physics*, Phys. Rept. **504** (2011), 145–233, [`arXiv:1101.2599` [hep-ph]].

[52] J. Bellm et al., *Herwig 7.0/Herwig++ 3.0 release note*, Eur. Phys. J. **C76** (2016), no. 4, 196, [`arXiv:1512.01178` [hep-ph]].

[53] S. Gieseke, A. Ribon, M. H. Seymour, P. Stephens and B. Webber, *Herwig++ 1.0: An Event generator for e+ e- annihilation*, JHEP **02** (2004), 005, [`arXiv:hep-ph/0311208` [hep-ph]].

[54] T. Sjöstrand, L. Lönnblad, S. Mrenna and P. Skands, *PYTHIA 6.3 Physics and Manual*, `hep-ph/0308153`.

[55] T. Sjöstrand, S. Mrenna and P. Skands, *PYTHIA 6.4 physics and manual*, JHEP **05** (2006), 026, [`hep-ph/0603175`].

[56] F. Krauss, R. Kuhn and G. Soff, *AMEGIC++ 1.0: A Matrix Element Generator In C++*, JHEP **02** (2002), 044, [`hep-ph/0109036`].

[57] T. Gleisberg and S. Höche, *Comix, a new matrix element generator*, JHEP **12** (2008), 039, [`arXiv:0808.3674` [hep-ph]].

[58] F. Coradeschi, D. de Florian, L. J. Dixon, N. Fidanza, S. Höche, H. Ita, Y. Li and J. Mazzitelli, *Interference effects in the $H(\to \gamma\gamma) + 2$ jets channel at the LHC*, Phys. Rev. **D92** (2015), no. 1, 013004, [`arXiv:1504.05215` [hep-ph]].

[59] T. Gleisberg, F. Krauss, K. T. Matchev, A. Schälicke, S. Schumann and G. Soff, *Helicity formalism for spin-2 particles*, JHEP **09** (2003), 001, [`hep-ph/0306182`].

[60] F. A. Berends and W. Giele, *Multiple Soft Gluon Radiation in Parton Processes*, Nucl.Phys. **B313** (1989), 595.

[61] F. A. Berends and W. Giele, *The six-gluon process as an example of Weyl-van der Waerden spinor calculus*, Nucl. Phys. **B294** (1987), 700.

[62] F. Dyson, *The S matrix in quantum electrodynamics*, Phys.Rev. **75** (1949), 1736–1755.

[63] J. S. Schwinger, *On the Green's functions of quantized fields. 1.*, Proc.Nat.Acad.Sci. **37** (1951), 452–455.

[64] J. S. Schwinger, *On the Green's functions of quantized fields. 2.*, Proc.Nat.Acad.Sci. **37** (1951), 455–459.

[65] N. D. Christensen and C. Duhr, *FeynRules - Feynman rules made easy*, Comput. Phys. Commun. **180** (2009), 1614–1641, [`arXiv:0806.4194` [hep-ph]].

[66] A. Alloul, N. D. Christensen, C. Degrande, C. Duhr and B. Fuks, *FeynRules 2.0 - A complete toolbox for tree-level phenomenology*, Comput.Phys.Commun. **185** (2014), 2250–2300, [`arXiv:1310.1921` [hep-ph]].

[67] R. Kleiss and R. Pittau, *Weight optimization in multichannel Monte Carlo*, Comput. Phys. Commun. **83** (1994), 141–146, [`arXiv:hep-ph/9405257` [hep-ph]].

[68] S. Catani and M. H. Seymour, *A general algorithm for calculating jet cross sections in NLO QCD*, Nucl. Phys. **B485** (1997), 291–419, [`hep-ph/9605323`].

[69] T. Gleisberg and F. Krauss, *Automating dipole subtraction for QCD NLO calculations*, Eur. Phys. J. **C53** (2008), 501–523, [`arXiv:0709.2881` [hep-ph]].

[70] C. F. Berger, Z. Bern, L. J. Dixon, F. Febres-Cordero, D. Forde, H. Ita, D. A. Kosower and D. Maître, *Automated implementation of on-shell methods for one-loop amplitudes*, Phys. Rev. **D78** (2008), 036003, [`arXiv:0803.4180` [hep-ph]].

[71] C. F. Berger, Z. Bern, L. J. Dixon, F. Febres-Cordero, D. Forde, T. Gleisberg, H. Ita, D. A. Kosower and D. Maître, *Next-to-leading order QCD predictions for W+3-Jet distributions at hadron colliders*, Phys. Rev. **D80** (2009), 074036, [`arXiv:0907.1984` [hep-ph]].

[72] H. Ita, Z. Bern, L. J. Dixon, F. Febres-Cordero, D. A. Kosower and D. Maître, *Precise Predictions for Z + 4 Jets at Hadron Colliders*, Phys.Rev. **D85** (2012), 031501, [`arXiv:1108.2229` [hep-ph]].

[73] G. Cullen, N. Greiner, G. Heinrich, G. Luisoni, P. Mastrolia, G. Ossola and T. Reiter, *GoSam: A program for automated one-loop Calculations*, J.Phys.Conf.Ser. **368** (2011), 012056, [`arXiv:1111.6534` [hep-ph]].

[74] G. Cullen, N. Greiner, G. Heinrich, G. Luisoni, P. Mastrolia, G. Ossola, T. Reiter and F. Tramontano, *Automated One-Loop Calculations with GoSam*, Eur.Phys.J. **C72** (2012), 1889, [`arXiv:1111.2034` [hep-ph]].

[75] V. Hirschi, R. Frederix, S. Frixione, M. V. Garzelli, F. Maltoni and R. Pittau, *Automation of one-loop QCD corrections*, JHEP **05** (2011), 044, [`arXiv:1103.0621` [hep-ph]].

[76] F. Buccioni, J.-N. Lang, J. M. Lindert, P. Maierhöfer, S. Pozzorini, H. Zhang and M. F. Zoller, *OpenLoops 2*, Eur. Phys. J. C **79** (2019), no. 10, 866, [`arXiv:1907.13071` [hep-ph]].

[77] S. Actis, A. Denner, L. Hofer, J.-N. Lang, A. Scharf and S. Uccirati, *RECOLA: REcursive Computation of One-Loop Amplitudes*, Comput. Phys. Commun. **214** (2017), 140–173, [`arXiv:1605.01090` [hep-ph]].

[78] S. Actis, A. Denner, L. Hofer, A. Scharf and S. Uccirati, *Automatizing one-loop computation in the SM with RECOLA*, PoS **LL2014** (2014), 023.

[79] M. Schönherr, *An automated subtraction of NLO EW infrared divergences*, Eur. Phys. J. **C78** (2018), no. 2, 119, [`arXiv:1712.07975` [hep-ph]].

[80] S. Schumann and F. Krauss, *A parton shower algorithm based on Catani-Seymour dipole factorisation*, JHEP **03** (2008), 038, [`arXiv:0709.1027` [hep-ph]].

[81] S. Höche and S. Prestel, *The midpoint between dipole and parton showers*, Eur. Phys. J. **C75** (2015), no. 9, 461, [`arXiv:1506.05057` [hep-ph]].

[82] Z. Nagy and D. E. Soper, *A new parton shower algorithm: Shower evolution, matching at leading and next-to-leading order level*, `hep-ph/0601021`.

[83] Z. Nagy and D. E. Soper, *Matching parton showers to NLO computations*, JHEP **10** (2005), 024, [`hep-ph/0503053`].

[84] S. Höche et al., *Matching Parton Showers and Matrix Elements*, `hep-ph/0602031`.

[85] S. Frixione and B. R. Webber, *Matching NLO QCD computations and parton shower simulations*, JHEP **06** (2002), 029, [`hep-ph/0204244`].

[86] S. Catani, F. Krauss, R. Kuhn and B. R. Webber, *QCD matrix elements + parton showers*, JHEP **11** (2001), 063, [`hep-ph/0109231`].

[87] F. Krauss, *Matrix elements and parton showers in hadronic interactions*, JHEP **08** (2002), 015, [`hep-ph/0205283`].

[88] S. Höche, F. Krauss, S. Schumann and F. Siegert, *QCD matrix elements and truncated showers*, JHEP **05** (2009), 053, [`arXiv:0903.1219` [hep-ph]].

[89] S. Höche, F. Krauss, M. Schönherr and F. Siegert, *A critical appraisal of NLO+PS matching methods*, JHEP **09** (2012), 049, [`arXiv:1111.1220` [hep-ph]].

[90] T. Gehrmann, S. Höche, F. Krauss, M. Schönherr and F. Siegert, *NLO QCD matrix elements + parton showers in $e^+e^- \to$hadrons*, JHEP **01** (2013), 144, [`arXiv:1207.5031` [hep-ph]].

[91] S. Höche, F. Krauss, M. Schönherr and F. Siegert, *QCD matrix elements + parton showers: The NLO case*, JHEP **04** (2013), 027, [`arXiv:1207.5030` [hep-ph]].

[92] J.-C. Winter, F. Krauss and G. Soff, *A modified cluster-hadronisation model*, Eur. Phys. J. **C36** (2004), 381–395, [`hep-ph/0311085`].

[93] X. Artru and G. Mennessier, *String model and multiproduction*, Nucl. Phys. **B70** (1974), 93–115.

[94] B. Andersson, G. Gustafson, G. Ingelman and T. Sjöstrand, *Parton Fragmentation and String Dynamics*, Phys. Rept. **97** (1983), 31–145.

[95] B. Andersson, *The Lund model*, vol. 7, Camb. Monogr. Part. Phys. Nucl. Phys. Cosmol., 1997.

[96] M. Schönherr and F. Krauss, *Soft photon radiation in particle decays in SHERPA*, JHEP **12** (2008), 018, [`arXiv:0810.5071` [hep-ph]].

[97] M. Albrow, T. Coughlin and J. Forshaw, *Central Exclusive Particle Production at High Energy Hadron Colliders*, Prog.Part.Nucl.Phys. **65** (2010), 149–184, [`arXiv:1006.1289` [hep-ph]].

[98] S. Jadach and B. Ward, *Yfs2: The Second Order Monte Carlo for Fermion Pair Production at LEP / SLC With the Initial State Radiation of Two Hard and Multiple Soft Photons*, Comput. Phys. Commun. **56** (1990), 351–384.

[99] S. Jadach, B. F. L. Ward and Z. Wąs, *Coherent exclusive exponentiation for precision Monte Carlo calculations*, Phys. Rev. **D63** (2001), 113009, [`hep-ph/0006359`].

[100] F. A. Berends and R. Kleiss, *Distributions in the Process e+ e- —> mu+ mu- (gamma)*, Nucl. Phys. B **177** (1981), 237–262.

[101] F. A. Berends, G. Burgers and W. van Neerven, *On Second Order {QED} Corrections to the Z Resonance Shape*, Phys. Lett. B **185** (1987), 395.

[102] G. Burgers, *On the Two Loop {QED} Vertex Correction in the High-energy Limit*, Phys. Lett. B **164** (1985), 167–169.

[103] G. Passarino and M. Veltman, *One Loop Corrections for e+ e- Annihilation Into mu+ mu- in the Weinberg Model*, Nucl. Phys. B **160** (1979), 151–207.

[104] F. A. Berends, W. van Neerven and G. Burgers, *Higher Order Radiative Corrections at LEP Energies*, Nucl. Phys. B **297** (1988), 429, [Erratum: Nucl.Phys.B 304, 921 (1988)].

[105] F. A. Berends, R. Kleiss and S. Jadach, *Monte Carlo Simulation of Radiative Corrections to the Processes e+ e- —> mu+ mu- and e+ e- —> anti-q q in the Z0 Region*, Comput. Phys. Commun. **29** (1983), 185–200.

[106] O. Nicrosini and L. Trentadue, *Soft Photons and Second Order Radiative Corrections to $e^+e^- \to Z^0$*, Phys. Lett. **B196** (1987), 551.

[107] D. Y. Bardin, P. Christova, M. Jack, L. Kalinovskaya, A. Olchevski, S. Riemann and T. Riemann, *ZFITTER v.6.21: A Semianalytical program for fermion pair production in e^+e^- annihilation*, Comput. Phys. Commun. **133** (2001), 229–395, [`hep-ph/9908433`].

[108] P. Virtanen, R. Gommers, T. E. Oliphant, M. Haberland, T. Reddy, D. Cournapeau, E. Burovski, P. Peterson, W. Weckesser, J. Bright, S. J. van der Walt, M. Brett, J. Wilson, K. J. Millman, N. Mayorov, A. R. J. Nelson, E. Jones, R. Kern, E. Larson, C. J. Carey, İ. Polat, Y. Feng, E. W. Moore, J. VanderPlas, D. Laxalde, J. Perktold, R. Cimrman, I. Henriksen, E. A. Quintero, C. R. Harris, A. M. Archibald, A. H. Ribeiro, F. Pedregosa, P. van Mulbregt and SciPy 1.0 Contributors, *SciPy 1.0: Fundamental Algorithms for Scientific Computing in Python*, Nature Methods **17** (2020), 261–272.

[109] S. Jadach, W. Płaczek and M. Skrzypek, *QED exponentiation for quasi-stable charged particles: the $e^-e^+ \to W^-W^+$ process*, Eur. Phys. J. C **80** (2020), no. 6, 499, [`arXiv:1906.09071` [hep-ph]].

[110] M. W. Grunewald et al., *Reports of the Working Groups on Precision Calculations for LEP2 Physics: Proceedings. Four fermion production in electron positron collisions*, `hep-ph/0005309`.

[111] P. Abreu et al., DELPHI collaboration, *Cross-sections and leptonic forward backward asymmetries from the Z0 running of LEP*, Eur. Phys. J. C **16** (2000), 371–405.

[112] P. Abreu et al., DELPHI collaboration, *Measurement and interpretation of fermion pair production at LEP energies from 130-GeV to 172-GeV*, Eur. Phys. J. C **11** (1999), 383–407.

[113] J. Abdallah et al., DELPHI collaboration, *Measurement of the W pair production cross-section and W branching ratios in e+ e- collisions at s**(1/2) = 161-GeV to 209-GeV*, Eur. Phys. J. C **34** (2004), 127–144, [`hep-ex/0403042`].

[114] D. Y. Bardin et al., *Event generators for WW physics*, CERN Workshop on LEP2 Physics (followed by 2nd meeting, 15-16 Jun 1995 and 3rd meeting 2-3 Nov 1995), 9 1997, pp. 3–101.

[115] D. Abercrombie et al., *Dark Matter Benchmark Models for Early LHC Run-2 Searches: Report of the ATLAS/CMS Dark Matter Forum*, Phys. Dark Univ. **27** (2020), 100371, [`arXiv:1507.00966` [hep-ex]].

[116] P. Azzi et al., *Report from Working Group 1: Standard Model Physics at the HL-LHC and HE-LHC*, vol. 7, pp. 1–220, 12 2019.

[117] *High-Luminosity Large Hadron Collider (HL-LHC) : Preliminary Design Report.*

[118] A. Abada et al., FCC collaboration, *HE-LHC: The High-Energy Large Hadron Collider: Future Circular Collider Conceptual Design Report Volume 4*, Eur. Phys. J. ST **228** (2019), no. 5, 1109–1382.

[119] S. Kallweit, J. M. Lindert, P. Maierhöfer, S. Pozzorini and M. Schönherr, *NLO QCD+EW predictions for V + jets including off-shell vector-boson decays and multijet merging*, JHEP **04** (2016), 021, [`arXiv:1511.08692` [hep-ph]].

[120] A. Denner, S. Dittmaier, M. Roth and L. H. Wieders, *Electroweak corrections to charged-current e+ e- —> 4 fermion processes: Technical details and further results*, Nucl. Phys. **B724** (2005), 247–294, [`arXiv:hep-ph/0505042` [hep-ph]], [Erratum: Nucl. Phys.B854,504(2012)].

[121] V. Bertone, S. Carrazza, N. P. Hartland and J. Rojo, NNPDF collaboration, *Illuminating the photon content of the proton within a global PDF analysis*, SciPost Phys. **5** (2018), no. 1, 008, [arXiv:1712.07053 [hep-ph]].

[122] A. V. Manohar, P. Nason, G. P. Salam and G. Zanderighi, *The Photon Content of the Proton*, JHEP **12** (2017), 046, [arXiv:1708.01256 [hep-ph]].

[123] A. Manohar, P. Nason, G. P. Salam and G. Zanderighi, *How bright is the proton? A precise determination of the photon parton distribution function*, Phys. Rev. Lett. **117** (2016), no. 24, 242002, [arXiv:1607.04266 [hep-ph]].

[124] T. Gleisberg, S. Höche, F. Krauss, M. Schönherr, S. Schumann, F. Siegert and J. Winter, *Event generation with SHERPA 1.1*, JHEP **02** (2009), 007, [arXiv:0811.4622 [hep-ph]].

[125] F. Cascioli, P. Maierhöfer and S. Pozzorini, *Scattering Amplitudes with Open Loops*, Phys.Rev.Lett. **108** (2012), 111601, [arXiv:1111.5206 [hep-ph]].

[126] A. Denner, S. Dittmaier and L. Hofer, *COLLIER - A fortran-library for one-loop integrals*, PoS **LL2014** (2014), 071, [arXiv:1407.0087 [hep-ph]].

[127] G. Ossola, C. G. Papadopoulos and R. Pittau, *CutTools: A Program implementing the OPP reduction method to compute one-loop amplitudes*, JHEP **0803** (2008), 042, [arXiv:0711.3596 [hep-ph]].

[128] A. Gehrmann-De Ridder, T. Gehrmann and E. W. N. Glover, *Antenna subtraction at NNLO*, JHEP **09** (2005), 056, [hep-ph/0505111].

[129] A. Gehrmann-De Ridder, T. Gehrmann and E. Glover, *Gluon–gluon antenna functions from Higgs boson decay*, Physics Letters B **612** (2005), no. 1-2, 49–60.

[130] A. Gehrmann-De Ridder, T. Gehrmann and E. Glover, *Quark-gluon antenna functions from neutralino decay*, Phys. Lett. B **612** (2005), 36–48, [hep-ph/0501291].

[131] A. Daleo, T. Gehrmann and D. Maître, *Antenna subtraction with hadronic initial states*, JHEP **04** (2007), 016, [`hep-ph/0612257`].

[132] A. Daleo, A. Gehrmann-De Ridder, T. Gehrmann and G. Luisoni, *Antenna subtraction at NNLO with hadronic initial states: initial-final configurations*, JHEP **01** (2010), 118, [`arXiv:0912.0374` [hep-ph]].

[133] T. Gehrmann and P. F. Monni, *Antenna subtraction at NNLO with hadronic initial states: real-virtual initial-initial configurations*, JHEP **12** (2011), 049, [`arXiv:1107.4037` [hep-ph]].

[134] R. Boughezal, K. Melnikov and F. Petriello, *A subtraction scheme for NNLO computations*, Phys.Rev. **D85** (2012), 034025, [`arXiv:1111.7041` [hep-ph]].

[135] M. Ritzmann, D. Kosower and P. Skands, *Antenna Showers with Hadronic Initial States*, Phys.Lett. **B718** (2013), 1345–1350, [`arXiv:1210.6345` [hep-ph]].

[136] J. Currie, A. Gehrmann-De Ridder, E. Glover and J. Pires, *NNLO QCD corrections to jet production at hadron colliders from gluon scattering*, JHEP **1401** (2014), 110, [`arXiv:1310.3993` [hep-ph]].

[137] X. Chen, T. Gehrmann, N. Glover, M. Höfer and A. Huss, *Isolated photon and photon+jet production at NNLO QCD accuracy*, Journal of High Energy Physics **2020** (2020), no. 4, .

[138] S. Jadach and B. Ward, *Exponentiation of Soft Photons in the Monte Carlo: The Case of Bonneau and Martin*, Phys. Rev. D **38** (1988), 2897, [Erratum: Phys.Rev.D 39, 1471 (1989)].